# Spin–Exchange Polarized $^3$He Using Optically Pumped Alkali Atoms for Magnetic Resonance Imaging and Neutron Spin–Filters.

BY

Vance Reid Pomeroy

B.S., University of New Hampshire (1990)
M.S., University of New Hampshire (1992)

DISSERTATION

Submitted to the University of New Hampshire
in partial fulfillment of
the requirements for the degree of

Doctor of Philosophy

in

Physics

May 1998

This dissertation has been examined and approved.

Director, F. William Hersman
Professor of Physics

John R. Calarco
Professor of Physics

John F. Dawson
Professor of Physics

James M. Ryan
Professor of Physics

John J. Wright
Professor of Physics

Date

# Dedication

To Judith with love.

# Table of Contents

# List of Tables

# List of Figures

# ABSTRACT

## Spin–Exchange Polarized $^3$He Using Optically Pumped Alkali Atoms for Magnetic Resonance Imaging and Neutron Spin–Filters.

by

Vance Reid Pomeroy

University of New Hampshire, May, 1998

The past several years have witnessed an increase in applications of polarized noble gases. In particular, the development of high power lasers has enabled the realization of dense, highly polarized samples of $^3$He. We report here the development of a system to produce high density, highly polarized samples of $^3$He gas. We developed a liquid helium system to cryogenically increase the density of $^3$He gas to pressures exceeding 10 atmospheres. We developed a system based on adiabatic fast passage nuclear magnetic resonance to measure and monitor the $^3$He nuclear polarization. Polarizations as high as 64 % were measured and cells with polarization decay lifetimes as long as 180 hours were produced.

We present the first known two dimensional images acquired with polarized noble gases at 21 gauss. Under typical magnetic resonance imaging conditions the polarization of protons is $\sim 5.2\times 10^{-4}$ %. Using spin exchange optical pumping, we are able to produce $^3$He polarizations of tens of percent with no field dependence. We acquired images at 21 gauss with a custom imager and at 47,000 gauss using a commercial imager with equivalent resolution and signal strength. We acquired images of a rat lung at 21 gauss with a measured $T_1 \approx 40$ s and $T_2^* > 100$ ms. To demonstrate the applicability of low field imaging in and around conductive materials, we acquired images of a polarized $^3$He sample inside a 25.4 $\mu$m brass box at 21 gauss. Additionally, compared to the large distortions observed at high fields, we imaged a $^3$He sample near known paramagnetic materials with minimal distortions.

We fabricated polarized $^3$He based neutron spin–filters and used them in two experiments at the Los Alamos Neutron Science Center. Spin–filters were produced at three and six atmospheres with flat entrance and exit windows for a constant thickness of $^3$He. The first experiment utilized one of these spin–filters to measure the neutron polarization for neutron energies ranging from 25 meV to 10 eV. The second experiment required a spin–filter to polarize neutrons and another one to analyze the spin of the neutrons having passed through a $^{139}$La target.

*"... it is my necessary breath of life to understand...."*

— *Ruth Benedict*

# Chapter 1

# Introduction

First produced by Kastler[5] in 1950, polarized $^3$He has been a useful tool and testing ground in many areas of research. Numerous experiments have utilized polarized $^3$He targets to study fundamental interactions in nuclear and high energy physics. In addition, a technique in magnetic resonance imaging using polarized noble gases to image human lungs and airways has been realized.

This thesis reports on the development of a system to polarize $^3$He nuclei using spin exchange with optically pumped rubidium atoms. In addition, a description of neutron spin–filters and the first polarized $^3$He low–field 2–D images are given.

## Methods of Polarizing $^3$He

There are two methods for polarizing $^3$He in its gaseous form: metastability exchange optical pumping and spin–exchange with optically pumped alkali atoms. The metastability exchange method uses direct optical pumping of the metastable $2^3S_1$ state of $^3$He. The metastable atoms are produced by an RF discharge at pressures of roughly one torr of $^3$He gas. The electron spin metastable state is polarized by optically pumping the $2^3S_1 \rightarrow 2^3P_0$ transition with 1083 nm circularly polarized light. Recent developments[1] in arc–lamp–pumped neodymium–doped lanthanum magnesium hexaluminate (Nd:LMA) lasers at 1083 nm have yielded high $^3$He polarization. Polarization is then transferred to the nucleus through the hyperfine interaction. Recently,[2] metastable optical pumping experiments with mixtures of $^3$He and $^4$He were performed using a 50 mW diode laser, producing $^3$He polarizations of 80% when the laser was tuned to the $^4$He line and 50% when pumping in the absence of $^4$He. Since the density is low under optical pumping conditions, polarized $^3$He internal targets have been realized based on the metastable exchange method.[3] Dense samples of polarized $^3$He have been produced utilizing a mechanical compression system.[4]

The second method for polarizing $^3$He is through spin exchange with optically pumped rubidium vapor. Rubidium valence electrons are polarized by absorption of circularly polarized resonant laser light at 795 nm. Through collisions with $^3$He atoms, polarization is transferred to the $^3$He nucleus by the hyperfine interaction. In a well designed system, the time constant for spin exchange is on the order of 10 hours. The spin exchange method has produced high polarizations ($> 50\%$) at pressure exceeding 10 atmospheres. Advances in high power Ti:Sapphire lasers and, more recently, laser diode arrays, have dramatically improved the performance of this method. Chapter 2 describes the optical pumping technique and Chapter 3 provides the details used to produce samples of highly polarized $^3$He.

## Nuclear and Particle Physics

The $^3$He nucleus is of considerable interest in nuclear and particle physics. The ground state wave function is exactly solvable for modern two–body potentials. The dominant component of the ground state wave function is the spatially symmetric S–state, with the protons paired to spin = 0 and the neutron is left to carry the spin. The wave function also has a D–state, due to the tensor force where the three nucleons are oriented antiparallel to the $^3$He nuclear spin and an S′–state where the protons are parallel to one another and opposite to the neutron spin. Non–relativistic Faddeev calculations[6–8] of the three body bound state predict contributions to the ground state from a ∼90 % S–state, ∼8 % D–State, and a $\lesssim$2 % S′–state. This picture is supported by the similarity between neutron and $^3$He magnetic moments ($\mu_n$=–1.91$\mu_N$ and $\mu_{He}$=–2.12$\mu_N$). Fundamental properties of the neutron, such as its charge distribution and spin structure, are unconstrained experimentally. Currently, several experiments are utilizing polarized $^3$He to measure the neutron electromagnetic form factors[9–11] and structure functions at SLAC[12–14] and at HERMES.[15]

In addition to polarized target experiments, polarized $^3$He samples can be used to produce broad band beams of polarized low energy neutrons. Polarized $^3$He has a large spin–dependent cross section for the reaction

$$n +^3 He \rightarrow^4 He^* \rightarrow t + p$$

which enables it to function as a neutron spin–filter. Neutrons with spin parallel to the $^3$He spin have a low capture cross section as compared to neutrons with spin antiparallel. By using highly polarized samples of $^3$He, neutron beams with nearly 100 % polarization and up to 50 % transmission of the desired polarization can be produced. These polarized neutron beams can be used in a wide variety of nuclear and particle physics experiments. Fundamental physics experiments exploring symmetry violation, such as parity and time nonconservation, are essential tests of current theories to improve our understanding of the natural world. Polarized neutron beams can be utilized to explore violation of time reversal symmetry through free neutron beta decay[16] and the triple correlation between the neutron spin and momentum and the spin of a polarized target.[17] Chapter 5 discusses the details of neutron spin–filters for two experiments at the Los Alamos Neutron Science Center. The first of these experiment measured the neutron polarization from the transmission through a spin–filter. The second experiment measured the parity–violating neutron spin rotation through $^{139}$La. This experiment required the use of a $^3$He spin–filter and spin–analyzer.

## Magnetic Resonance Imaging

Since the first image of polarized $^{129}$Xe in mouse lungs,[18] polarized $^3$He and $^{129}$Xe have been used to image both animal and human organs. $^3$He and $^{129}$Xe gases can be polarized to values much larger than the thermal Boltzmann polarization ($10^{-5}$–$10^{-6}$). Due to the high polarization, magnetic resonance imaging with noble gases can be realized. The lower density of noble gases is compensated by the high nonequilibrium polarization, resulting in ample signal strength to perform the hundreds of NMR pulses required for imaging. Compared to proton imaging, polarized noble gas imaging utilizes small flip angles so as not to deplete the polarization between acquisitions. Pulse sequences have been developed to accommodate the special requirements for polarized noble gas imaging.[19] The resolution of images acquired with polarized noble gases have surpassed those previously acquired by other methods. Due to its recent success, polarized gas MRI is being tested as a diagnostic and surgical planning tool for Chronic Obstructive Pulmonary Disease.

Unlike conventional proton imaging where the polarization is magnetic field dependent, $^3$He polarization is independent of the field strength; this allows for the use of lower fields. In Chapter 4, details of the first low–field (21 gauss) imaging experiments are given. This is an exciting advancement to the field of magnetic resonance imaging. Some of the benefits of using lower fields are discussed, including imaging in the presence of conducting and magnetic materials.

*"The good spinner hath a large shift."*

— *Benjamin Franklin*

# Chapter 2

# Optical Pumping

## 2.1 Introduction

Polarization of a noble gas via spin exchange requires a source of angular momentum to transfer to the noble gas nucleus; in this case, the source is optically pumped rubidium. Optical pumping of rubidium is accomplished by absorption of resonant photons that carry angular momentum to the atom. The spin transfer depends on the helicity of the photon and the initial state of the atom. Absorption of circularly polarized photons causes the magnetic quantum number, m, of the quantum system to change by $\Delta\mathrm{m} = \pm1$. If the atom emits a photon from the excited state, some of the angular momentum is carried away. If the angular momentum of the emitted photon is different from that of the absorbed photon, the atom is left with the difference. While optical pumping is used to change the electron spin, nuclear spin can be modified by the hyperfine interaction between the electron and nuclear magnetism. Section 2.3 will address the issue of optical pumping of atoms with non–zero nuclear spin.

The field of optical pumping in the presence of noble gases has been advanced in recent years by the development of high intensity light sources. In particular, for the D1 spectral line of rubidium, high power Ti:Sapphire and diode lasers at 794.7 nm have been used to achieve large rubidium polarization.

In this chapter, the basics of optical pumping will be discussed. Optical pumping was first introduced by Kastler[20] in 1950 as a way of producing a nonequilibrium population of spin states amongst the sublevels of the atom in its ground state. For a more thorough description of this field, the reader is referred to several reviews[21–27] and to Wagshul[28] *et al.* and Larson[29] *et al.* for the specific case of Rb optical pumping in the presence of $^3$He.

## 2.2 Optical Pumping with Zero Nuclear Spin

### 2.2.1 Fundamentals

In this section, an introduction to optical pumping is given, with an emphasis on the D1 transition of Rb with zero nuclear spin. To begin, Rb vapor is illuminated with circularly polarized laser light on or near resonance with helicity $\sigma_\pm$ along the quantization axis. Angular momentum of an incident photon is transferred to a Rb atom. Transitions occur that satisfy the selection rule $\Delta m = \pm1$. The optical pumping diagram for the D1 transition of Rb for resonant light with helicity $\sigma_+$ is shown in figure 2-1. This figure shows that there are only two magnetic sublevels ($m_s = \pm1/2$) in both the ground state $5^2S_{1/2}$ and the excited state, $5^2P_{1/2}$. For an incident beam of laser light with helicity $\sigma_+$, only the magnetic sublevel $m_s = -1/2$ can undergo a transition to an excited state. Once in the excited state the atom returns to the ground state via spontaneous emission, ending up in one of the two sublevels. Eventually the $+1/2$ level of the ground state will have an increased population relative to that of the -1/2 level, thus creating a polarization of the electron spin. The removal of electrons from the -1/2 state is referred to as depopulation pumping. The Clebsch-Gordon coefficients are given in figure 2-1a) for the transition to the ground state. On average, three photons are needed to move the atom from the -1/2 level to the +1/2 level.

The efficiency of populating the sublevel $m_s = 1/2$ can be increased by adding a buffer gas. $^3$He buffer gas will collisionally mix the sublevels and thus randomize the angular momentum in the excited state. This randomization will have the effect of averaging the transition probabilities. In order for the reorientation of the excited state to increase the pumping rate, the mixing of the ground state must occur less frequently. For alkali atoms in helium buffer gas, the depolarization cross section is roughly $10^{-25}$ cm$^2$ for the ground state (S-state), and approximately $10^{-15}$ cm$^2$ for the excited state (P-state).[26] Additionally, to equalize transitions to the ground state sublevels, the time to mix the excited state sublevels must be short compared to the time it takes the atom to spontaneously decay to the ground state.

For a transition to the ground state via spontaneous emission, the photon can be reabsorbed by another rubidium atom and, thus, reducing the sample polarization; this effect is called radiation trapping. Radiation trapping increases with the density of alkali vapor. Because of its large quenching cross section, $N_2$ buffer gas is added to the cell to reduce spontaneous emission of photons. Helium has a low quenching cross section which necessitates the use of $N_2$. The Rb atom transfers energy to the $N_2$ molecule producing rotational and vibrational degrees of freedom of the molecule. Spin angular momentum is not conserved during quenching, so transitions to either spin state have equal probability. So that the quenching rate for $N_2$ exceeds the radiative decay rate,[23] nitrogen pressures of 30 to 100 torr are added.

The diagram for optical pumping the D1 line of Rb in the presence of helium and $N_2$ buffer gases is shown in figure 2-1 b). Once in an excited state, the atom undergoes collisional mixing which populates both magnetic substates; it then returns to one of the sublevels in the ground state via a nonradiative transition. If the atom ends up in the magnetic sublevel $m_s = 1/2$, it will remain there until some spin destruction interaction occurs. If the atom returns to the sublevel $m_s = -1/2$, it will undergo more transitions to the excited state until an equilibrium point is reached, balancing the number of incident photons to the relaxation of rubidium in the ground state. The Clebsch-Gordon coefficients for buffer gas mixing and quenching with $N_2$ are shown in the figure. It takes on average two photons to pump the atom from the -1/2 sublevel to the +1/2 sublevel in the presence of $N_2$ and $^3$He buffer gases.

### 2.2.2 Optical Pumping Rate Equations

To consider the case of rubidium optical pumping in the presence of $^3$He and $N_2$ buffer gases, the absorption of linearly polarized laser light by Rb vapor is examined. Linearly polarized laser light is absorbed by either sublevel in the ground state (S-state). The absorption cross section for a linearly polarized photon is[29]

$$\sigma(\nu) = \frac{\Lambda_0^2}{8\pi}\Gamma_{nat}\left[\frac{\Gamma}{(\nu-\nu_0)^2+(\Gamma/2)^2} + \frac{b(\nu-\nu_0)}{\Gamma}e^{\frac{-|\nu-\nu_0|}{\Gamma_a}}\right]. \tag{2.1}$$

The first term in the cross section is a Lorentzian lineshape, which is symmetric about the frequency $\nu_0$ (wavelength $\Lambda_0$ = 794.7 nm). $\Gamma$ is the pressure broadened linewidth (18.7±0.3) GHz/atm for $^3$He, and (17.8±0.3) GHz/atm for $N_2$,[30] and $\Gamma_{nat}$ is the natural linewidth (5.66 MHz). The pressure broadened width is much wider than the natural and Doppler-broadened width (250 MHz). Pressure broadening can be viewed as a consequence of the distortion of the atomic levels due to the Rb–$^3$He

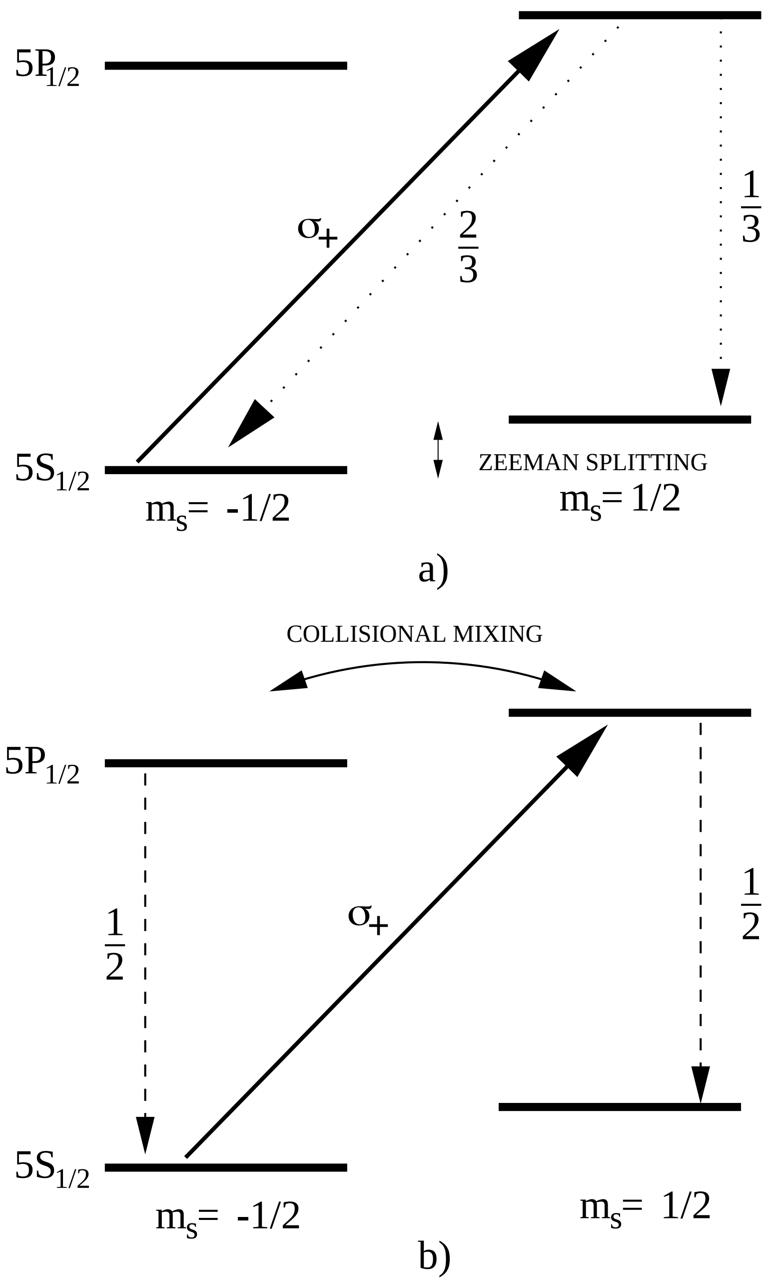

Figure 2-1: Optical pumping diagrams for the D1 transition of Rb ignoring nuclear spin. The solid lines represent absorption of circularly polarized laser light $\sigma_+$, while the dotted and dashed lines indicate allowed transitions with their corresponding probabilities. Figure a) shows the diagram for optical pumping of Rb without any buffer gases. The dotted lines correspond to radiative transitions. Figure b) diagrams optical pumping of Rb in the presence of helium and $N_2$ buffer gases. The dashed lines correspond to nonradiative transitions.

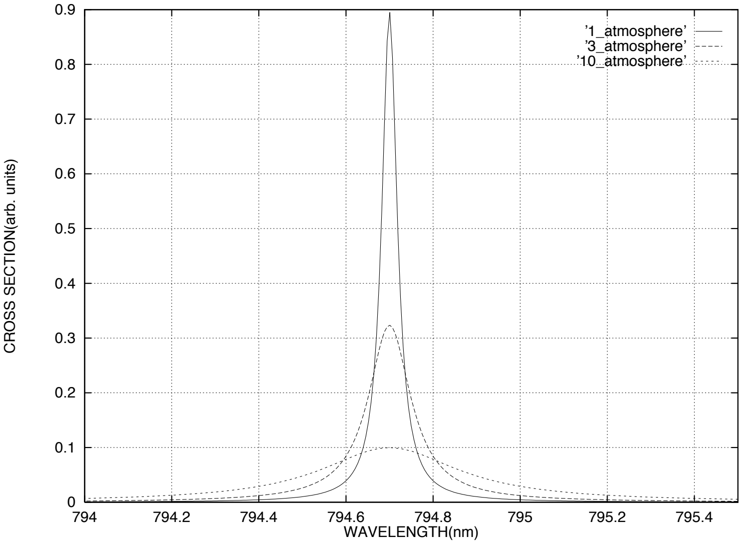

Figure 2-2: Relative absorption cross sections for samples containing 1, 3, and 10 atmospheres of $^3$He.

interatomic potential.[31–33] The second term in equation (2.1) is a parameterization of the observed line–shape asymmetry and line–shift which has a negligible effect on the polarization. Researchers at Princeton[30] have recently completed $D_1$ and $D_2$ line–width, line–shift and asymmetry measurements of the absorption cross section. Measurement of the frequency shift and asymmetry can be used to determine noble gas density in a cell. This can be a useful technique when the exact determination of the number density is required[1]. Integration of equation (2.1) gives

$$\int_{-\infty}^{\infty} \sigma(\nu) d\nu = \frac{\Lambda_0^2}{4} \Gamma_{nat} = \pi r_e c f,$$

where $r_e$ is the classical electron radius, $c$ is the speed of light, and $f$ is the D1 transition oscillator strength.

For circularly polarized light $\sigma_{\pm}$, absorption only occurs for atoms in the $\mp 1/2$ sublevel. For left circularly polarized light $\sigma_+$ the rate equations for the populations in the ground state sublevels are

$$\frac{d\rho_{\pm 1/2}}{dt} = \pm \left[ \frac{\Gamma_{SD}}{2} + \gamma_{opt} \right] \rho_{-1/2} \mp \frac{\Gamma_{SD}}{2} \rho_{1/2}, \tag{2.2}$$

where $\rho_{1/2}$ and $\rho_{-1/2}$ are the normalized population densities that satisfy the equation $\rho_{1/2} + \rho_{-1/2} = 1$. $\Gamma_{SD}$ is the spin destruction rate in Hz, $\gamma_{opt}$ is the photon absorption rate per Rb atom for circularly polarized photons and is given by

$$\gamma_{opt}(\vec{r}) = \int \Phi^+(\nu, \vec{r}) \sigma(\nu) d\nu. \tag{2.3}$$

---

[1] The number density can also be determined using the transmission of a low energy neutron beam through the cell (see chapter 5).

$\Phi^{+}(\nu, \vec{r})$ is the flux of circularly polarized photons at a frequency $\nu$ ($\mathrm{GHz}^{-1}\mathrm{cm}^{-2}\mathrm{s}^{-1}$) and is related to the intensity $I(\vec{r})$ and total laser power $P(\vec{r})$ at the point $\vec{r}$ by

$$I(\vec{r}) = \int \Phi^{+}(\vec{r}, \nu) d\nu$$

$$P(\vec{r}) = \int d^2 r \int h\nu \Phi(\vec{r}, \nu) d\nu,$$

and $\sigma(\nu)$ is the unpolarized cross–section (equation (2.1)).

For an initially unpolarized Rb vapor, the solution to equation (2.2) is

$$\begin{aligned} P_{Rb}(t) &= \rho_{1/2} - \rho_{-1/2} && (2.4) \\ &= \frac{\gamma_{opt}(\vec{r})}{\gamma_{opt}(\vec{r}) + \Gamma_{SD}} \left(1 - e^{-(\gamma_{opt}(\vec{r}) + \Gamma_{SD})t}\right). && (2.5) \end{aligned}$$

The position dependent steady–state Rb polarization from equation (2.5) is

$$P_{Rb}(\vec{r}, t = \infty) = \frac{\gamma_{opt}(\vec{r})}{\gamma_{opt}(\vec{r}) + \Gamma_{SD}}. \qquad (2.6)$$

For Rb polarizations approaching 100% $\gamma_{opt} \gg \Gamma_{SD}$.

The propagation of circularly polarized laser light through Rb vapor is given by

$$\frac{d\Phi(\vec{r}, \nu)}{dz} = -\lambda^{-1}(\vec{r}, \nu)\Phi(\vec{r}, \nu), \qquad (2.7)$$

where $\lambda(\vec{r}, \nu)$ is the photon absorption length:[28]

$$\lambda^{-1}(\vec{r}, \nu) = 3[Rb]\sigma\nu(|\langle\frac{1}{2}, -\frac{1}{2}, 1, m_p|\frac{1}{2}, m\rangle|^2\rho_{-1/2} + |\langle\frac{1}{2}, \frac{1}{2}, 1, m_p|\frac{1}{2}, m\rangle|^2\rho_{1/2}), \qquad (2.8)$$

where $m_p = 0, \pm 1$ is the z component of the photon angular momentum, and $m$ is the sublevel in the excited state. $[Rb]$ is the Rb number density with units $\mathrm{cm}^{-3}$ and $\sigma(\nu)$ is the absorption cross section for linearly polarized light. For a left circularly polarized incident laser light $\sigma_{+}$, incident upon Rb vapor in the presence of a buffer gas, equation (2.7) becomes

$$\begin{aligned} \frac{d\Phi(\vec{r}, \nu)}{dz} &= -2\Phi(\vec{r}, \nu)[Rb]\sigma(\nu)\rho_{-1/2} && (2.9) \\ &= -\Phi(\vec{r}, \nu)[Rb]\sigma(\nu)[1 - P_{Rb}(\vec{r})], && (2.10) \end{aligned}$$

where $P_{Rb}$ is the spatially dependent Rb polarization. Taking the simple case of a uniformly illuminated cell with an incident resonant laser light traveling along the z-axis, and ignoring Rb polarization losses due to radiation trapping and diffusion to the walls, equation (2.7) becomes

$$\frac{d\Phi(z, \nu)}{dz} = -\Phi(z, \nu)[Rb]\sigma(\nu)[1 - P_{Rb}(z)]. \qquad (2.11)$$

The Rb polarization as a function of z in the cell using equations (2.3), (2.6), and (2.11) can be determined. Figure 2-3 shows the calculated flux profile for this simplified case.

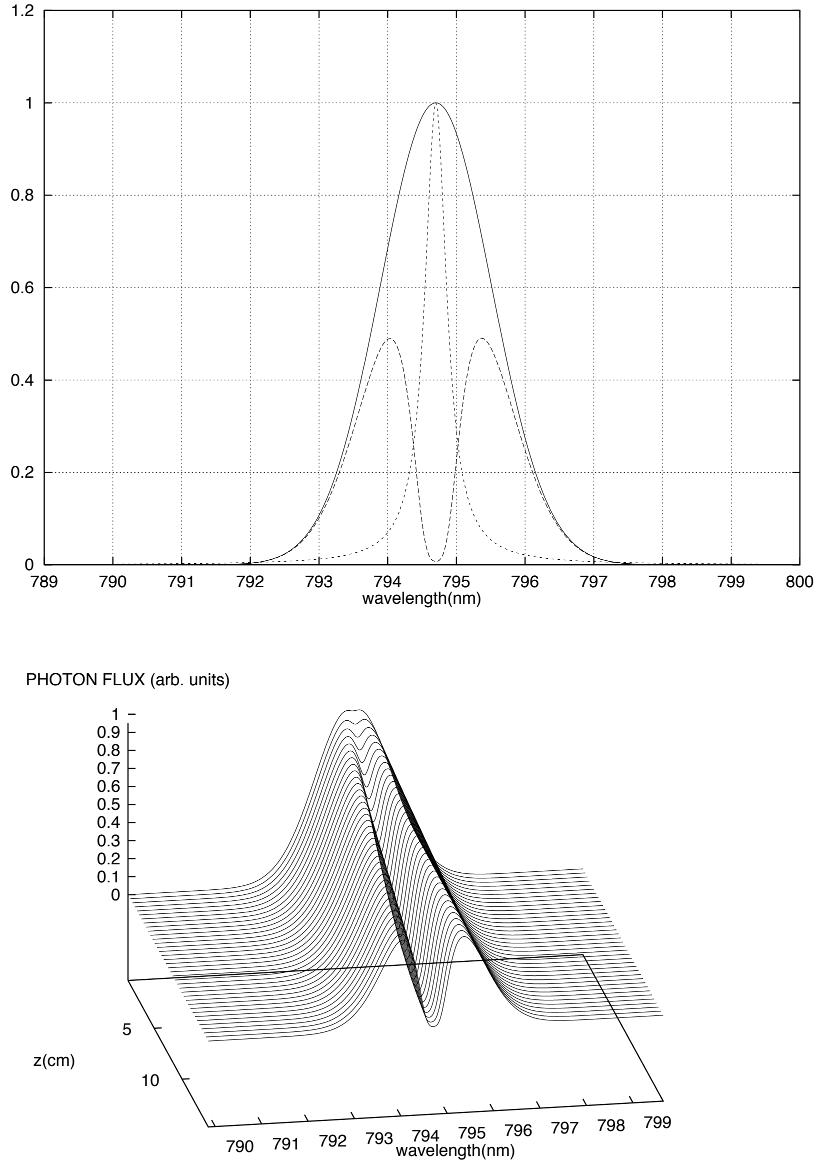

Figure 2-3: Calculated flux distribution for a 15 W circularly polarized photon beam centered at 794.7 nm with a Gaussian distribution width of 1.9 nm passing through a 15 cm long, 2.9 cm diameter cylindrical cell containing 10 atmospheres of $^3$He (at 0 °C), 100 torr of $N_2$ a and rubidium number density of $4.0 \times 10^{14}$ cm$^{-3}$. Depolarization due to radiation trapping is assumed not to exist as a consequence of quenching by $N_2$ gas. Additionally, there is no depolarization from diffusion near the walls. The top figure contains the initial and final photon flux after passing through 15 cm of Rb vapor. Also included in the top figure is the normalized line shape of the D1 absorption cross section. The bottom figure is the laser flux profile as a function of wavelength and depth in the cell.

## 2.3 Nonzero Nuclear Spin Effects

The total spin of an atom is given by

$$\mathbf{F} = \mathbf{L} + \mathbf{S} + \mathbf{I} = \mathbf{J} + \mathbf{I}$$

where **L** is the orbital angular momentum of the electron, **S** is the spin angular momentum of the electron, and **I** is the nuclear spin. Rb has two stable isotopes, $^{85}$Rb and $^{87}$Rb. The spin and abundances for the two isotopes are I = 5/2, I = 3/2, and 72.17%, 27.83% respectively. Both the ground state and the excited state of the D1 transition have two hyperfine multiplets, F = 1 and F = 2 for $^{87}$Rb and F=2 and F=3 for $^{85}$Rb. As illustrated in figure 2-4, there are eight ground state sublevels of $^{87}$Rb (I = 3/2). Similarly, there would be twelve levels for the ground state of $^{85}$Rb (I = 5/2). These are compared to the simple two level diagram (figure 2-1) that has been examined up to this point. As with the two level system, for a given helicity of incident light, there is a level in the ground state that is populated by decays from the excited state and does not get depopulated by the incident photons. For the ground state F = 3 and $m_F$ = 3 of $^{85}$Rb, and the $^{87}$Rb ground state F = 2 and $m_F$ = 2, no transitions to an excited state exist. However, it now takes many more excitations to move the electrons to this state. Fortunately, most interactions do not affect the nuclear spin, allowing the nucleus to act as a reservoir of angular momentum. If an electron in the $^{87}$Rb atom is in the state F = 2 $m_F$ = 2 it will likely end up in one of the $m_F$ = 1 levels after a spin exchange interaction. On average, it will then take only two excitations to move it back into the F=2 $m_F$=2 state. Therefore, the nucleus slows down the pumping process, but it also reduces the relaxation rate. Wagshul *et al.*[28] investigated more closely effects due to nuclear spin.

## 2.4 Relaxation

The asymptotic value of the rubidium polarization is given by $P_{Rb}=\gamma_{opt}/(\gamma_{opt}+\Gamma_{SD})$, where $\Gamma_{SD}$ is the sum of all relaxation mechanisms. As $\Gamma_{SD}$ increases, more incident photons per second are required to maintain a constant rubidium polarization. An approximate value for the minimum laser power needed is given by

$$P_{min} = \Gamma_{SD}[Rb]V_{cell}P_{Rb}$$

where $[Rb]$ is the rubidium number density, $V_{cell}$ is the cell volume and $P_{Rb}$ is the rubidium polarization. Since interactions with the walls of the cell causing rubidium depolarization is not included in $\Gamma_{SD}$, this value underestimates the actual power needed to polarize a sample. Rb atoms near the cell walls are unpolarized approximately 100% of the time and thus absorb more light than atoms far away from the walls. $\Gamma_{SD}$ is given by

$$\Gamma_{SD} = k_{Rb--Rb}[Rb] + k_{Rb--N_2}[Rb] + k_{Rb--He}[He] \tag{2.12}$$

where $k_{Rb--Rb}$ and $k_{Rb--N_2}$ are the rate coefficients corresponding to spin destruction due to rubidium and nitrogen. $k_{Rb--He}$ is the rate coefficient for polarization loss due to interactions with helium, $k_{Rb--He} = k_{SD} + k_{SE}$; where $k_{SD}$ and $k_{SE}$ are the $^3$He–Rb spin destruction and spin exchange rates. $k_{SD}$ is due to the coupling of the rubidium spin **S** to the rotational angular momentum **N** of the colliding atoms.[34] $k_{SE}$ is due to the rubidium atom valence electron penetrating the core and transferring its spin to the $^3$He nucleus. Recent measurements of the Rb and $^3$He rate coefficients

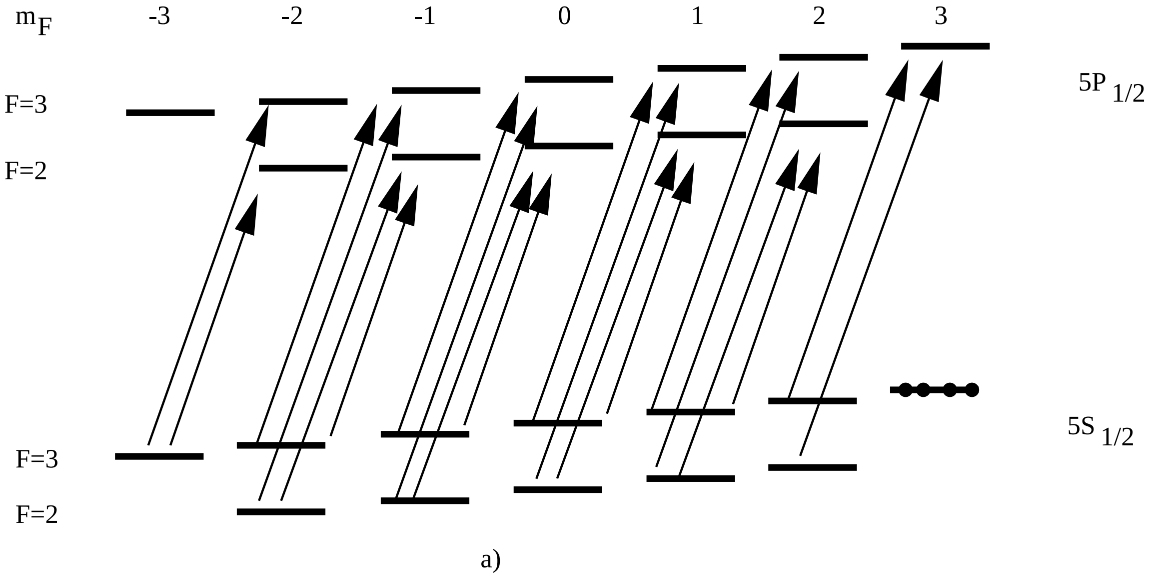

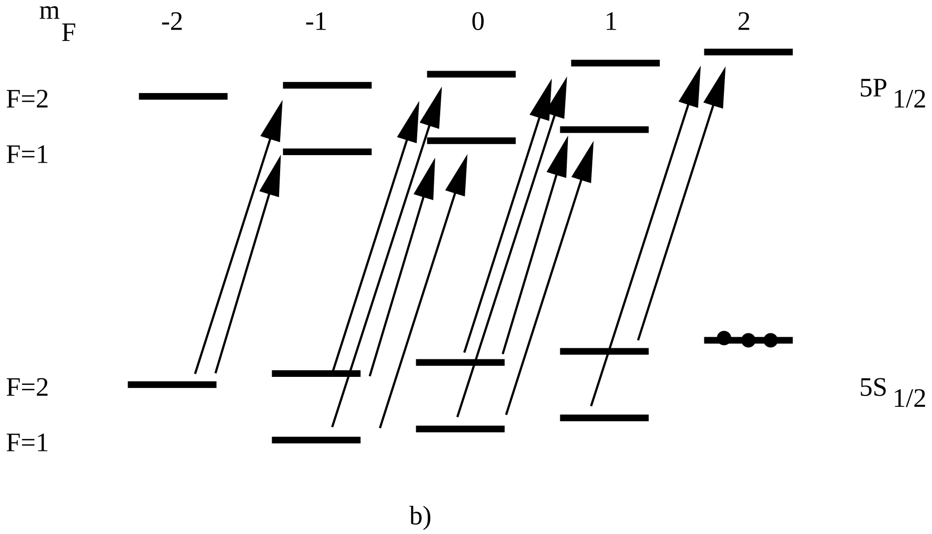

Figure 2-4: Level schemes for a) $^{85}$Rb and b) $^{87}$Rb D1 transition with $\sigma_+$ light.

have been performed[42] with the results:

$$\begin{aligned} k_{Rb--Rb} &= (4.2 \pm 0.4) \times 10^{-13} \mathrm{cm}^3 \mathrm{s}^{-1} \\ k_{Rb--He} &= 1.0 \times 10^{-29} T^{4.259} \mathrm{cm}^3 \mathrm{s}^{-1} \\ k_{SE} &= (6.7 \pm 0.6) \times 10^{-20} \mathrm{cm}^3 \mathrm{s}^{-1}. \end{aligned}$$

Previous measurements of $k_{Rb--Rb}$ were performed by Knize[35] with the quoted value $k_{Rb--Rb} = (7.8 \pm 0.8) \times 10^{-13} \mathrm{cm}^3 \mathrm{s}^{-1}$, and by Wagshul and Chupp[28] with the quoted value $k_{Rb--Rb} = (8.11 \pm 0.33) \times 10^{-13} \mathrm{cm}^3 \mathrm{s}^{-1}$ The difference between these earlier values and the recent measurements by Baranga *et al.*[42] may be due to the temperature dependence found in $k_{Rb--He}$. The spin destruction rate coefficient for interaction with nitrogen, $k_{Rb--N_2}$, was measured by Wagshul and Chupp

$$k_{Rb--N_2} = (9.38 \pm 0.22) \times 10^{-18} \mathrm{cm}^3 \mathrm{s}^{-1}.$$

For a sample containing 1 atmosphere of $^3$He and 100 torr of $N_2$ gas the Rb spin destruction rate is

$$\Gamma_{SD} = 166_{Rb--Rb} + 33.2_{Rb--N_2} + 55.2_{Rb--He} = 256 \mathrm{s}^{-1}$$

where [Rb] = $4 \times 10^{14}$ and T=453 K. Increasing the $^3$He pressure to 10 atmospheres gives

$$\Gamma_{SD} = 166_{Rb--Rb} + 33.2_{Rb--N_2} + 550.2_{Rb--He} = 749.4 \mathrm{s}^{-1}.$$

At these higher pressures the Rb spin destruction is dominated by the Rb–$^3$He interaction. At 10 atmospheres, only 2.4% of the Rb spin destruction is due to spin exchange with $^3$He.

*"She can spin.–Then may I set the world on wheels, when she can spin for a living."*

*— William Shakespeare*

# Chapter 3

# Polarized $^3$He

Polarization of the $^3$He nucleus by spin exchange with optically pumped Rb was first reported by Bouchiat *et al.*[36] in 1960. Rb atoms were optically pumped using resonant light from a Rb lamp passing through a linear polarizer and quarter–wave plate into a Pyrex bulb containing 2.8 atmospheres of $^3$He gas at 140 °C. A Rb polarization of 10% was observed and a $^3$He nuclear polarization of .01% was measured, which is roughly $10^4$ times greater than its value at room temperature in a 123 Gauss field due to a Boltzmann distribution of states. The limiting factors for achieving high $^3$He polarization were low Rb polarization due to an insufficient flux of resonant light and a short lifetime of the $^3$He polarization. Herman[37] later showed that the spin exchange process is dominated by the Fermi contact interaction between the $^3$He nucleus and the Rb valence electron and is about 3 orders of magnitude greater than the magnetic interaction between the dipoles of each atom. Gamblin and Carver[38] went on to show that relaxation mechanisms limited the final achievable $^3$He polarization; relaxation due to field gradients were examined experimentally and theoretically.

## 3.1 Spin Exchange

The process of spin exchange occurs during binary collisions between the optically pumped alkali atom and the noble gas nucleus (see figure 3-1). During collisions, there is a small probability that the alkali atom's valence electron will penetrate through the noble gas electron cloud and into its nucleus. It is the hyperfine interaction between the alkali valence electron and the noble gas nucleus that mediates spin exchange. Most of the time the electronic spin is transferred into rotational angular momentum of the colliding atoms. There are two interactions relevant in the spin–exchange process: the dipole–dipole interaction and the formation of van der Waals molecules. For the Rb–$^3$He system, the collisions are short and so only the dipole–dipole interaction is relevant. However, the formation of van der Waals molecules with heavier noble gas atoms such as Xe would increase the interaction time between the Rb atom and the noble gas nucleus. The creation of such molecules with Rb and $^3$He are unlikely since the $^3$He velocities are too large for such a formation. Even if the molecule did form, its lifetime would be too short for significant spin exchange to occur. Herman[37] estimated the spin exchange cross section for the Rb-$^3$He system to be $10^{-24}$ cm$^2$.

For a collision between an atom with electron spin $\mathbf{S}$ and a buffer gas with nuclear spin $\mathbf{I}$, the spin exchange Hamiltonian[39] for the two interacting dipoles is

$$H_{SE} = -2\gamma\mu_n\mu_B\Sigma_i\left[\frac{\mathbf{S}\cdot\mathbf{I}}{r_i^3} - 3\frac{(\mathbf{I}\cdot\mathbf{r_i})(\mathbf{S_i}\cdot\mathbf{r_i})}{r_i^5} - \frac{8\pi}{3}\delta(\mathbf{r}_i)\mathbf{S}\cdot\mathbf{I}\right], \tag{3.1}$$

where $\gamma$ is the $^3$He gyromagnetic ratio, $\mu_n$ is the nuclear magneton, $\mu_B$ is the Bohr magneton, $\mathbf{I}$ is the $^3$He nuclear spin, $\mathbf{S}$ is the Rb electron spin and $r_i$ is the distance from the $i$th alkali–metal electron to the noble gas nucleus. The first two terms of equation (3.1) describes the interaction between two

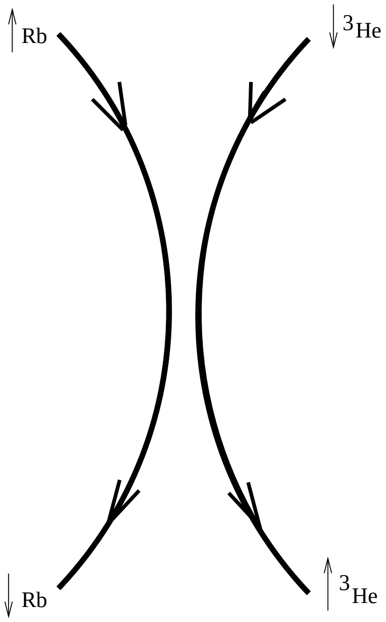

Figure 3-1: Spin–exchange diagram.

point magnetic dipoles and, due to the overlap of the Rb valence electron and the $^3$He nucleus, the last describes the Fermi contact interaction. It is this last term that dominates in the interaction for spin exchange between the Rb valence electron and the $^3$He nuclear spin.

After creating a sample of atomically polarized Rb vapor, spin is then transfered to the nucleus of a $^3$He atom. The rate equation which defines the time evolution of the $^3$He polarization is

$$\frac{d\rho_{He}}{dt} = \left[\frac{\Gamma}{2} + \gamma_{SE}\rho_{Rb}(\frac{1}{2})\right]\rho_{He}(-\frac{1}{2}) - \left[\frac{\Gamma}{2} + \gamma_{SE}\rho_{Rb}(-\frac{1}{2})\right]\rho_{He}(\frac{1}{2}), \tag{3.2}$$

where $\gamma_{SE}$ is the spin exchange rate, $\rho_{Rb}(\pm\frac{1}{2})$ are the normalized Rb population densities for the states $m_{\pm\frac{1}{2}}$, $\rho_{He}(\pm\frac{1}{2})$ are the normalized $^3$He population densities and $\Gamma$ is the total $^3$He relaxation rate. The spin exchange rate is given by $\gamma_{SE} = k_{SE}[\text{Rb}]$, where [Rb] is the Rb number density and $k_{SE}$ is the spin exchange rate constant. Coulter *et al.*[40] reported $k_{SE} = (1.2\pm0.2) \times 10^{-19}$ and Larson *et al.*[41] $k_{SE} = (6.1\pm0.2) \times 10^{-20}$. A recent measurement by Baranga *et al.*[42] found $k_{SE} = (6.7\pm0.6) \times 10^{-20}$ which is in good agreement with Larson *et al.* The rubidium number density can be calculated from the curve given by Killian[43]

$$[\text{Rb}] = \frac{10^{10.55-4132/\text{T}}}{1.38 \times 10^{-16}\text{T}}$$

where [Rb] is in units of cm$^{-3}$ and $T$ is the temperature in Kelvin.

If the initial $^3$He polarization is $P^0_{^3He}$, the solution to equation (3.2) is

$$P_{^3He}(t) = P_{Rb}\frac{\gamma_{SE}}{\gamma_{SE}+\Gamma} + \left[P^0_{^3He} - P_{Rb}\frac{\gamma_{SE}}{\gamma_{SE}+\Gamma}\right]e^{-(\gamma_{SE}+\Gamma)t}, \tag{3.3}$$

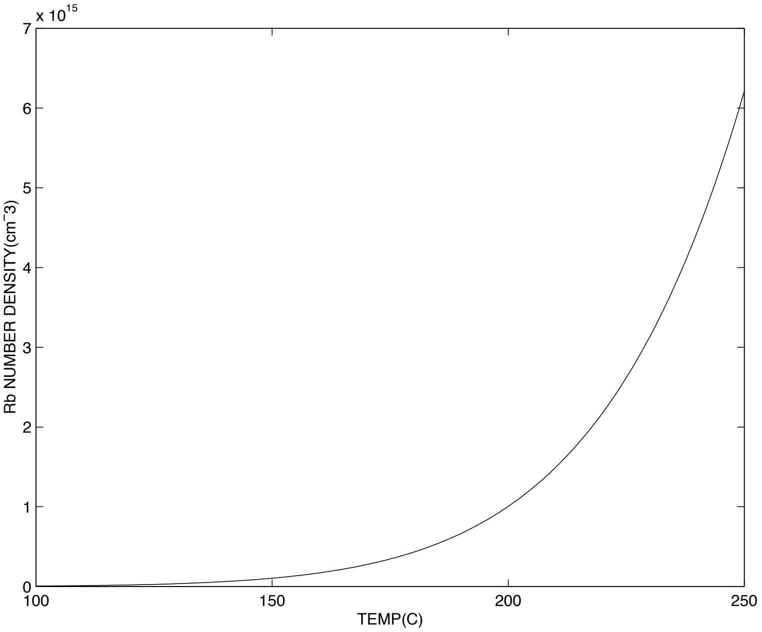

Figure 3-2: Rubidium vapor pressure curve.

where $P_{Rb} = \rho(\frac{1}{2})$-$\rho(\text{-}\frac{1}{2})$ is the Rb polarization. One can see from equation (3.3) that the asymptotic ($t \to \infty$) $^3$He polarization is $P_{Rb}\frac{\gamma_{SE}}{\gamma_{SE}+\Gamma}$ and to achieve high polarization: $\gamma_{SE} \gg \Gamma$ and $P_{Rb} \sim 1$. These requirements can be fulfilled with a sufficient Rb number density, large incident laser light, and cells with long $^3$He lifetimes.

## 3.2 $^3$He Relaxation

From equation (3.3), for high $^3$He polarization the relaxation rate $\Gamma$ must be small compared to the spin exchange rate $\gamma_{SE}$. The three main components that contribute to the relaxation are: interactions with the walls, depolarization due to magnetic field gradients and $^3$He–$^3$He bulk relaxation. The first two are dependent on conditions in the lab, while the third component is dependent on the $^3$He density which is fixed by the constraints of the experiment. The observed relaxation rate is a sum of the individual rates,

$$\Gamma = \Gamma_{wall} + \Gamma_{grad} + \Gamma_{bulk} + \Gamma_{imp},$$

where the terms are for wall, magnetic field gradient, $^3$He–$^3$He bulk, and impurity related relaxation mechanisms respectively. Since care has been taken to achieve high vacuum in the cells before filling and the gases are free of impurities after passing through purifying pumps and cold traps, the last term, $\Gamma_{imp}$, is assumed to be small. However, impurities that are created during the rubidium chasing procedure are not understood, but are hopefully minimized by a careful distilling procedure. It is the wall related relaxation that presents the biggest obstacle for producing cells with high polarization. In the remaining portion of this section, wall, magnetic field gradients, and $^3$He dipole–dipole relaxation mechanisms are discussed. An additional source of relaxation is due to ionizing radiation. The reader is referred to Bonin *et al.*[48] and Coulter *et al.*[49] for a description of the effects a charged particle beam has on $^3$He polarization.

### 3.2.1 Wall Relaxation

The least understood contribution to the relaxation rate is that due to the interaction of noble gas atoms with the walls. At this point it is still a great unknown as to how to prepare cells such that they have predictably long relaxation times. Fitzsimmons *et al.*[50] were the first to investigate surface related relaxation of $^3$He. Their studies included testing of different glass types, of which Pyrex, quarts, and two aluminosilicate glasses were included. They concluded that the two mechanisms, permeation and adsorption, which keep the noble gas nuclei in the vicinity of the glass surface, are the two dominant sources for wall relaxation. Relaxation occurs when the glass contains paramagnetic centers which can interact with the noble gas, causing the nuclear spin to relax. The longer a noble gas atom resides near these paramagnetic impurities the greater the chance its nuclear spin will change its orientation.

The contribution to wall relaxation from permeation is important for glasses containing high amounts of $SiO_2$, such as quartz and Pyrex, since they are more permeable to helium.[52] The structure of these glasses is such that there are openings large enough for helium atoms to permeate. Fitzsimmons *et al* measured a temperature dependence of $^3$He relaxation in glass. For Pyrex and quartz, a peak relaxation time was observed at roughly 125 K; this maximum leads one to believe that different mechanism are at work for the higher and lower temperature regions. Below the peak at low temperatures, the rate of relaxation was attributed to adsorption of the helium onto the glass surface. Since permeation into glass increases with temperature, absorption was thought to explain the increased rate at higher temperatures. To test their theory, Fitzsimmons *et al* measured the $^3$He relaxation temperature dependence in aluminosilicate glass. For aluminosilicate glasses, the structure of the material is such that aluminum ions fill in the openings in the glass, thus reducing permeation of helium. For example, Corning 1720 aluminosilicate glass is roughly three orders of magnitude less permeable than Pyrex. Measuring the temperature dependence for $^3$He in aluminosilicate glass, they found the relaxation time increased with temperature and that there was no maximum. The increase in relaxation time with temperature for impermeable glasses supports the idea that permeation of $^3$He into Pyrex and quartz at higher temperatures is the dominant mechanism for wall related relaxation.

The relaxation of a $^3$He atom which has been absorbed into the glass may in general be a result of three mechanisms:[51] precession of the $^3$He moment about the net local field, magnetic field gradients caused by the magnetic dipoles in the glass, or dipolar coupling between a $^3$He nucleus and a flipping magnetic dipole in the glass. The effect of these mechanisms is to reorient the nuclear spin of the $^3$He atom away from its original direction.

Calculations of relaxation times as a result of absorption of $^3$He gas, are unable to reproduce measured values from cells made from impermeable glass. Timsit *et al.*[51] concluded that the adsorption of $^3$He gas onto a glass surface containing paramagnetic impurities (mainly $Fe^{3+}$ ions) is a likely candidate for the observed relaxation. The Fermi contact term of the spin exchange Hamiltonian of equation (3.1) is not only the major interaction term for spin exchange between noble gas atoms and alkali atoms, but also a sink of angular momentum between a noble gas atom and paramagnetic impurity in the glass. Timsit *et al.* calculated the relaxation time for a $^3$He nucleus near an $Fe^{3+}$ ion on the surface of the glass and found it to be in agreement with measured results. Conclusions from these measurements indicate the need for iron free, helium impermeable aluminosilicate glass to maximize the $^3$He polarization lifetime. Compared to Pyrex, which produces $^3$He lifetimes of a few tens of hours, aluminosilicate glass exhibit lifetimes of up to 100 hours or more. Additionally, aluminosilicate glasses are known to be alkali resistant. Quartz has also been successfully used with long lifetimes even with its high $^3$He permeability due to its low iron content. Corning 7056, a borosilicate glass, has been shown[52] to exhibit long $^3$He relaxation times. Although Corning 7056 is easier for glass blowers to work, the aluminosilicate glasses are preferred for many applications due to their greater strength, higher melting point (useful for charged particle beams), and low permeability to helium.

Heil *et al.*[53] measured relaxation times for $^3$He in cells made from Pyrex and the aluminosilicate glass Supremax,[54] that were internally coated with various metals. Heil *et al* reported that Cesium, bismuth, and lead showed significantly increased relaxation times over that of uncoated Supremax cells, on the other hand magnesium, antimony and zinc did not show improvement. Pyrex cells coated with cesium, bismuth and rubidium also showed a large increase in relaxation time. Bismuth was chosen since it is a diamagnetic material that has a tight lattice structure that may reduce $^3$He permeation to the glass surface. Cesium was chosen since it is capable of repelling $^3$He atoms away from the walls; the attractive potential for helium to the surface of cesium is very weak.[55] The largest increase for both Pyrex and Supremax cells occurred when cesium was used for the coating. Supremax showed the longest relaxation time indicating that the coating was not 100 percent efficient at stopping permeation of helium to the glass. Measurements also confirmed previous results for non–coated cells: reduced relaxation time for Pyrex cells when compared to cells made from the aluminosilicate glass Supremax.

### 3.2.2 Relaxation Due to Inhomogeneous Fields

Magnetic field gradients cause relaxation for moving magnetic dipoles. As a dipole moves through a field gradient it sees a time dependent magnetic field which can couple to the nuclear spin. In the frame of the moving dipole, Fourier components at the resonance frequency $\omega = \gamma \mathrm{B}$ will cause the moment to precess about a direction other than the z–axis, lowering then net magnetization in the sample. The relaxation related to field inhomogeneity has been calculated[38, 56, 57]

$$\Gamma_{grad} = D\frac{|\Delta \mathrm{B_x}|^2 + |\Delta \mathrm{B_y}|^2}{\mathrm{B_z^2}} \tag{3.4}$$

where D is the diffusion constant[1], $\Delta \mathrm{B}_x$ and $\Delta \mathrm{B}_y$ are the gradients of the transverse components of the magnetic field and $\mathrm{B}_z$ is the holding field.

### 3.2.3 $^3$He–$^3$He Magnetic Dipolar Relaxation

Once experimental conditions are such that relaxation is not dominated by wall effects or field inhomogeneity, the limiting factor is due to magnetic dipole–dipole coupling between the $^3$He nuclear spins. During binary $^3$He–$^3$He, collisions the magnetic dipole interaction couples the nuclear spins resulting in a loss of nuclear polarization to the relative orbital angular momentum. Using three different $^3$He–$^3$He interatomic potentials, Newbury *et al.*[58] have calculated the theoretical dipolar relaxation rate for temperatures ranging from 0.1 to 550 K. Their calculated value for the relaxation rate at 23 °C is

$$\Gamma_{bulk} = \frac{[^3\mathrm{He}]}{744} h^{-1},$$

where [$^3$He] is the $^3$He number density normalized to the density at 1 atmosphere and 0 °C.

---

[1] D=1.8±0.2 cm$^2$s$^{-1}$ at P=1 bar and 20°C.[64]

## 3.3 Cell Fabrication

Cell fabrication is an important and, as yet, a not completely understood component of producing polarized $^3$He gas samples. Many steps have been taken to try and remove the unpredictable $^3$He lifetime when producing a sample of polarized gas. It has been suggested that glasses with low concentrations of paramagnetic iron atoms will have longer $^3$He relaxation times than those with higher concentrations. Low permeability of $^3$He into the glass is also thought to increase the polarization relaxation time. Corning 1720 and 1724 aluminosilicate glasses were selected for their resistance to the corrosive effects of alkali metals at high temperatures and for their low permeability to helium. All of the aluminosilicate glass was re-blown to increase the "smoothness" of the walls. It is thought that a rough surfaces contributes to the relaxation of $^3$He polarization by increasing the interaction time of the nucleus with the walls of the glass. Another purpose for reworking the drawn tubing is to strengthen the glass by removing any minute fractures or defects which occurred during the manufacturing of the tubing.

Cells were supplied by two different glassblowers: Anderson Glass Company Inc.[59] and the Princeton University Glassblower shop.[60] Anderson Glass fabricated cells for use in MRI and targets for electron scattering experiments and Princeton made cells that were used for testing purposes and neutron polarizers for experiments at LANSCE.

Very important to the fabrication of $^3$He cells is the use of clean glassware and impurity free gases and rubidium. To produce clean glassware, it was necessary to fabricate a high vacuum system with good conductance between the cells and the pump. Figure 3-3 shows the schematic of the vacuum/filling system. The pumping system was a Balzers TSU 240 turbo–pumping unit. The ultimate achievable vacuum for this unit is approximately 1.0 $\times 10^{-9}$ torr. An oil trap was installed between the turbo pump and the backing pump to reduce the risk of oil back streaming into the vacuum system. In addition, to vent the turbo with argon gas in the event of a power outage, an automatic vent valve was installed. If the system was ever opened for maintenance or upgrading components it was first backfilled with argon to reduce contamination from moisture and dust. To achieve high vacuum all connections were made using Conflat seals or VCR fittings. The vacuum valves were all of the straight–through type to maximize conductance. Also, the valves were constructed with copper gaskets instead of o–rings for high vacuum. Except for the stainless–to–glass connections that were used to connect each cell and rubidium distillery, the entire body of the vacuum system was made from stainless steel. The manifold was wrapped in heat tapes for periodic baking of the system at 100 °C. The raised temperature allows for an increase in the outgasing rate from the walls of the manifold to shorten the time needed to reach a vacuum of at least 1.0 $\times 10^{-8}$ torr. A hot cathode ion gauge and model 919 hot cathode controller from the HPS Division of MKS Instruments, Inc. were used to measure the vacuum in the system. A base vacuum of 5.0 $\times 10^{-9}$ torr was typical after baking.

To make sure that there were no impurities in the cell before filling, the glassware was baked out in an oven under a vacuum of $\sim 1 \times 10^{-8}$ torr at 400 °C for 4 days, followed by 2 days at 200 °C. In an attempt to remove some of the uncertainties in making samples with long polarization lifetimes, an SRS RGA100 residual gas analyzer (RGA) was incorporated into the vacuum system to monitor gas components during the evacuation period. Using spectra from numerous cells, no correlation between observed gas spectra and cell lifetimes were observed. Figure 3-4 shows a typical RGA spectrum at the end of the cell bake–out period. If water and oxygen peaks in the RGA spectrum were significantly above the noise after the bake–out period, the 200 °C bake–out was extended until they were reduced. In addition to monitoring impurities, the RGA also served as a leak checker when connecting new cells.

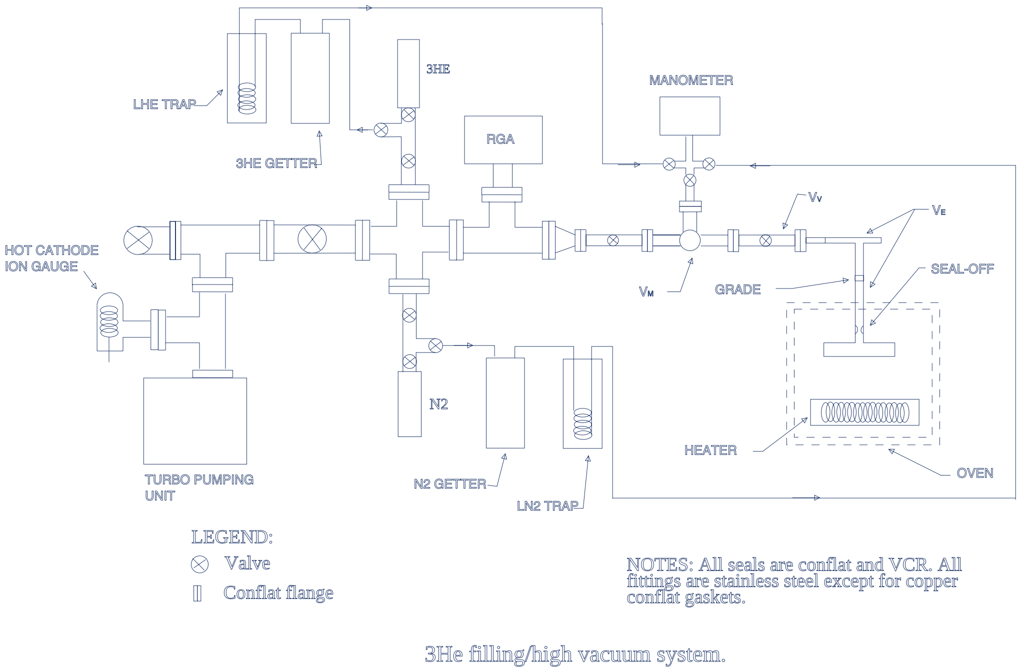

Figure 3-3: Vacuum/filling system.

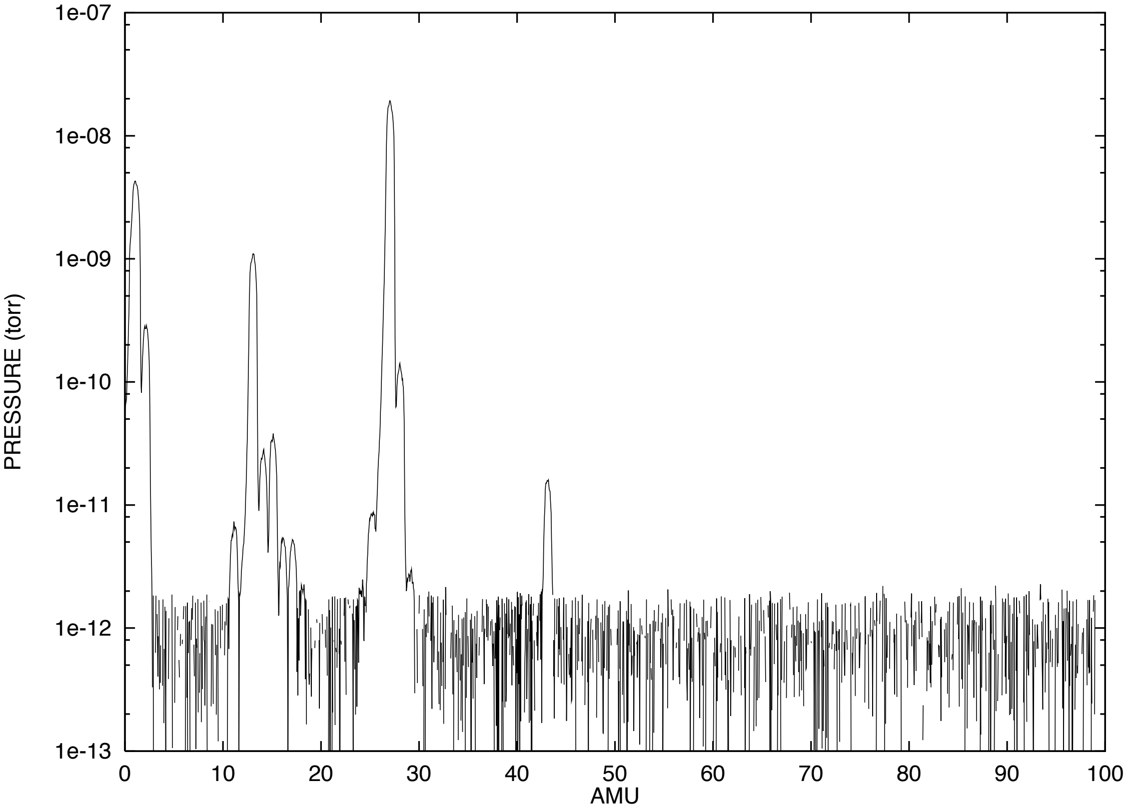

Figure 3-4: Typical RGA spectrum after bake–out.

During the cell bake–out, the Pyrex and grade glass were kept outside of the oven to reduce stress from the different thermal expansion coefficients for the different glasses. In an attempt to try and improve the rate of producing cells with long lifetimes, recent cells were connected to aluminosilicate manifolds and both cell and manifold were placed inside the bake–out oven (see figure 3-5). This reduces the probability of moving impurities into the cell while distilling the rubidium since most of the glass that the rubidium is chased through has been baked under vacuum. The ovens were made from interlocking pieces of Marinite I,[61] a high temperature material rated to 2000 °F. The heat was supplied by two CRFP series ceramic fiber radiant heaters from Omega.[62] The heaters were wired in series, each rated to 300 Watts at 60 V. CN76000 temperature controllers from Omega[62] were used to maintain a constant temperature in the oven. Before baking, all of the glassware was washed with nitric acid for 15 minutes, followed by 4 rinses with De-ionized water. After washing, the cells and glass manifold were quickly fused onto the vacuum system via a glass–to–conflat seal. A diaphragm and dust filter were used to prevent moisture and impurities from entering the system during the fusing procedure. The rubidium was added to the system by breaking open the break–seal on a vacuum packed rubidium ampoule which was then fused onto the glass manifold. Break–seal ampoules were chosen for their higher chemical purity. The newly connected glass manifold was then evacuated using a rotary vane vacuum pump. A trap was used to reduce back-streaming from the vacuum pump. The cell was evacuated for a few hours to make sure that most of the water had been removed from the manifold. The glass manifold was then opened to the high–vacuum system and pumped overnight. If no vacuum leaks were found, some of the rubidium was then distilled from the ampoule into a holding bulb and then the ampoule was removed. In order to minimize the introduction of impurities into the cell the distilling procedure was a necessarily slow and tedious process. Distilling was carried out using a 3 inch yellow flame from a torch. And, rather than driving it in its liquid state which may carry impurities into the cell care was taken to move the rubidium by using an evaporation and condensation process[2].

The vacuum system has three separate ports on the filling manifold for evacuating and filling three separate cells. Each port has its own vacuum valve to separate it from the filling manifold and an up–to–air valve to evacuate the cell with a rotary vane pump before opening the valve to the high vacuum system. The up–to–air valve was also used as a vent for working the glass when fusing the cell to the manifold. Each of the three ports are connected to the "filling manifold" which is valved off from the main manifold during filling. Any cell can be filled independently without disturbing the other cells. Connected to the filling manifold was an MKS Baratron type 122A absolute pressure gauge for measuring the gas pressure. The pressure is monitored with a PDR–D–1 power supply digital readout from MKS. High purity stainless steel bellows valves from Nupro were used for gas handling. These valves are bakeable and are good for high vacuum applications. Both the nitrogen and the $^3$He gases were purified by flowing through their respective SAES GC50 getter pumps. In line with the getter pumps, cold traps were used for further purification. The cold traps consisted of coils of stainless steel tubing submerged in liquid nitrogen for the nitrogen and either liquid nitrogen or helium for $^3$He. The gases were supplied in stainless lecture bottles with stainless steel bellowed valves from Isotec, Inc.,[63] with a chemical purity of 99.9995% and a isotopic purity of 99.9995%. Figure 3-3 includes a flow diagram for the filling system.

After the cells had been baked, the oven was removed and then a small quantity ($\approx$ 100 milligrams) of rubidium was distilled into the cell using the distilling procedure previously discussed. In order to

---

[2] The necessity for clean cell fabrication was supported by refilling a 6 atm cell increasing the relaxation time to $\approx$45 hours from $\approx$10 hours.

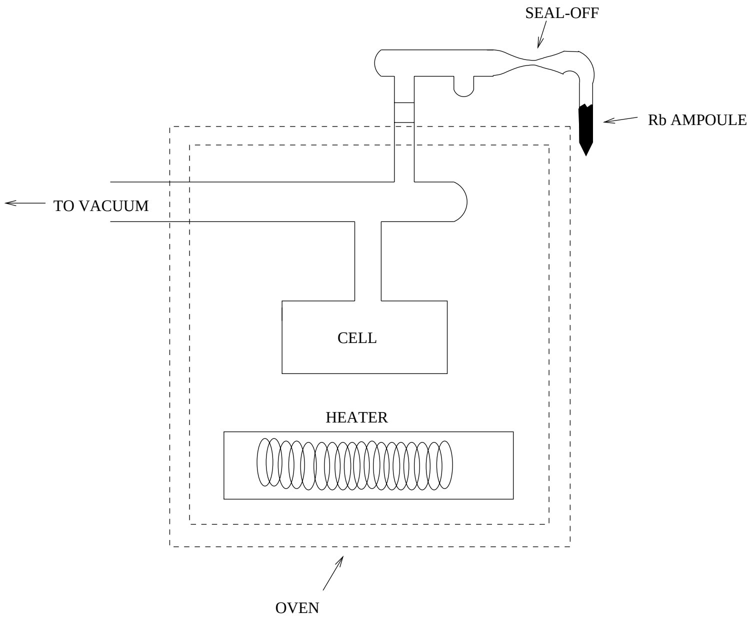

Figure 3-5: Diagram of the cell and glass manifold during bake–out. The Rb ampoule was removed before the bake–out process.

remove any impurities created during the distilling process the cells were then left under high vacuum for 24 hours to remove any impurities created during the distilling process. The getter pumps were turned on and allowed to warm up for 24 hours before use. Just before the cell was filled, all the valves in the system were closed. With all the valves closed, the volume $V_M$ (see figure 3-3) was used as a calibrated volume for filling cells with know quantities of gas.

### 3.3.1 Gas Filling Procedure

The steps taken to fill a particular cell depends on the desired final number density of $^3$He. In order to collapse the glass onto itself during the seal–off procedure, the pressure inside the cell must be lower than atmospheric pressure. To produce cells at higher pressures, cryogenic liquids are used to compress the gas in the cell during seal–off. This dictates a maximum final pressure of approximately 3.5 atmospheres (at 273.15 K) when filling under liquid nitrogen. Final pressures above this value require the use of liquid helium. Each gas was introduced into the manifold volume $V_M$ before filling. To determine the correct manifold pressure, it was assumed at this point that the cell was at either liquid nitrogen or helium temperatures. The manifold filling pressure, $P_M$, needed to produce a final cell pressure of $P_{cell}$ at temperature $T_{final}$ is

$$P_M = \frac{T_g T_{liquid}}{T_{final}} \frac{P_{cell}}{V_M} \left( \frac{V_M + V_V + V_E}{T_g} + \frac{V_{cell}}{T_{liquid}} \right) \tag{3.5}$$

where $T_g$ is the gas temperature in the manifold, $V_M$ is the volume associated with the manifold. $V_V$ and $V_E$ are the volumes associated with the valve and the extra volume between the cell and the valve (see figure 3-3), $T_{liquid}$ is the temperature of either liquid nitrogen or helium.

## Liquid Helium Fill

After closing all the valves, two diode thermocouples were fitted to the cell for monitoring the liquid helium level surrounding the cell. A glass dewar was then placed around the cell on top of a vertical translation table (see figure 3-6). The purpose of this table was to lower the cell and dewar in a controlled manner during the seal–off procedure. It was important to gradually lower the cell as the tubing is collapsing onto itself to form a strong and uniform seal. The dewar is required to maintain the cell at liquid helium temperature to cryogenically compress the gases in the cell to a pressure below 1 atmosphere. If the pressure is below 1 atmosphere the cell can be sealed off with a torch. Custom Styrofoam lids were placed on the dewar with a stainless steel baffle between the cell and the foam to act as a radiation shield. Apezion Q was used to make a tight seal between the lid and the tube connecting the cell to the vacuum system. The lid was then covered with aluminum foil to prevent additional heat loss and also to protect the lid from the torch. The cold–traps were filled with the cryogenic liquids and allowed to reach thermal equilibrium. Using a vacuum sealed transfer line the cell was cooled down to 4.2 K by filling the glass dewar with liquid helium from a storage dewar. Next the nitrogen gas was passed through the getter pump and liquid nitrogen trap and then into the filling manifold. The nitrogen was allowed to flow into the manifold until the pressure reached a value of

$$P_N^m = P_N \frac{V_{cell}}{V_M},$$

where $P_N$ ($\sim$ 100 torr) is the desired final pressure of nitrogen in the cell. Next the valve between the manifold and cell was opened, freezing the nitrogen gas into the cell. The valve was then closed. This procedure was then repeated for $^3$He. However, since the exact temperature of the gas in the cell is not known the final pressure calculation becomes more complicated. The number of atoms in the cell after seal–off is given by

$$N_{cell} = N - N' - N_V - N_E \tag{3.6}$$

where $N$ is the number of atoms in the filling manifold before introducing the gas into the cell, $N'$ is the number of atoms in the manifold after introducing the gas and, $N_V$ and $N_E$ are the number of atoms in the volume between the valve and the seal–off, $V_V + V_E$.

First, an approximate number of atoms in the cell after introduction of the $^3$He gas was calculated:

$$N_{cell} \approx \frac{(P - P')V_M}{kT_g} - \frac{P'(V_V + V_E)}{kT_g} \tag{3.7}$$

where $P$ is the pressure in the filling manifold before introducing the gas, $P'$ is the pressure in the manifold after filling the cell and the valve is closed, $k$ is the Boltzmann constant, and $T_g$ is the gas temperature in Kelvin. Additional fillings of $^3$He can be used to increase the final number density. For $n$ fillings, the total number density in the cell is

$$N_{cell}^n \approx N_{cell}^{n-1} + \frac{1}{KT_g}\Big((P^n - P'^n)V_M + (P'^{n-1} - P'^n)(V_V + V_E)\Big)$$

where $N_{cell}^{n-1}$ is the number density after ($n$-1) fillings.

Since our approximate calculation for $N_{cell}$ does not take into account temperature gradients or any other effects that may change the final number density after the cell is removed, the number of atoms in the cell must be recalculated. To calculate the correct number of atoms in the cell, $N_V$ and $N_E$ in equation (3.6) must be determined. After waiting for the glass to reach thermal equilibrium,

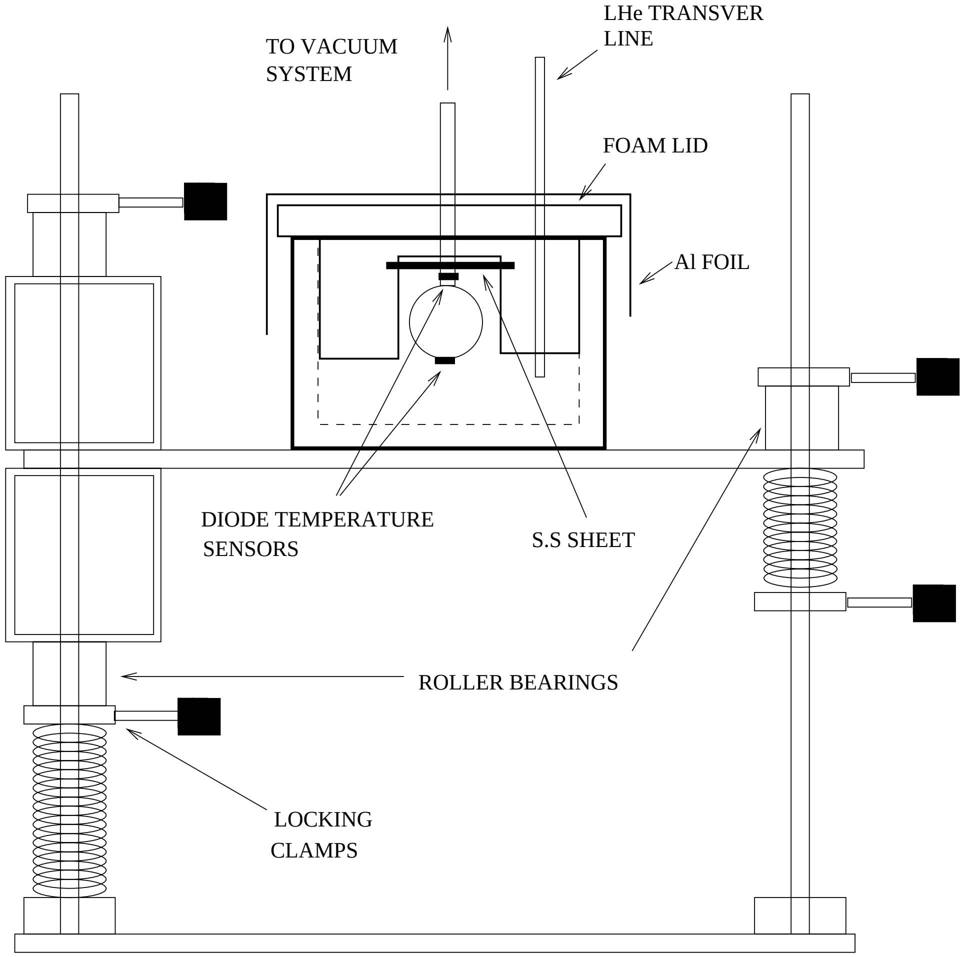

Figure 3-6: Drawing of the high pressure liquid helium filling system. A liquid nitrogen dewar is mounted to a vertically translating table ("ztable") which is used to move the cell down during the seal–off procedure. Locking knobs hold the table down after completing the seal–off. A custom foam lid with a stainless steel radiation shield is used to reduce the rate of liquid helium evaporation. Diode temperature sensors are used to monitor the cell temperature.

the pressure in the manifold volume, $V_M$, $P''$, is re–measured. Then the valve between the filling manifold and the cell manifold is opened and then closed, allowing the gas to come to equilibrium between the volumes $V_M$ and $V_V + V_E$. The final pressure $P'''$ is then measured. Using equation (3.6), the number of atoms in the cell is

$$N_{cell} = \frac{1}{kT}\left(V_M(P - P') - P'''(V_M + V_V + V_E) + P''V_M\right) \tag{3.8}$$

Similarly for $n$ fills, the final number of atoms in the cell is

$$N_{cell} = \frac{V_M}{kT_g}\Sigma_{j=1}^{n}(P_j - P_j') - \frac{1}{kT_g}(P'''(V_M + V_V + V_E) - P''V_m).$$

To compensate for the change in volumes occurred by constricting the seal–off tubing a small correction must be made to $V_E$ and $V_{cell}$ at this point.

## Liquid Nitrogen Fill

In order to compress the gas the cells were submerged in liquid nitrogen to reach a desired final pressures lower than 3.5 atmospheres. After cooling down the cell in liquid nitrogen, the nitrogen gas was introduced at a pressure

$$P = P_N\frac{T_{liquid}}{T_{final}}$$

where $P_N$ was on the order of 100 torr and $T_{liquid}$ is 77 K. Next the $^3$He gas is introduced into the cell until it reached a partial pressure of

$$P = P_{^3He}\frac{T_{liquid}}{T_{final}}.$$

A period of approximately 15 minutes was allowed for mixing of the two gases. The valve to the cell was then closed and the cell sealed off. The final number density in the cell can be calculated in the same manner as the higher pressure case (see equation (3.8)).

In the previous calculations, the volumes $V_{cell}$, $V_M$, $V_V$, and $V_E$ were assumed to be known. The volumes $V_M$, $V_V$, and $V_E$ were measured using several calibrated volumes; the results are given in table 3.1. Several calibrated volumes were needed, since there were two unknown volumes. Once $V_M$ was determined, the cell volume could then be measured. To determine $V_{cell}$ the cell and manifold were evacuated. Then the volume $V_M$ is filled with nitrogen gas and its pressure $P$ was measured. The valve between the cell and the filling manifold was opened to allow for the gas to mix between the two volumes. The valve was then closed and the final pressure $P'$ measured. The total volume $V = V_{cell} + V_V + V_E$ was then determined using

$$V = V_M\left(\frac{P}{P'} - 1\right).$$

After the cell was sealed off the measurement was repeated to determine the volume $V'$=$V_V + V_E$

$$V' = V_M\left(\frac{P''}{P'''} - 1\right)$$

where $P''$ is the pressure in the filling manifold before introducing the nitrogen gas into the volume $V'$, and $P'''$ is the pressure after the gas has been introduced into the volume $V'$. The cell volume

| | |
|---|---|
| $V_M$ | 166.7±.74 |
| $V_V^{left}$ | 43.3±1.8 |
| $V_V^{center}$ | 41.1±1.9 |
| $V_V^{right}$ | 43.3±1.8 |

Table 3.1: Calibrated manifold volume and valve volumes.

can then be calculated

$$V_{cell} = V - V' = V_M\left(\frac{P}{P'} - \frac{P''}{P'''}\right).$$

At this point a correction must be used to compensate for the loss of volume due to constriction of the glass tubing during seal–off (~0.1cm$^3$). The total uncertainty in the final pressure is approximately 0.7%. An additional source of error that is not included in the given uncertainties is the change in volume due to any changes in the location of the bellows in a valve. It is assumed this contribution to the uncertainty is small and, thus, is ignored.

## 3.4 Adiabatic Fast Passage NMR

$^3$He polarization measurements are made using the NMR technique adiabatic fast passage (AFP).[39] As reported in chapter 4, a magnetic moment in a magnetic field $\mathbf{B}_0 = \mathrm{B}_0\hat{\mathbf{z}}$ will precess at an angular frequency $\omega_0 = \gamma\mathrm{B}_0$. In addition, by applying a small rotating magnetic field at a angular frequency $\omega$ an effective magnetic field is produced in the rotating frame

$$\mathrm{B}_{\mathrm{eff}} = \left(\mathrm{B} - \frac{\omega}{\gamma}\right)\hat{\mathbf{z}} + \mathrm{B}_1\hat{\mathbf{x}}'$$

where the angle between the z–axis and the effective magnetic field is given by

$$\tan(\theta) = \frac{\mathrm{B}_1}{\mathrm{B} - \frac{\omega}{\gamma}}.$$

The magnetic moment precesses about the effective magnetic field $\mathrm{B}_{eff}$. By sweeping B from $\mathrm{B} \ll \frac{\omega}{\gamma}$ to $\mathrm{B} \gg \frac{\omega}{\gamma}$, the magnetic moment is rotated through an angle $\theta \approx 180°$. At the resonant condition $\mathrm{B} = \frac{\omega}{\gamma}$, the magnetic moment precesses about a vector in the x–y plane. In the lab frame, the magnetization is observed to precess about the vector $\mathbf{B}_1$ which is rotating about the z–axis at the resonant frequency $\omega_0$. Figure 3-7 shows the time evolution of $\mathrm{B}_{eff}$ in the rotating frame as the magnetic is swept up through resonance.

An oscillating magnetic field of amplitude $2\mathrm{B}_1$ is used to produce a rotating field of amplitude $\mathrm{B}_1$

$$\mathbf{B}_1 = 2\mathrm{B}_1\cos(\omega \mathrm{t})\hat{\mathbf{x}}'$$

where $\mathbf{B}_1$ can be rewritten as two counter rotating magnetic fields

$$\mathbf{B}_1 = \mathrm{B}_1\left((\cos(\omega \mathrm{t})\hat{\mathbf{x}}' + \sin(\omega \mathrm{t})\hat{\mathbf{y}}') + (\cos(\omega \mathrm{t})\hat{\mathbf{x}}' - \sin(\omega \mathrm{t})\hat{\mathbf{y}}')\right).$$

The first term rotates about the z–direction and the second about the negative z–direction. One of

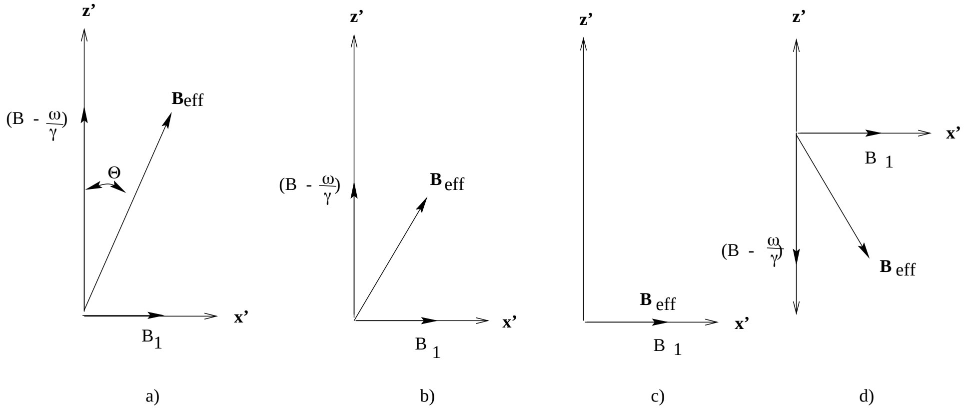

Figure 3-7: Diagram of the AFP process in the rotating frame of $B_1$. In a) the spins are precessing about $B_{eff}$¿$B_1$. As the magnetic field is swept towards resonance, $B_{eff}$ decreases and approaches resonance where in figure c) $B_{eff}$=$B_1$. In figure d) the magnetic has passed through resonance.

these terms rotates in the same direction as the magnetic moment and the other in the opposite direction. The direction of rotation depends on the spin state of the magnetic moment. The oppositely rotating field will have little effect since in the rotating frame it rotates at a frequency $2\omega$, which is far from the resonant condition; its contribution averages to zero over time. The signal detected due to a net magnetization $\mathbf{M}$ is proportional to $dM_T/dt$ where $M_T = \mathbf{M}\cdot\hat{\mathbf{x}}'$ is the transverse component of the magnetization. Calculating $M_T$ gives

$$\mathrm{M_T} = \mu\mathrm{NP}\hat{\mathbf{B}}_{\mathrm{eff}} \cdot \hat{\mathbf{x}}'$$

where $\mu$ is the magnetic moment, $N$ is the number of spins, $P$ is the polarization and $\hat{\mathbf{B}}_{eff}$ is a unit vector pointing in the $\mathbf{B}_{eff}$ direction

$$\hat{\mathbf{B}}_{eff} = \frac{(\mathrm{B} - \frac{\omega}{\gamma})\hat{\mathrm{z}}' + \mathrm{B}_1\hat{\mathrm{x}}'}{\sqrt{(\mathrm{B} - \frac{\omega}{\gamma})^2 + \mathrm{B}_1^2}}.$$

The transverse magnetization is then given by

$$\mathrm{M_T} = \mu\mathrm{NP}\frac{\mathrm{B}_1}{\sqrt{(\mathrm{B} - \frac{\omega}{\gamma})^2 + \mathrm{B}_1^2}}. \tag{3.9}$$

The induced EMF on a set of pick–up coils that have their axes perpendicular to the z–axis will have a magnitude proportional to $M_T$

$$S_{induced} = S_0\frac{\mathrm{B}_1}{\sqrt{(\mathrm{B} - \frac{\omega}{\gamma})^2 + \mathrm{B}_1^2}} \tag{3.10}$$

where $S_0$ is the peak signal amplitude.

The loss of magnetization during the reversal depends on the sweep rate at which the magnetic field is varied, dB/dt. The sweep rate must be slow enough so that the magnetization can follow the effective magnetic field; this is the adiabatic condition. In addition, the sweep rate must be fast enough to keep the magnetization from depolarizing during the reversal; this is the fast condition. If these conditions are met, this method of spin reversal is called adiabatic fast passage (AFP) NMR. The adiabatic condition requires that the time of passage through resonance is long compared to the period of precession about $\mathrm{B}_{eff}$. The extreme condition occurs when $\mathrm{B}_{eff} = \mathrm{B}_1$, ie at the resonance condition. The adiabatic condition is met if

$$\tau = \frac{\mathrm{B}_1}{\left|\frac{d\mathrm{B}}{dt}\right|} \gg \frac{1}{\gamma \mathrm{B}_1}$$

where $\tau$ is the time passage through resonance. The adiabatic condition can be rewritten in the form

$$\frac{1}{\mathrm{B}_1}\left|\frac{dB}{dt}\right| \ll \gamma \mathrm{B}_1.$$

The second condition requires that the sweep rate is fast enough to minimize magnetization losses from relaxation: $\tau \ll T_1$, $T_2$, the longitudinal and transverse relaxation times (see chapter 4). However, since the magnetization is rotating adiabatically with $\mathrm{B}_{eff}$, there is essentially no component of the magnetization that is transverse to $\mathbf{B}_{eff}$. This means that the contribution from $T_2$ relaxation is minimal. The AFP requirements can then be written as

$$\frac{1}{T_1} \ll \frac{1}{\mathrm{B}_1}\left|\frac{d\mathrm{B}}{dt}\right| \ll \gamma \mathrm{B}_1. \tag{3.11}$$

If the sample has been carefully prepared and the relaxation is limited by magnetic field inhomogeneities then in the rotating frame[57]

$$\frac{1}{T_1^r} \approx \mathrm{D}\frac{|\Delta \mathrm{B_z}|^2}{\mathrm{B}_1^2}$$

where D is the $^3$He self diffusion constant[3].

## 3.5 $^3$He Signal Amplitudes

The $^3$He signals from the lock–in were read by the computer and stored for fitting. The data were fit using the form of equation (3.10). The parameterized fit function is

$$S_{fit}(t) = A1 + A2t + \frac{A3}{\sqrt{(t - A4)^2 + A5^2}} \tag{3.12}$$

which is a Lorentzian function of width $A5$, amplitude $\frac{A3}{A5}$, center at $A4$, and on a linear background with slope $A2$ and intercept $A1$. Figure 3-8 shows a typical sweep up data set fit to equation (3.12). Illustrating the quality of the fit, figure 3-8 also shows an expanded view of the data and the fit about the peak. Note the function does not exactly fit the data. Distortions due to field inhomogeneity, the lock–in time constant and other effects will distort the signal from the predicted signal shape. However, the signal amplitude is still proportional to the $^3$He polarization even, if a perfect fitting function is not known. Provided the lock–in time constant is not changed between measurements

---

[3] D=1.8±0.2 cm$^2$s$^{-1}$ at P=1 bar and 20°C.[64]

and the magnetic field inhomogeneities are not changed such as by moving magnetic objects in the proximity of the apparatus, polarization calibration with protons will produce AFP NMR signals of the same shape. The signals from the two lock–in output channels are

$$S_x(t) = -k^{He}\mathrm{M_T(t)G_{coil}G_{pre}^{He}G_l^{He}}\cos(\phi) \tag{3.13}$$

$$S_y(t) = -k^{He}\mathrm{M_T(t)G_{coil}G_{pre}^{He}G_l^{He}}\sin(\phi) \tag{3.14}$$

where $k^{He}$ is a constant that depends on the frequency response of the lock–in and the cell geometry, $\mathrm{M}_T(\mathrm{t})$ is the transverse polarization (equation (3.9)), $G_{coil}$ is the pick–up coil gain, $G_{pre}$ is the pre–amplifier gain, $G_l^p$ is the lock–in gain and $\phi$ is relative the phase of the input signal to that of the lock–in reference phase. The peak amplitude of the $^3$He signal is

$$S_{He} = \mu_{He}N_{He}P_{He}k^{He}G_{coil}G_{pre}^{He}G_l^{He} \tag{3.15}$$

where $\mu_{He}$ is the $^3$He magnetic moment, $N_{He}$ is the number of $^3$He atoms in the sample and $P_{He}$ is the $^3$He polarization.

The sweep rate was approximately 0.5 gauss/s and $\mathrm{B}_1$ is $\approx$ 30 mgauss for the $^3$He NMR data. Using these quantities, equation (3.11) gives

$$\approx 0.01 \ll 16.7 \ll 97.3$$

which satisfies the AFP requirements. Losses occurred during NMR measurements were on the order of 0.1% or less.

## 3.6 Proton Calibration

The $^3$He polarization was determined using an AFP NMR signal from hydrogen protons in water and their known thermal Boltzmann polarization. The calibration was accomplished using a cell filled with De-ionized water, which had a nearly identical geometry as the $^3$He cell. It was important to maintain the frequency and lock–in time–constant when acquiring data with $^3$He and water. The lock–in and pre–amplifier gain is changed to account for the much smaller signal from protons. It is also important to place the cells in the same location in the NMR apparatus. Signals from the two lock–in output channels can be written in the form

$$S_x(t) = -k^p\mathrm{M_T(t)G_{coil}G_{pre}^{p}G_l^{p}}\cos(\phi) \tag{3.16}$$

$$S_y(t) = -k^p\mathrm{M_T(t)G_{coil}G_{pre}^{p}G_l^{p}}\sin(\phi) \tag{3.17}$$

where $k^p$ is a constant that depends on the frequency response of the lock–in and the water cell geometry. If the $^3$He and water cells have identical geometries and the lock–in time constant is not changed then $k = k^p = k^{He}$, the peak amplitude of the proton signal is of the form

$$S_p = \mu_p N_p P_p k^p G_{coil}G_{pre}^{p}G_l^{p} \tag{3.18}$$

where $\mu_p$ is the magnetic moment of the proton, $N_p$ is the number of protons in the sample, and $P_p$ is the proton polarization

$$P_p = \tanh\left(\frac{\mu_p \cdot \mathbf{B}}{kT}\right) = \tanh\left(\frac{\hbar\omega}{2kT}\right).$$

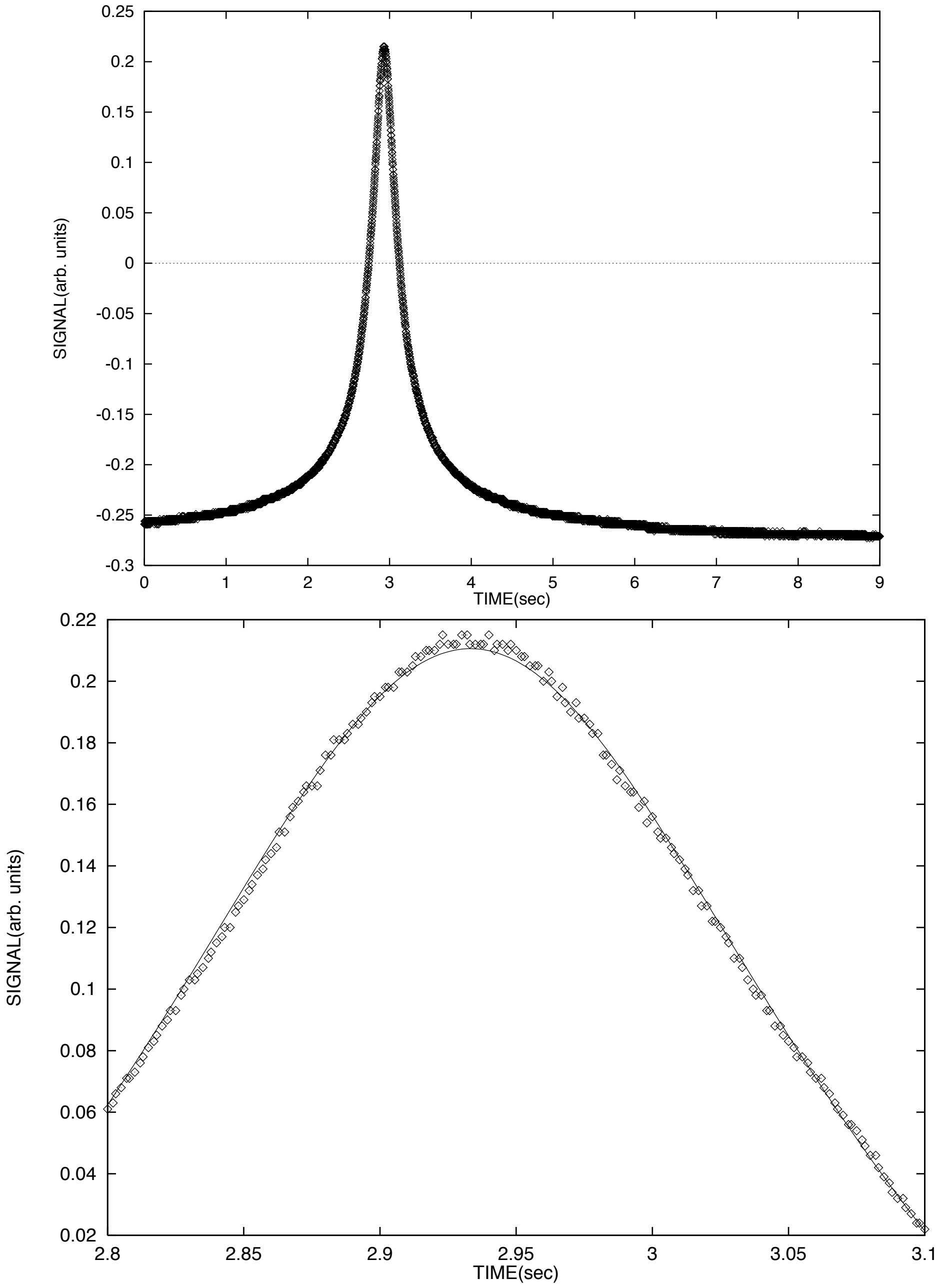

Figure 3-8: The top figure is a sample $^3$He AFP NMR data set for an "up" sweep. The data are represented by symbols and the fit by the solid line. The fitting parameters are A[i]=-.27911, -.000314, .06372, 2.933, .1299. The uncertainty in the amplitude is 0.2%. The bottom figure is an expanded view of the data and fit.

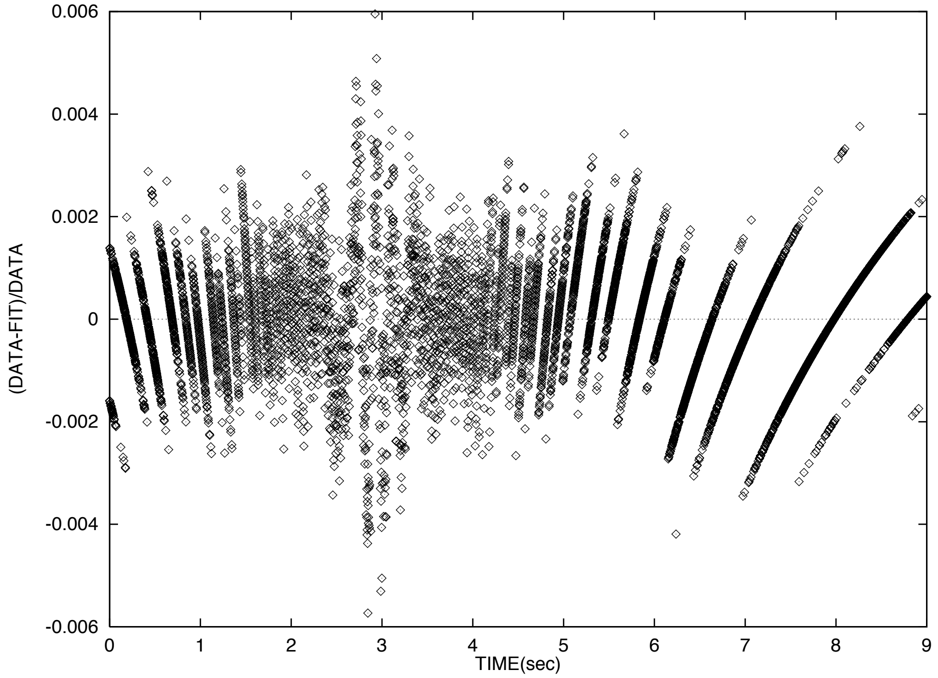

Figure 3-9: The difference between the data and the fit to a Lorentzian function.

If $k_p = k_{He}$, $k$ can be measured from the proton signal amplitude and substituted into equation (3.15) to determine the $^3$He polarization

$$P_{^3He} = P_p \frac{S_{He}}{S_p} \frac{\mu_p}{\mu_{He}} \frac{N_p}{N_{He}} \frac{G^p_{pre} G^p_l}{G^{He}_{pre} G^{He}_l}. \tag{3.19}$$

### 3.6.1 Proton NMR Measurement

Due to the low proton polarization at these fields ($P_p \approx 7.7 \times 10^{-7}\%$) measurement of the proton NMR signal is difficult. The proton signal is approximately $5 \times 10^{-5}$ times smaller than the signal from a 1 atmosphere sample of $^3$He polarized to 50%. Signal averaging is used to increase the signal–to–noise ratio. In addition to electrical noise, the signal also contains a component from RF pick–up due to $B_1$. This pick–up is large compared to the water signal, thus requiring its subtraction at the input of the lock–in using the phase–shifter amplifier discussed in section 3.7. The RF pick–up also is in the form of noise due to motion within the NMR apparatus from acoustic and vibrational coupling. Figure 3-10 is a single acquisition "up" data set with a signal-to-noise ratio of approximately 1. Figure 3-11 shows sample data sets for signal averaged "up" and "down" sweeps. The NMR parameters are given in table 3.2. To allow for the polarization to relax to its equilibrium value the "up" and "down" data are acquired with a 20 second pause between acquisitions. The inversion of the "up" and "down" data is a consequence of the protons relaxing between sweeps, and the signal depends on the rate of change of the magnetic field B and the direction of the polarization.

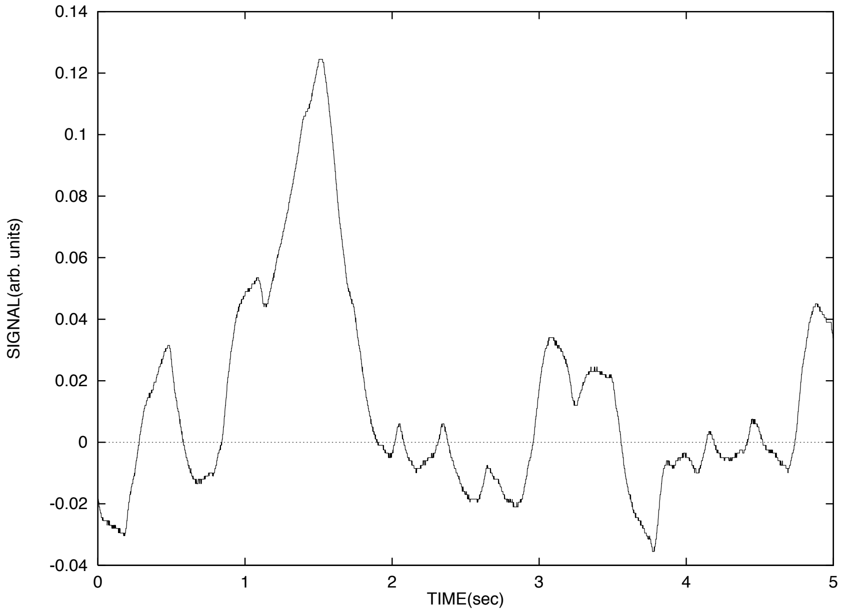

Figure 3-10: A single proton "up" sweep AFP NMR data set.

### 3.6.2 Proton NMR Data Analysis

Since the relaxation time of protons in water (on the order of 3 seconds) is comparable to the sweep rate, relaxation cannot be ignored during AFP. To include relaxation, the Bloch equations[39] were used to describe the time evolution of the magnetization. In the rotating frame the Bloch equations are

$$\frac{dP_x}{dt} = \gamma P_y(\mathrm{B(t)} - \frac{\omega}{\gamma}) - \frac{\mathrm{P_x} - \chi \mathrm{B_1}}{\mathrm{T_2}} \tag{3.20}$$

$$\frac{dP_y}{dt} = \gamma P_z \mathrm{B_1} - \gamma \mathrm{P_x}(\mathrm{B(t)} - \frac{\omega}{\gamma}) - \frac{\mathrm{P_y}}{\mathrm{T_2}} \tag{3.21}$$

$$\frac{dP_z}{dt} = -\gamma P_y \mathrm{B_1} - \frac{\mathrm{P_z} - \chi \mathrm{B(t)}}{\mathrm{T_1}} \tag{3.22}$$

where

$$\mathrm{B(t)} = \beta \mathrm{t} + \mathrm{B_i},$$

$T_1$ and $T_2$ are the longitudinal and transverse relaxation times, $\mathrm{B}_i$ is the initial magnetic field, and $\chi = \mu_p/kT$. If $\mathrm{B_1} = 0$, the polarization is given by $P = \chi \mathrm{B}$ (see equation (4.2)).

The signal shape is dependent on the transverse magnetization. As the magnetic field is swept, the effective magnetic field seen in the rotating frame is

$$\mathbf{B}_{eff} = (\beta t + \mathrm{B_i} - \frac{\omega}{\gamma})\hat{\mathbf{z}}' + \mathrm{B_1}\hat{\mathbf{x}}'.$$

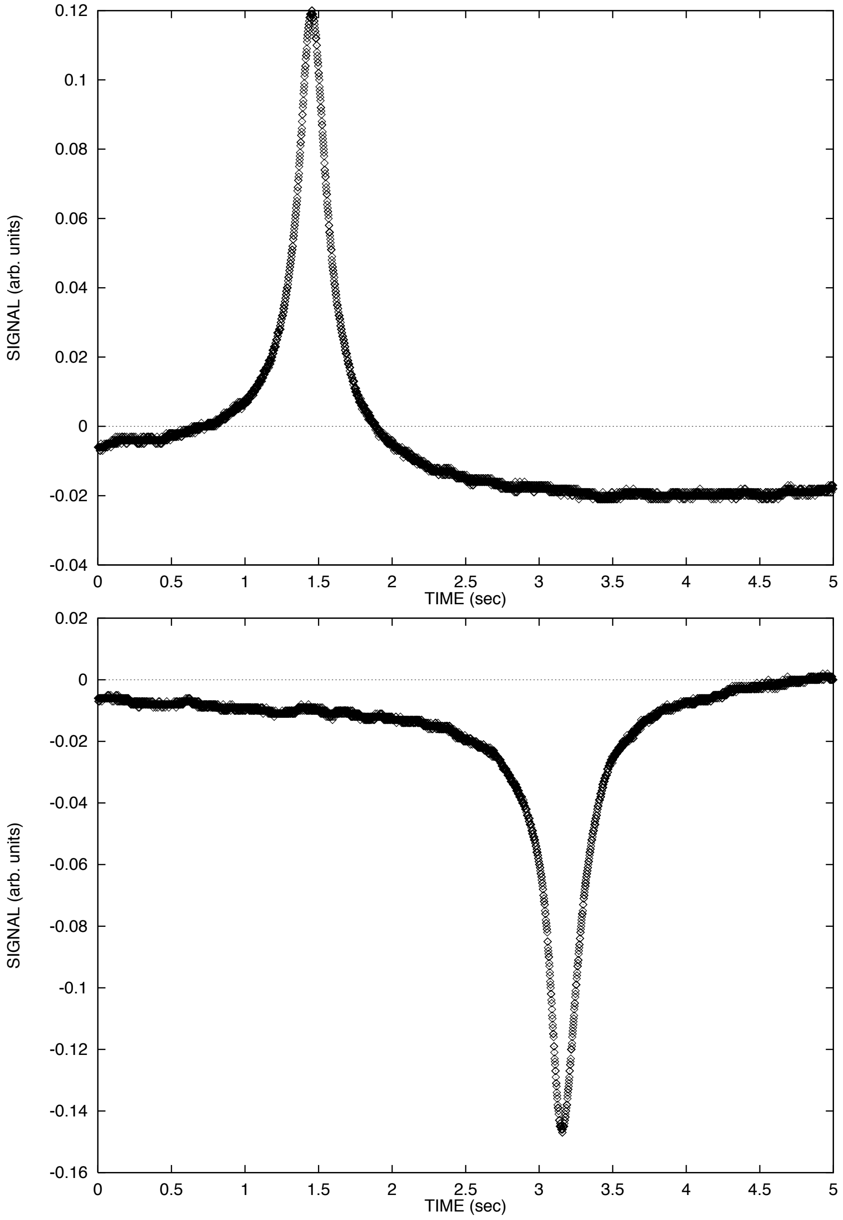

Figure 3-11: The top figure is a proton AFP NMR "up" data using 100 signal averaging sweeps. The bottom figure is a "down" data set.

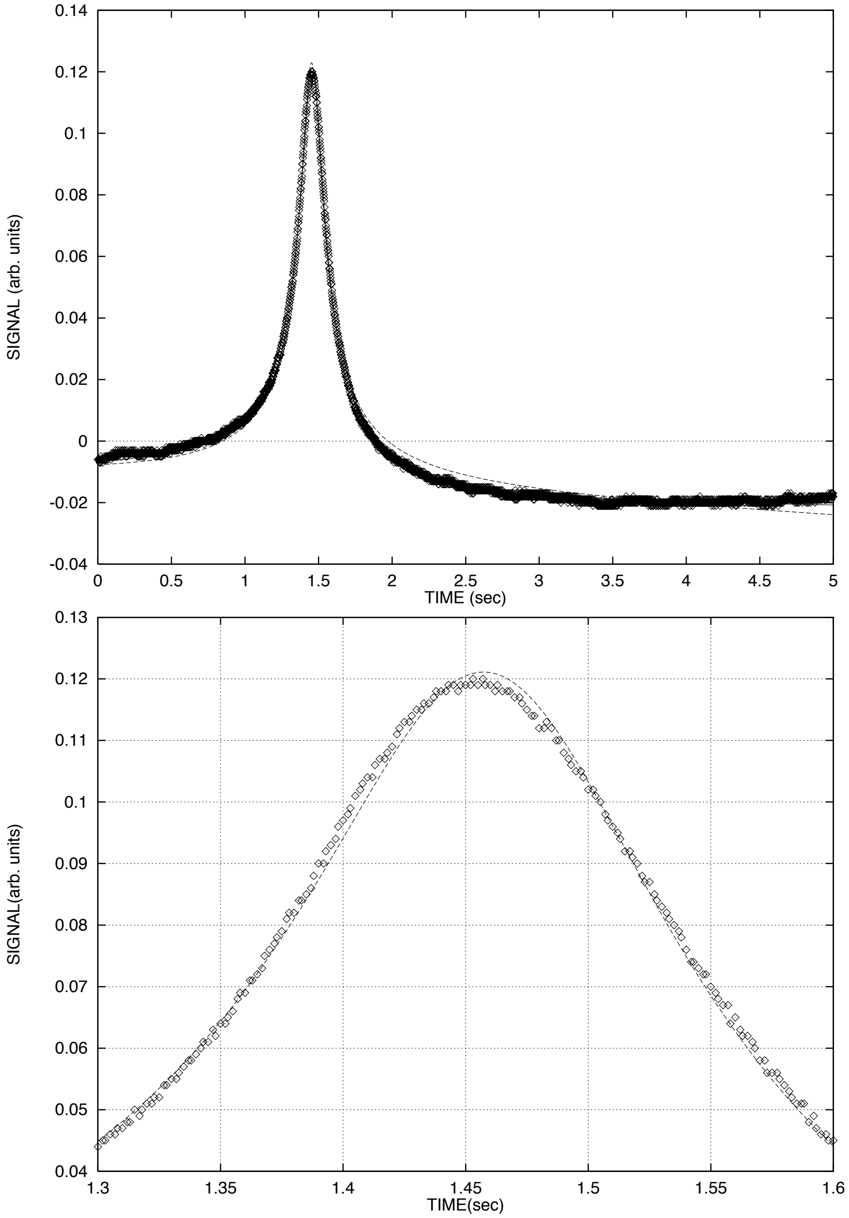

Figure 3-12: The top figure is a Proton "up" data set with 100 signal averages. The dashed line is a fit to the data using equation (3.12). The solid line is a fit taking into account the time evolution of the polarization during acquisition. The bottom figure is an expanded view of the data and the fit including relaxation.

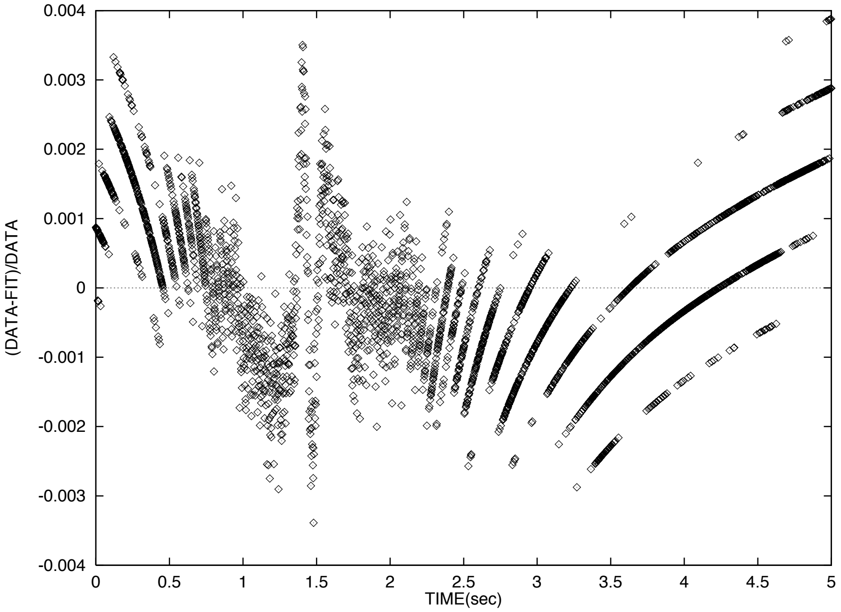

Figure 3-13: A plot of the difference between the proton data and the fit including relaxation.

The polarization in the direction of $\mathrm{B}_{eff}$ is given by

$$P_{thermal} = \tanh\left(\frac{-\mu\hat{\mathbf{B}}_{eff}\cdot\mathbf{B}_{tot}}{kT}\right) \approx -\frac{\mu\hat{\mathbf{B}}_{eff}\cdot\mathbf{B}_{tot}}{kT} \tag{3.23}$$

where

$$\mathbf{B}_{tot} = (\beta t + \mathrm{B_i})\hat{\mathbf{z}}' + \mathrm{B_1}\hat{\mathbf{x}}'$$

and $\hat{\mathbf{B}}_{eff}$ is the unit vector pointing in the direction of $\mathbf{B}_{eff}$

$$\hat{\mathbf{B}}_{eff} = \frac{(\beta t + \mathrm{B_i} - \frac{\omega}{\gamma})\hat{\mathbf{z}}' + \mathrm{B_1}\hat{\mathbf{x}}'}{\sqrt{(\beta t + \mathrm{B_i} - \frac{\omega}{\gamma})^2 + \mathrm{B_1^2}}}.$$

Rewriting $P_{thermal}$ gives

$$P_{thermal}(t) = -\frac{\mu}{kT}\frac{\mathrm{B(t)}\left(\mathrm{B(t)} - \frac{\omega}{\gamma}\right) + \mathrm{B_1^2}}{(\mathrm{B(t)} - \frac{\omega}{\gamma})^2 + \mathrm{B_1^2}}. \tag{3.24}$$

If the magnetic field was swept until time t, $P_{thermal}$ is the asymptotic polarization in the direction of $\hat{\mathbf{B}}_{eff}$. Equations (3.22) were integrated to calculate the proton polarization $P_{eff}$ with respect to $\mathbf{B}_{eff}$, as the magnetic field was swept from some initial value $\mathrm{B}_i$ to a final value $\mathrm{B}_f$. The integration was carried out with a program written in FORTRAN utilizing a modified midpoint method.[44] The data were then fit with a FORTRAN program using the Levenberg-Marquardt method[44] and the

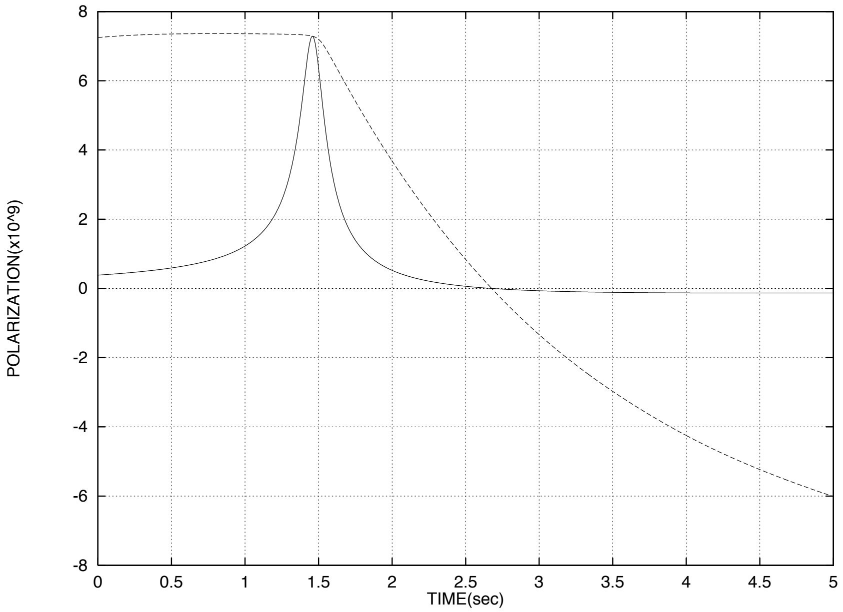

Figure 3-14: Numerical simulation of the proton polarization as the magnetic field is swept through resonance. The solid line is the transverse component of the polarization and the dashed line is the proton polarization with respect to $\mathbf{B}_{eff}$.

function[4]

$$A1 + A2t + \frac{A3}{\sqrt{(t-A4)^2 + A5^2}} P_{eff}(t). \tag{3.25}$$

If the proton AFP data were fit to a Lorentzian function (ignoring relaxation), the corresponding signal amplitude was over estimated by 4.3%.

The longitudinal relaxation rate of protons in water is on the order of $T_1 = 3$ seconds. Meiboom[45] has shown that $T_2 < T_1$ for protons in natural water due to the presence of 0.037% $^{17}$O. $^{17}$O has a spin of $\frac{5}{2}$ and has been shown by Meiboom to be the dominant factor in splitting the proton resonance by spin–spin interaction. Nuclei that are in the presence of different magnetic environments will precess at different frequencies. Each location (frequency) will then correspond to a different line in frequency space. By exchanging protons between different oxygen atoms, several resonance line are created and an effective broader linewidth is observed thus producing a shorter $T_2$. For proton resonance in water using the Bloch equations and including exchange, Meiboom calculated the relationship between $T_1$ and $T_2$ in the presence of an RF field

$$\frac{1}{T_2} - \frac{1}{T_1} = \tau \Sigma_i \frac{P_i \delta_i^2}{1 + \tau^2(\delta_i^2 + \omega_1^2)} \tag{3.26}$$

where $\tau$ is the average lifetime a proton is bonded to a specific oxygen atom ($^{16}$O, $^{17}$O, or $^{18}$O), $P_i$ is the relative intensity of the $i$th line, $\delta_i$ is the separation of the $i$th line from the dominant line, and

---

[4] $P_{eff}$(t) has been normalized such that $P_{eff}$(0)=1.

| Parameter | Value | Units | Uncertainty(%) |
|---|---|---|---|
| $P_p$ | $7.66 \times 10^{-7}$ | % | 1.2 |
| $B_{init}$ | 21.3 | gauss | 1.0 |
| dB/dt | $\sim$0.9 | gauss/s | – |
| $\mu_p/\mu_N$ | 2.79285 | – | – |
| $\mu_{He}/\mu_N$ | 2.12762 | – | – |
| $N_p$ | $4.67 \times 10^{24}$ | $cm^{-3}$ | 1.2 |
| Temp | 297 | Kelvin | 0.7 |
| Pre–amp gain | 200 | – | 1.1 |
| Lock–in gain | 1000 | – | 1.1 |
| Lock–in time const. | 30 | ms | – |
| $\nu_0$ | 95 | kHz | – |
| $B_1$ | $\sim$30 | mgauss | 5.0 |
| Signal Averages | 100 | – | – |

Table 3.2: Proton AFP NMR parameters.

$\omega_1 = \gamma B_1$ is the radial frequency about the RF field $B_1$. Using the given quantities

$$\frac{1}{T_2} - \frac{1}{T_1} = 0.082$$

for $B_1 = 30$ mgauss. The value of $T_1 = 2.1$ was determined by optimizing the fit to the AFP NMR data. The difference between the value from the best fit to the approximate value quoted above may be attributed to a temperature difference and contamination of the water sample.

### 3.6.3 Polarization Calibration Uncertainties

From equation (3.19), the $^3$He polarization can be calculated from the signal amplitudes that were extracted from a fit to the data. Table 3.2 lists all the relevant quantities and their uncertainties needed to determine the $^3$He polarization. The proton polarization uncertainty was determined using the uncertainties in the temperature and the holding field $B_{init}$. $B_{init}$ was determined by changing the resonant frequency $\nu_0$ and measuring the shift in the peak of the AFP NMR signal. The uncertainty in the number of protons was calculated using an uncertainty in the temperature and a 1% uncertainty in the volume of the water sample. The uncertainties in the lock–in and pre–amplifier gain were measured by connecting the output of the pre–amplifier to the input of the lock–in and comparing the net gain for different lock–in and pre–amplifier gains so that their ratio was held constant. The uncertainties in the signal amplitudes were determined using the calculated covariance matrix elements from the fitting routine[44] which corresponded to the fit amplitude. The uncertainties for the data points were determined from the data and entered into the fitting routine. The error in the proton signal amplitude is approximately 0.6% and 0.2% for the $^3$He amplitude. The above uncertainties result in a total error of 2.9% in the $^3$He polarization.

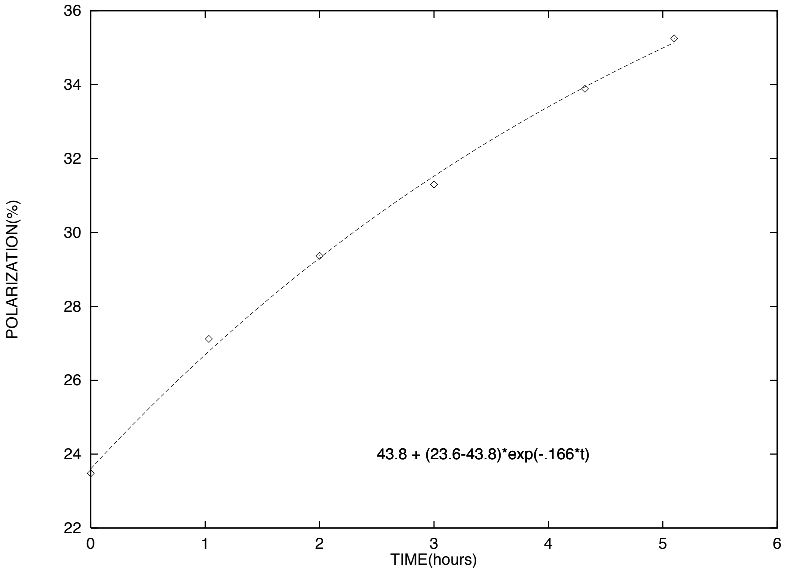

Figure 3-15: Polarization ramp up data for cell LA2 (see table 5.2) using 2.3 W from a Ti:Sapphire laser and 15 W from a fiber coupled laser diode.

### 3.6.4 $^3$He Polarization Time Dependence.

The time evolution of the $^3$He polarization is given by equation (3.3)

$$P_{^3He}(t) = P_{Rb}\frac{\gamma_{SE}}{\gamma_{SE}+\Gamma} + \left[P^0_{^3He} - P_{Rb}\frac{\gamma_{SE}}{\gamma_{SE}+\Gamma}\right] e^{-(\gamma_{SE}+\Gamma)t}. \tag{3.27}$$

Figure 3-15 is a plot of the polarization ramp up data for a cylindrical cell containing 3 atmospheres of $^3$He and 100 torr of nitrogen (cell LA2, see table 5.2). A Ti:Sapphire laser delivering 2.3 W and a 15 W fiber coupled diode were used for the optical pumping. The data were fit to equation (3.27) and represented by the dashed line in the figure. The asymptotic polarization for this particular cell and pumping conditions was 43.8±1.3% with a time constant of ~6 hours.

Figure 3-16 is the time evolution of the polarization in a ~ 3 atmosphere spherical cell polarized with a diode laser at 170 °C. After polarizing for approximately 9 hours the polarization was flipped into the other state while the polarizing continued. The data were fit to equation (3.27).

If there is some initial polarization and the number density of rubidium is roughly zero then the time evolution of the polarization is governed by

$$P_{^3He}(t) = P^0_{^3He}e^{-\Gamma t}.$$

Relaxation rates are measured by observing the decay of polarization with the sample at room temperature. Figure 3-17 is the relaxation data for a 2.5 cm diameter spherical cell made from GE 180[46] containing 3.2 atmospheres of $^3$He. Corresponding to a 352 hour contribution from relaxation mechanisms other than $^3$He–$^3$He dipole interaction (section 3.2.3) the lifetime of this cell is roughly 140 hours. Similar cells made from Supremax glass exhibited even longer lifetimes.

An interesting observation was made using two cells that exhibited poor relaxation times ($<$

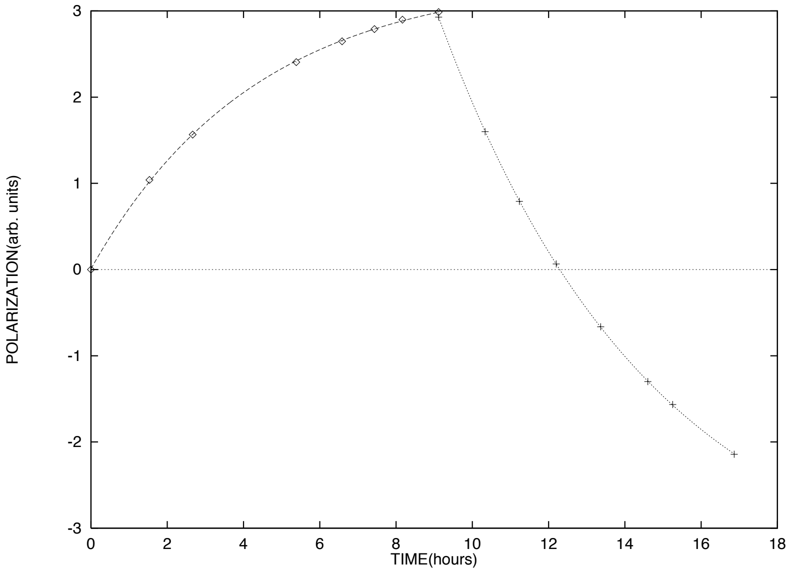

Figure 3-16: Time evolution of the polarization of a spherical cell at 170 °C. The cell is polarized in one state for approximately 9 hours and then flipped into the other state while still polarizing the initial state. The points represent the data and the solid lines are fits to the data.

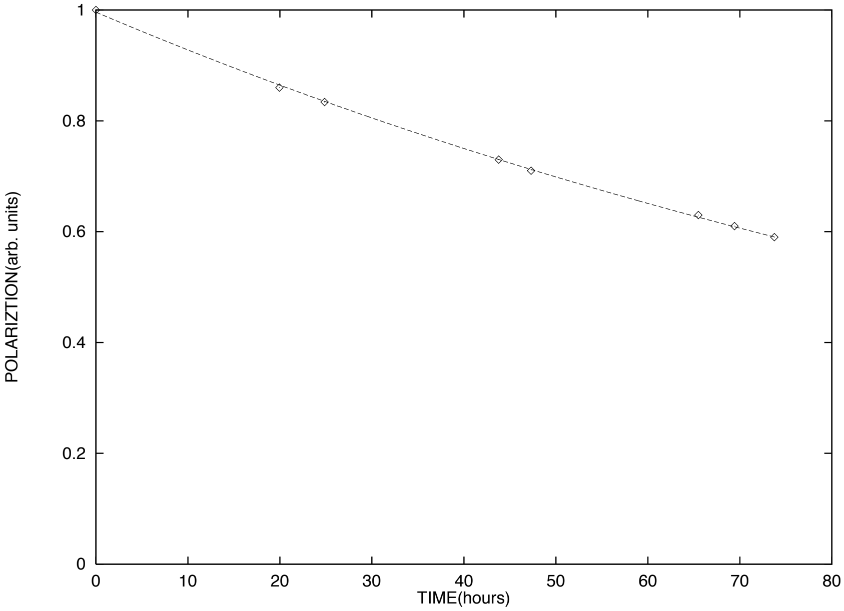

Figure 3-17: Relaxation data for a 3.2 atmosphere spherical cell made from GE 180. The solid line is an exponential fit to the data with a relaxation time of approximately 140 hours.

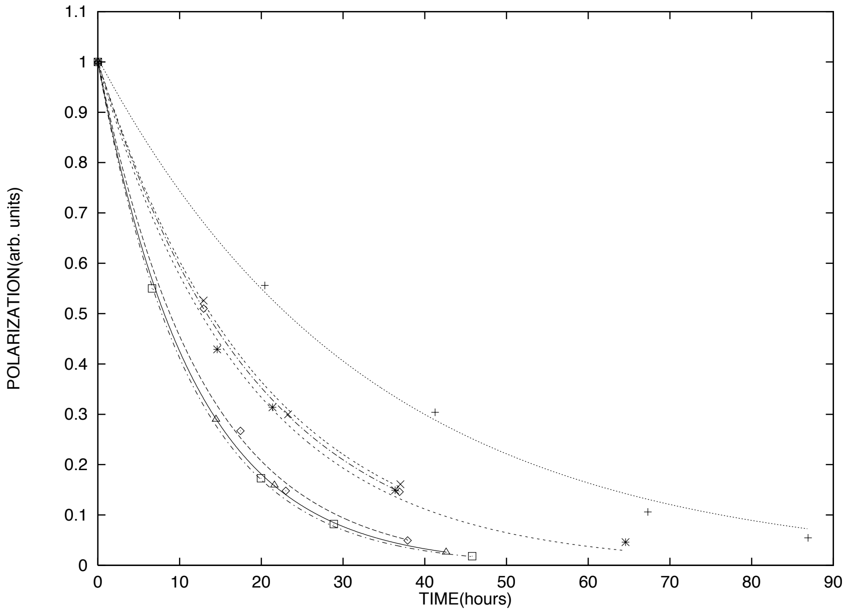

Figure 3-18: Relaxation data for a spherical cell containing $\sim$ 3 atmospheres of $^3$He. Each curve corresponds to a measurement of the decay of polarization with the cell in a different orientation.

30 hours at 3 atmospheres). Relaxation in these cells appeared to have an orientation dependence. Figure 3-18 is the relaxation data from a 3 atmosphere spherical cell made from 1720 aluminosilicate glass. Each curve corresponds to a measurement of the relaxation rate with the cell in a random orientation. As a cell is cooling down, gravity causes rubidium to puddle in the bottom of the cell. Since the rubidium would cover different regions of the glass surface and thus cover good and bad regions of the glass depending on the cells orientation this would explain the position dependence to the relaxation time. A bad region would be one that has a paramagnetic impurity embedded at the surface, which would cause depolarization of $^3$He. Cells with extended relaxation times have not been observed to exhibit such an effect.

## 3.7 $^3$He Polarization Apparatus

The apparatus used for adiabatic fast passage (AFP) nuclear magnetic resonance (NMR) is shown in figure 3-19. The holding field $\mathbf{B_0}$ is produced by a pair of 2.02 meter diameter coils placed in Helmholtz configuration. Each coil contains 126 turns of number 9, square magnet wire resulting in a field of $\approx$1.12 gauss per ampere of current. The current in the coils is provided by a Hewlett Packard 6012A dc power supply that is remotely controlled by the data acquisition computer. Figure 3-20 shows calculations for $\Delta$B/B as a function of position. A second AFP NMR apparatus is shown in figure 3-21. This apparatus was originally designed to be used at the Saskatchewan Accelerator Laboratory to provide the field needed for a polarized $^3$He target. Available space constrained the size of the coils and thus necessitated a configuration other than Helmholtz to produce a uniform field over the available volume. The coils were wound with number 6 magnet wire. The smaller coils have a diameter of 36 cm and contain 90 turns. The larger pair have a diameter of 83 cm with 100 turns. The field produced is $\approx 2.66$ Gauss per ampere of current. Figure 3-22 shows a calculation of $\Delta B/B$ produced by this coil configuration.

Perpendicular to the holding field $\mathbf{B}_0$ is an oscillating field $\mathbf{B}_1$, that is needed for AFP. $\mathbf{B}_1$ is produced by a pair of RF coils wound onto a PVC form with a near Helmholtz configuration: the diameter is 31.7 cm, separation 15.5 cm and each coil has 4 turns of number 20 magnet wire. A custom power amplifier was fabricated using an LM3886 audio amplifier IC from National Semiconductor to drive the RF coils. The IC has the ability of delivering 68 Watts into a 4 ohm load in the audio region. Figure 3-23 shows the circuit used in the RF amplifier. The input to the amplifier came from the internal oscillator of an NF Electronic Instruments 5610 double phase lock-in amplifier. The frequency range of this oscillator extends up to 120 kHz.

The AFP NMR signal is produced by the EMF induced in the pick–up coils. These coils are wound on Nylatron GS rectangular frames, and mounted on either side of the oven. The pick–up coil frames are 5 cm high, 7.5 cm wide, with 6 mm wide groves that are 7 mm deep. They are separated 7.9 cm from center to center. Each coil has 200 turns of number 28 magnet wire. The coils are center tapped to ground (see figure 3-24) with the outer leads connected to a Stanford Research Systems SR560 pre-amplifier to amplify the difference of each input. A capacitor was connected across the pickup coils to produce a resonant circuit tuned to the Larmor frequency. A quality factor, Q, of $\sim$60 was measured. Different capacitors with the same value of capacitance produce coils with varying Q. It was found that temperature ultra–stable capacitors produced coils with a higher Q than standard capacitors. It was thought that the internal resistance varies from capacitor to capacitor with the temperature stable capacitors having the lowest resistance. The signal output from the pre-amplifier was fed into one of the inputs of the lock–in amplifier. In order to subtract any unwanted pick–up from the RF coils, the other input to the lock–in came from a custom phase–shifter amplifier. This unwanted signal is due to imperfect symmetry of the pick–up coils and, therefore, it is difficult to position them so that complete cancelation will occur. The unwanted signal is amplified by the pre-amp and subtracted by the lock–in. The phase–shifter circuit diagram is shown in figure 3-26.

The data acquisition and polarization control was accomplished by an IBM pc computer with a National Instruments LAB–PC+ data acquisition (DAQ) card. The acquisition software was written using LABVIEW for Windows from National Instruments.[47] The computer controlled the holding magnetic field by sending a voltage signal to the dc power supply. The power supply was set up to run in current regulation mode, which produced 10 Amperes of current for a 1 V signal from the computer. During acquisition, the magnetic field was swept from just below to just above resonance. As the field was swept through resonance, the magnetization rotated through and angle of approximately 180°. Ramp rates, sample rates, and the number of scans were set in the software. The sample rate was 600 Hz.

Since the proton polarization is very small ( $7 \times 10^{-7}\%$), it was necessary to use signal averaging to increase the signal-to-noise ratio. The $^3$He signal was much larger than that from protons in water and, consequently, signal averaging was not needed for $^3$He. The DAQ card supplied two voltage signals, one to ramp the current and the other as a trigger pulse for the acquisition. The trigger was read by one of the input channels, and the X and Y outputs of the lock–in were read by two other channels. The two input channels were stored into a circular buffer. LABVIEW was instructed to acquire data when the falling edge of the trigger pulse had crossed a certain threshold. A problem due to interrupts, such as those made by moving the mouse or using the keyboard, caused noise spikes on the input channels of the DAQ card that were several hundred millivolts in amplitude. These spikes were large enough to trigger the data acquisition. To overcome this, the inputs to the DAQ card were run in differential mode; this limited the maximum input to 1 volt, however eliminating false triggers.

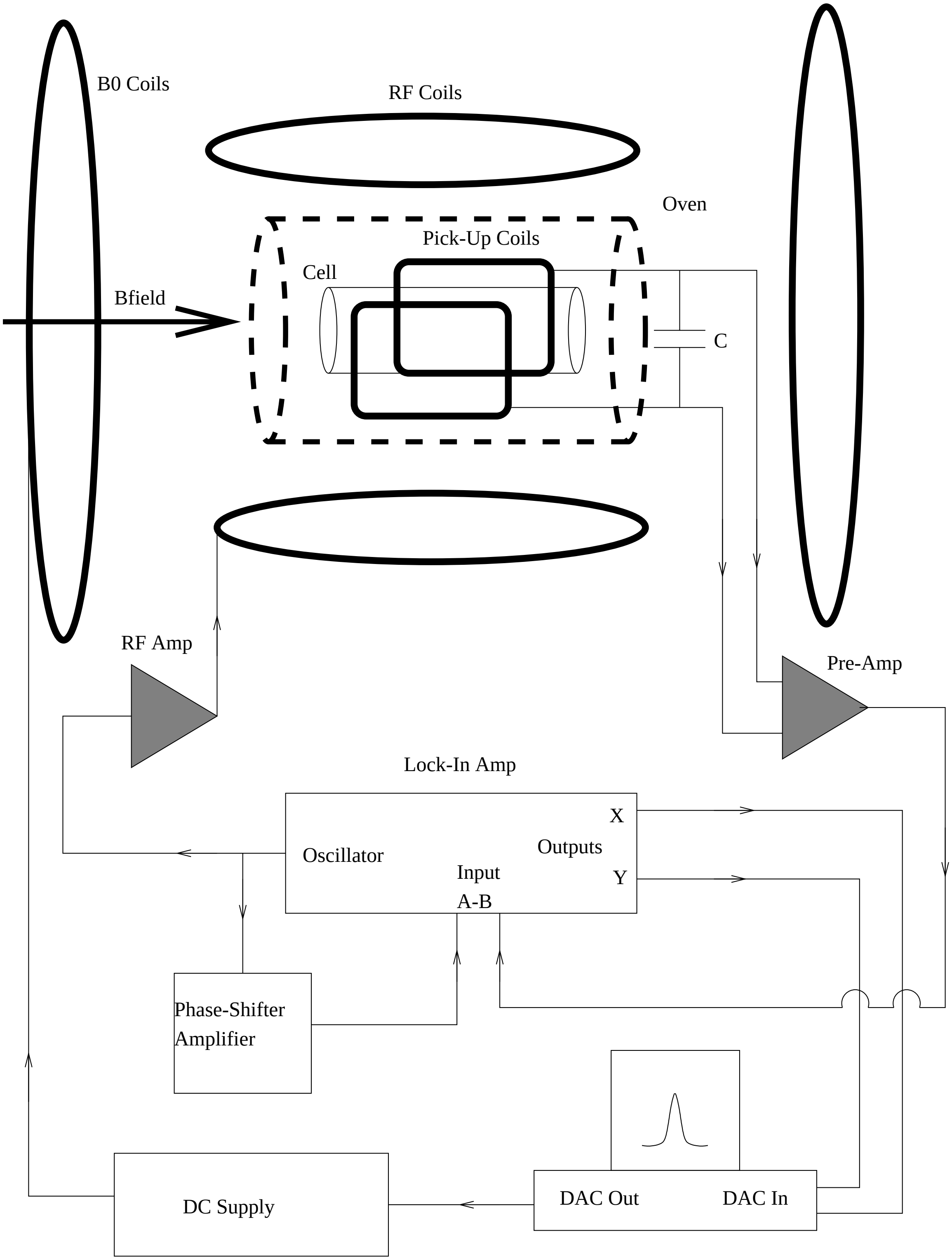

Figure 3-19: Block diagram of the AFP NMR apparatus.

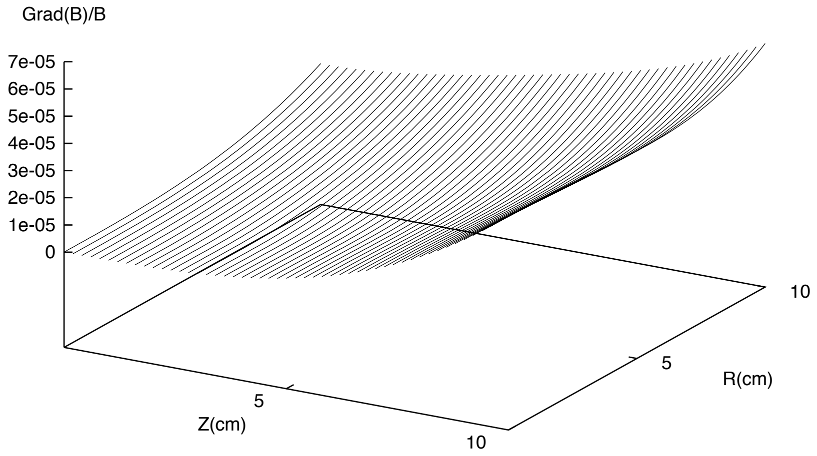

Figure 3-20: $\Delta$B/B ($m^{-1}$) calculations for the 2.02 meter holding field magnet.

To reduce electrical noise, a Sola isolation transformer was used to power all the electronics in the experiments. In order to reduce ground loop problems, the grounds from each piece of equipment were brought to the same point. However, despite these attempts, there was still a great deal of environmental noise in the room making NMR with water difficult. To reduce noise, all breakers were turned off to nonessential instruments and the lights were shut off. Also a shielding cage made from galvanized steel screen (hardware cloth) was built around the large 2 meter Helmholtz coils. The effect of this shield was a reduction in the noise by approximately a factor of 5.

Optical pumping occurred using an Argon Ion/Ti:Sapphire laser system or a fiber coupled laser diode,[65] which is capable of producing 15 W at ~795 nm. The Ti:Sapphire laser system produces about 3 W at 795 nm with a FWHM of about 0.1 nm. The diode laser profile was measured and has a much wider profile (see figure 3-27). The output from the Ti:Sapphire system was linearly polarized. Circularly polarized light was produced using a $\lambda/4$ plate. The output of the diode laser was also linearly polarized, however, mixing of the two spin states in the fiber destroyed the polarization. Circular polarization was then produced using the apparatus shown in Figure 3-28. A converging lens is used to produce a semi–parallel beam coming from the diverging beam out of the fiber. The divergence of the light exiting the fiber produces an approximate 14° cone. Next the light is split into two spin states 90° apart using a polarization beam–splitter cube. One of the beams travels straight through a $\lambda/4$ wave plate, thus converting to circularly polarized light. The other beam is reflected from a mirror and then sent through its own $\lambda/4$wave plate. The two beams are then focused onto the cell.

The ovens used for optical pumping were required to withstand ~180° C, and be both non–magnetic and non–conductive. Such demands limit the choice of material. Depending on the appli-

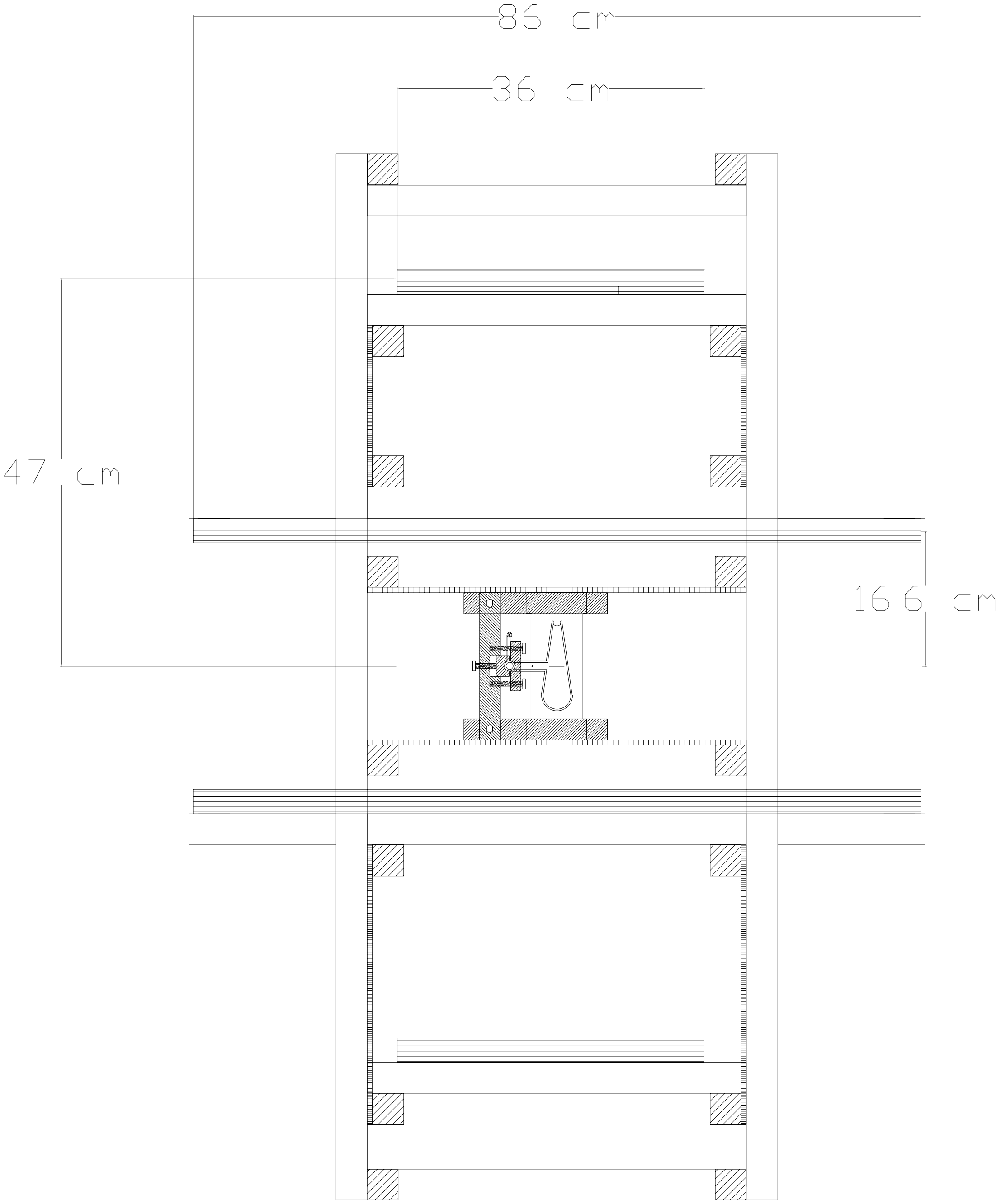

Figure 3-21: 4 coil magnet. The purpose of this arrangement is to produce a uniform field for a give space constraint.

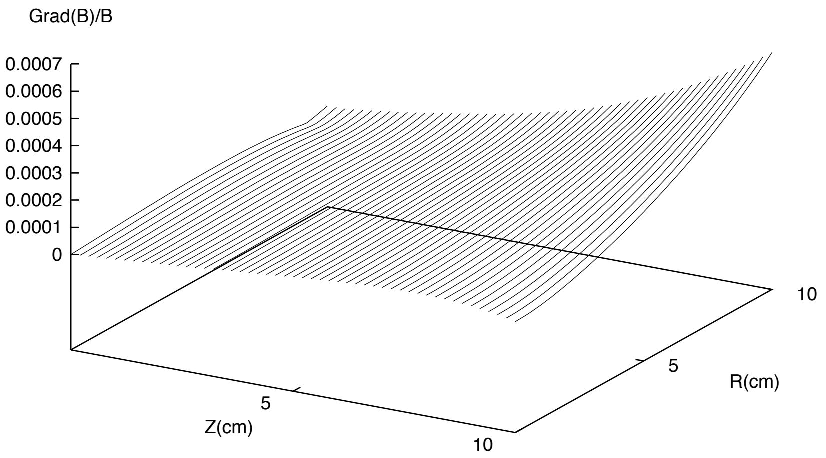

Figure 3-22: ΔB/B ($m^{-1}$) calculations for the 4 coil holding field magnet.

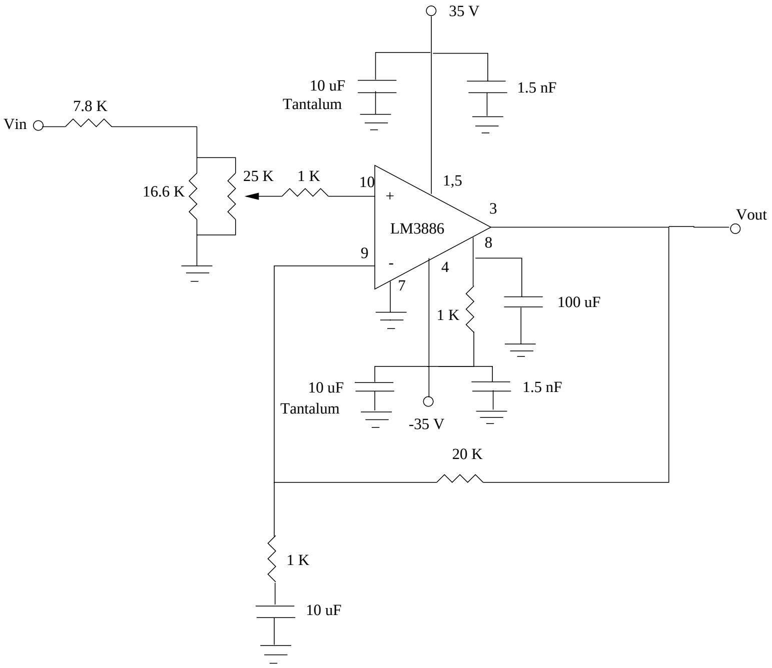

Figure 3-23: The circuit diagram of the RF amplifier used to produce $B_1$.

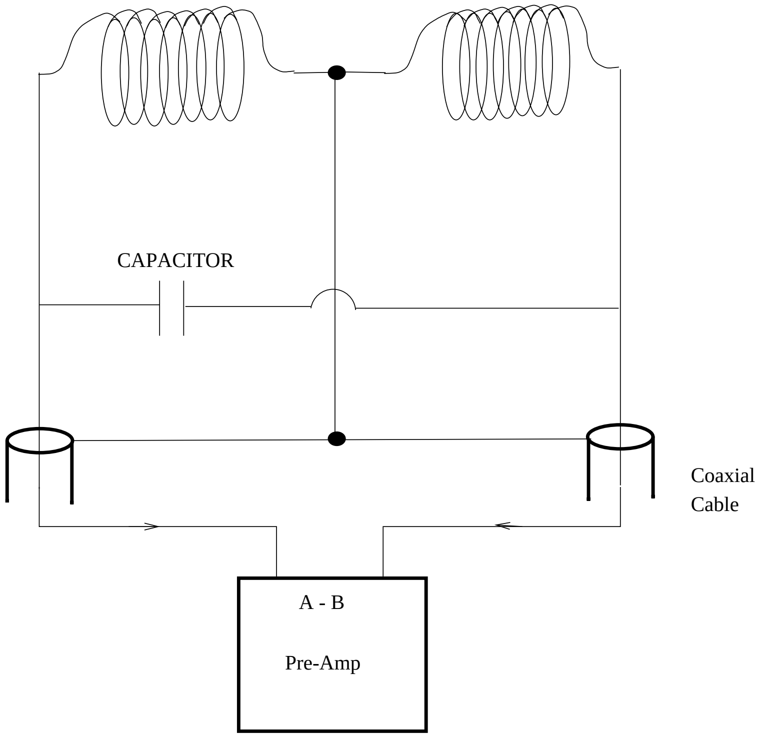

Figure 3-24: A diagram showing the pick–up coil configuration. The capacitor is used to form a tank circuit tuned to approximately 90 kHz.

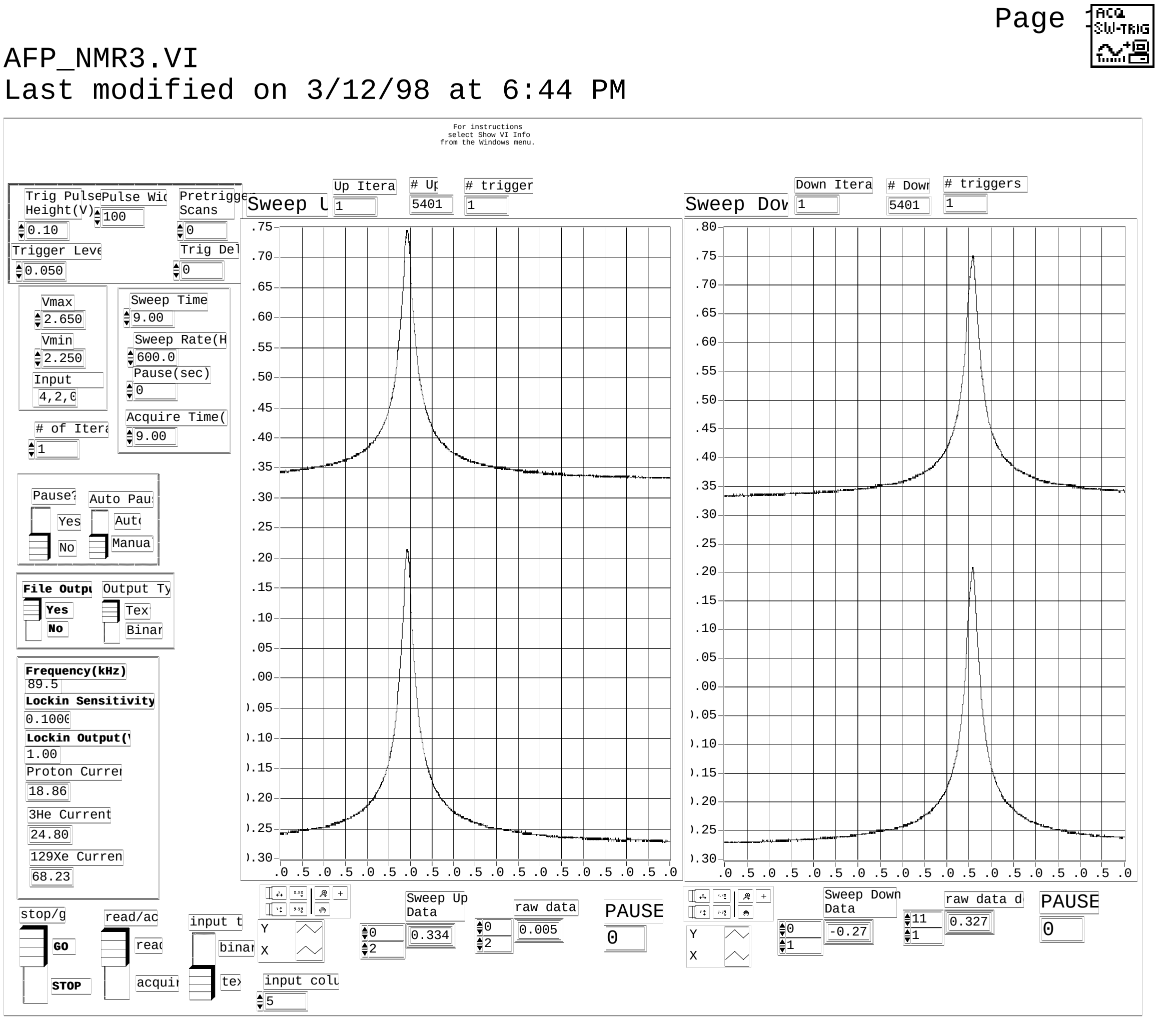

AFP_NMR3.VI
Last modified on 3/12/98 at 6:44 PM

For instructions
select Show VI Info
from the Windows menu.

Trig Pulse Height(V) 0.10
Pulse Wic 100
Pretrigge Scans 0
Trigger Leve 0.050
Trig Del 0
Vmax 2.650
Vmin 2.250
Input 4,2,(
Sweep Time 9.00
Sweep Rate(H 600.0
Pause(sec) 0
Acquire Time( 9.00
# of Itera 1
Pause? Yes No
Auto Pau: Auto Manua
File Outpu Yes No
Output Ty Tex Binar
**Frequency(kHz)** 89.5
**Lockin Sensitivity** 0.1000
**Lockin Output(V** 1.00
Proton Curren 18.86
3He Current 24.80
129Xe Curren 68.23
stop/g GO STOP
read/ac reac acqui
input t binar tex
input colu 5

Sweep U
Up Itera 1
# Up 5401
# trigger 1
Sweep Up Data 0 2 0.334
raw data 0 2 0.005
PAUSE 0

Sweep Dov
Down Itera 1
# Dowr 5401
# triggers 1
Sweep Down Data 0 1 -0.27
raw data d 11 1 0.327
PAUSE 0

Figure 3-25: The LABVIEW based data acquisition display.

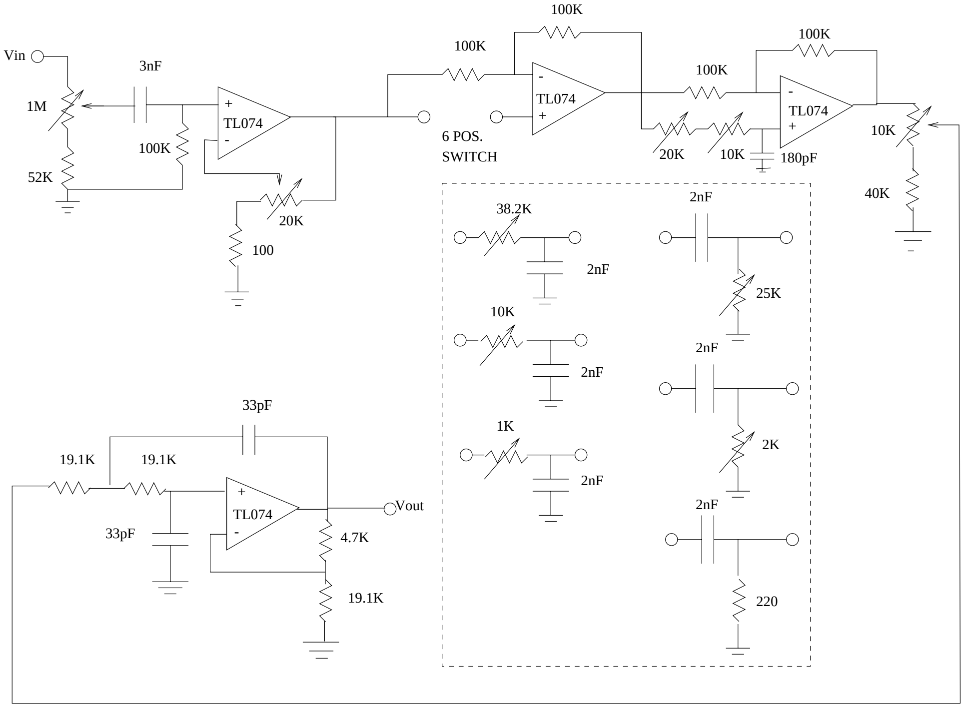

Figure 3-26: Circuit diagram for the phase–shifter amplifier. Resistors are ±1% tolerance. Capacitors are of the ceramic type. All variable resistors are high precision 10–turn Cermet resistors. Each IC power input was filtered using a $22\mu$F tantalum capacitor and 1.5nF ceramic capacitor.

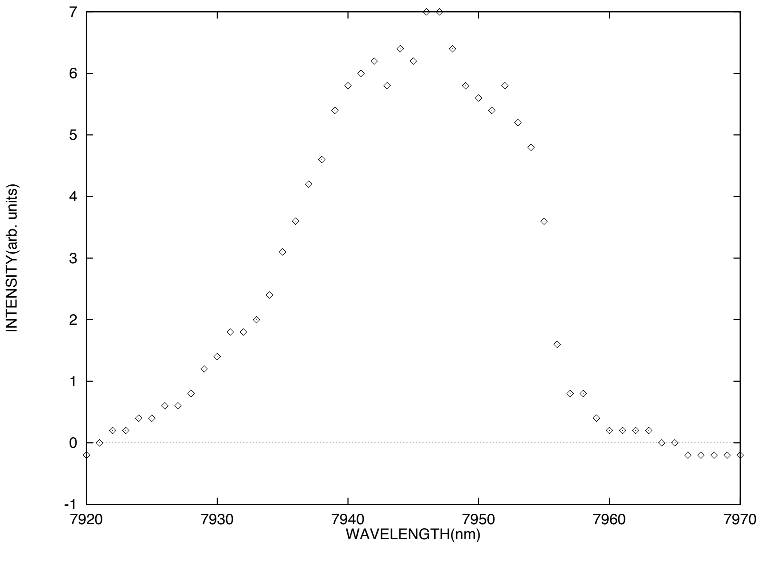

Figure 3-27: The intensity profile from the fiber coupled diode laser.

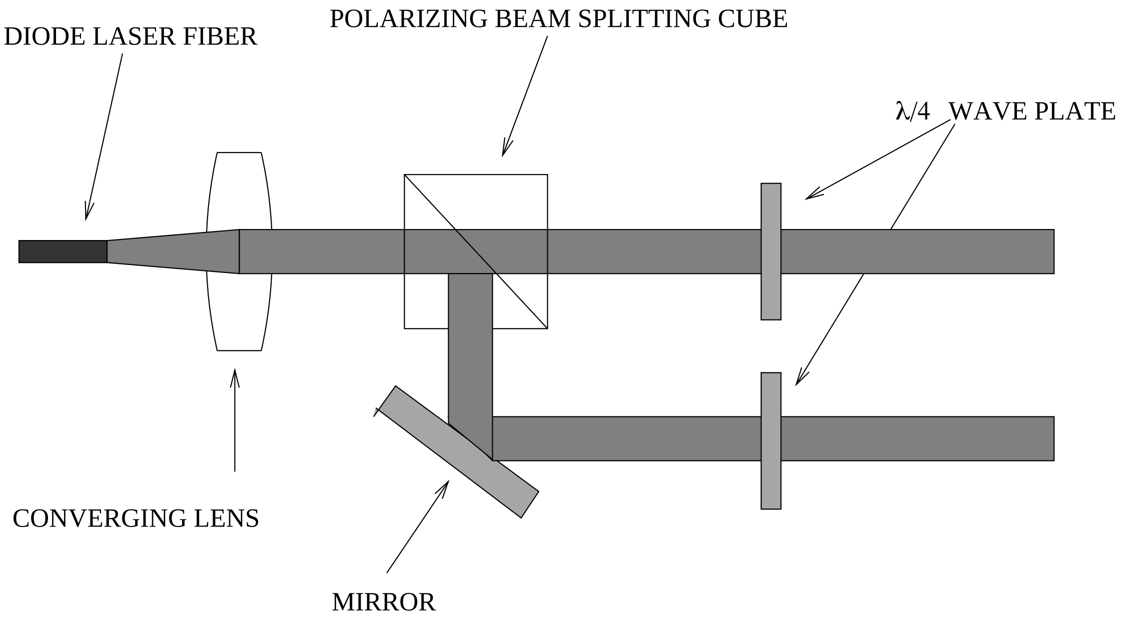

Figure 3-28: The repolarization optics used for the fiber coupled diode laser.

cation, various ovens were used. A cylindrical oven made from glass filled nylon was used for the valved cells in the MRI experiments. A double walled cylindrical glass oven was used for relaxation measurements with smaller cells.

*"I have had a most rare vision."*

— *William Shakespeare*

# Chapter 4

# Magnetic Resonance Imaging

In this chapter an introduction to nuclear magnetic resonance (NMR) and magnetic resonance imaging (MRI) is given. Furthermore, this chapter also introduces magnetic resonance imaging with polarized noble gases. Finally, the first low–field imager/spectrometer and the data that have been acquired will also be described in this chapter.

## 4.1 Basic Principles of NMR

Nuclear magnetic resonance involves the natural resonance phenomena of transitions between specific energy states of nuclear orientation in a magnetic field. Magnetic resonance requires the existence of a magnetic moment and angular momentum. The usefulness of NMR is that it allows for the study of specific spins in a magnetic material. Even in the presence of dominant magnetic material, spins that have a small contribution to the total magnetization can be investigated with NMR. Due to the screening effect of the electrons in chemical compounds, the resonance frequency of a free atom is different from that in bulk material. This effect is called chemical shift. Observing the chemical shift provides information about the chemical composition of the material. NMR also allows for non–invasive studies of subjects and materials. These properties allow for the use of NMR in fields such as physics, chemistry, biology and medicine. This section introduces the basic principles of NMR in preparation for a discussion of magnetic resonance imaging with polarized noble gases. Thorough discussions of NMR can be found in many texts.[39,66–68]

### 4.1.1 Magnetization and Polarization

Individual nucleons have a spin of $\frac{1}{2}$. The spins from individual nucleons couple together in a nucleus with orbital angular momentum to form the total angular momentum of $\hbar$I where I is either integer or half integer. The magnetic moment related to a total angular momentum $\hbar$I is

$$\mu = \frac{ge\hbar I}{2m_p} \tag{4.1}$$

where $g$ is the Landé factor, $e$ is the charge of an electron, $\hbar$ is Planck's constant divided by $2\pi$, and $m_p$ is the mass of the proton. By defining the gyromagnetic ratio

$$\gamma = \frac{ge}{2m_p}$$

the magnetic moment is

$$\mu = \gamma\hbar I.$$

For protons (neutrons) $\gamma = 26.73$ krad/sec–gauss ($\gamma = -18.296$ krad/sec–gauss) and for ${}^3$He $\gamma$ is 20.38 krad/sec–gauss.

If a magnetic moment is placed in a magnetic field the nucleus will be in an energy state of the Hamiltonian $\mathrm{H}=-\vec{\mu}\cdot\mathbf{B}$. If the magnetic field is pointing in the z direction

$$H = -\mu B_0 = -\gamma\hbar \mathrm{B_0 I_z}.$$

The eigenvalues for this Hamiltonian are

$$E = -m\gamma\hbar \mathrm{B_0}$$

where $m$ are substates corresponding to different levels, $m = -I, ..., I-1, I$. The energy difference between two adjacent states is

$$\Delta E = \hbar\gamma \mathrm{B}$$

and the energy absorbed is

$$\Delta E = \hbar\omega.$$

From these relations the transition between two adjacent states occurs when radiation of angular frequency $\omega$ ($=2\pi\nu$) is applied

$$\omega = \gamma \mathrm{B}.$$

When an isotropic non-ferromagnetic sample is placed in a magnetic field, a magnetization $\mathbf{M}$ is created

$$\mathbf{M} = \frac{\chi}{1+\chi}\frac{\mathbf{B}}{\mu_0}$$

where $\chi$ is the magnetic susceptibility and $\mu_0$ is the permeability of free space. For paramagnetic systems $\chi \ll 1$ so

$$\mathbf{M} = \chi\frac{\mathbf{B}}{\mu_0}. \tag{4.2}$$

For a collection of spin $\frac{1}{2}$ particles (eg. protons), each particle has two quantum substates, $m = \frac{1}{2}$ and $m = -\frac{1}{2}$. For thermal populations, statistical mechanics must be used to determine what fraction of the spins are aligned with the magnetic field and what fraction are pointing opposite to the field. Given that $\gamma$ is positive, in which case $\vec{\mu}$ is parallel to $\mathbf{I}$. The fraction of the spins that are pointing parallel(antiparallel) to the magnetic field direction is given by the Maxwell–Boltzmann distribution

$$N_{\uparrow\downarrow} = \frac{e^{\frac{\pm\mu B}{kT}}}{e^{\frac{\mu B}{kT}} + e^{-\frac{\mu B}{kT}}}$$

where ± is used to represent a magnetic moment parallel(+) or antiparallel(−) to the applied field. $T$ is the temperature in Kelvin and $k$ is the Boltzmann constant. The net magnetization is given by

$$\begin{aligned} \mathrm{M} &= N\mu\frac{N_\uparrow - N_\downarrow}{N_\uparrow + N_\downarrow} && (4.3)\\ &= N\mu\frac{e^{\frac{\mu \mathrm{B}}{kT}} - e^{-\frac{\mu \mathrm{B}}{kT}}}{e^{\frac{\mu \mathrm{B}}{kT}} + e^{-\frac{\mu \mathrm{B}}{kT}}} && (4.4)\\ &= N\mu\tanh\left(\frac{\mu \mathrm{B}}{kT}\right) && (4.5)\end{aligned}$$

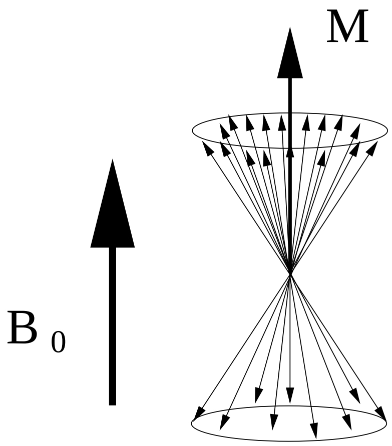

Figure 4-1: A net magnetization due to individual magnetic moments precessing around a magnetic field. Notice that the transverse magnetization is averaged to zero.

$$= N\mu \tanh\left(\frac{\hbar\omega}{2kT}\right) \tag{4.6}$$

where $N = N_\uparrow + N_\downarrow$. The polarization of a sample is defined as

$$P = \frac{N_\uparrow - N_\downarrow}{N_\uparrow + N_\downarrow} \tag{4.7}$$

and the polarization due to a Boltzmann distribution of spins is given by

$$P_{thermal} = \tanh\left(\frac{\hbar\omega}{2kT}\right) \approx \frac{\hbar\omega}{2kT} \tag{4.8}$$

where the thermal subscript is given since the polarization is dependent upon temperature for a given field. Seen from equation (4.8), the polarization increases linearly with frequency and therefore with magnetic field strength. For protons in a 1.5 tesla (15,000 gauss) field at 300 K, the polarization is $5.1\times10^{-4}\%$.

### 4.1.2 Magnetic Moment in a Magnetic Field

The motion of particles with spin I, in a constant magnetic field $\mathbf{B}_0$ and a weak oscillating field $\mathbf{B}_1$ perpendicular to $\mathbf{B}_0$, can be calculated classically. Let J be the magnitude of the angular momentum $\mathbf{J}$, classically given by $J = \hbar I$. An angle $\theta$ is defined as the angle between the z–axis and $\mathbf{J}$ (see Figure 4-2). The constant field $\mathbf{B}_0$ defines the z–axis, and $B_1$ is oscillating in the x–y plane. The constant magnetic field produces a torque on the magnetic moment

$$\mathbf{\Gamma} = \vec{\mu} \times \mathbf{B}_0 = \gamma(\mathbf{J} \times \mathbf{B}_0).$$

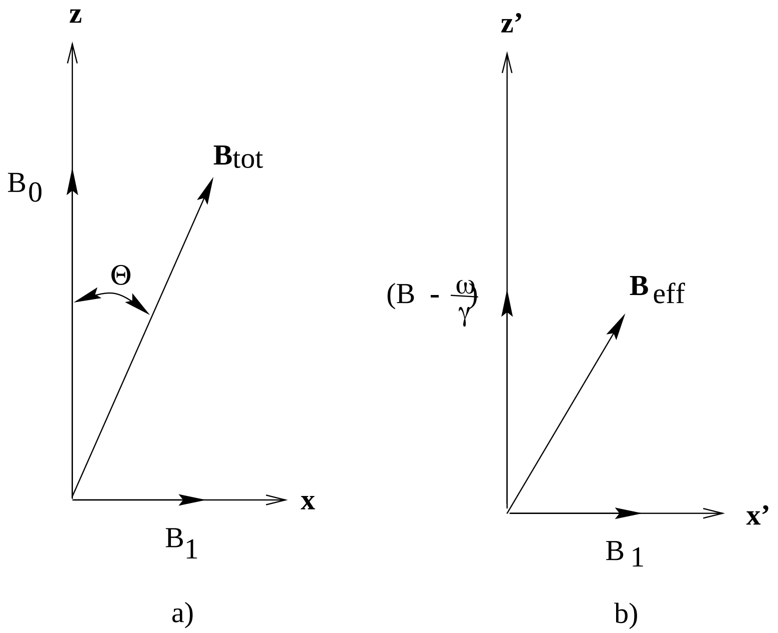

Figure 4-2: The magnetic fields in the a) lab and b) rotating frame.

The torque is equal to the time derivative of the angular momentum so

$$\frac{d\mathbf{J}}{dt} = \gamma(\mathbf{J} \times \mathbf{B_0}) \tag{4.9}$$

To solve this equation it first must be shown that the magnitude of **J** is constant

$$\frac{d(J^2)}{dt} = \frac{d(\mathbf{J} \cdot \mathbf{J})}{dt} = 2\mathbf{J} \cdot \frac{d\mathbf{J}}{dt} = 2\gamma\mathbf{J} \cdot (\mathbf{J} \times \mathbf{B}_0),$$

where it is readily seen that the last expression is identically zero. Using the identities

$$\omega_0 = \frac{d\phi}{dt}$$

$$\frac{d\theta}{dt} = 0$$

and the individual components of equation (4.9)

$$\frac{dJ_x}{dt} = \frac{d}{dt}(J \sin\theta \sin\phi) = \omega_0 J \sin\theta \cos\phi = \gamma J_y B_0$$

$$\frac{dJ_y}{dt} = \frac{d}{dt}(J \sin\theta \cos\phi) = -\omega_0 J \sin\theta \sin\phi = -\gamma J_x B_0$$

$$\frac{dJ_z}{dt} = \frac{d}{dt}(J\cos\theta) = 0$$

it is easily shown that

$$\omega = \gamma B_0$$

and

$$\vec{\omega}_0 = -\frac{|\frac{d\mathbf{J}}{dt}|}{|\mathbf{J}\times\hat{\mathbf{z}}|}\hat{\mathbf{z}},$$

where $\hat{\mathbf{z}}$ is the unit vector in the z direction. From equation (4.9), the magnetic moment is seen to precess about $\mathbf{B}_0$ with an angular frequency of $\omega_0$.

If a weak magnetic field $\mathbf{B}_1(t)$ is rotating in the x–y plane about the z axis with angular frequency $\omega$ given by the expression

$$B_1 = B_1(\hat{\mathbf{x}}\cos\omega t + \hat{\mathbf{y}}\sin\omega t),$$

along with a static magnetic field $\mathbf{B}_0$=B$_0\hat{\mathbf{z}}$, the equation of motion for the spin is

$$\frac{d\mathbf{J}}{dt} = \gamma(\mathbf{J}\times\mathbf{B}) \tag{4.10}$$

where $\mathbf{B} = \mathbf{B}_0 + \mathbf{B}_1$ is the total magnetic field.

The time dependence in equation (4.10) can be eliminated by moving into the rotating frame of $\mathbf{B}_1(t)$. In this new coordinate system, $\mathbf{B}_1(t)$ and $\mathbf{B}_0$ are static. In the lab frame the time derivative of the angular momentum vector is

$$\frac{d\mathbf{J}}{dt} = (\frac{\partial\mathbf{J}}{\partial t} + \vec{\omega}\times\mathbf{J}), \tag{4.11}$$

where $\frac{\partial\mathbf{J}}{\partial t}$ is the time derivative computed in the rotating frame. Substituting (4.11) into (4.10), the equation of motion in the rotating frame is

$$\frac{\partial\mathbf{J}}{\partial t} = \gamma\left[\mathbf{J}\times(\mathbf{B_0} + \mathbf{B_1} + \frac{\vec{\omega}}{\gamma})\right]. \tag{4.12}$$

Rewriting equation (4.12) in the form

$$\frac{\partial\mathbf{J}}{\partial t} = \gamma\left[\mathbf{J}\times(\mathbf{B_0} - \frac{\omega}{\gamma})\hat{\mathbf{k}}' + \mathbf{B_1}\hat{\mathbf{x}}'\right] \tag{4.13}$$

the spin vector is seen to precess about an effective magnetic field $\mathbf{B}_{eff} = (B_0 - \frac{\omega}{\gamma})\hat{\mathbf{k}}' + B_1\hat{\mathbf{x}}'$. At the resonant condition $\omega_0 = \gamma B_0$, the spin is precessing about the $\hat{\mathbf{x}}'$ axis with a frequency $\omega_1 = \gamma B_1$.

There are two general types of methods in NMR, cw (continuous wave) and the pulsed methods. The cw method utilizes an RF field that is applied continuously. Resonance is typically achieved by varying the frequency through the resonant condition. The RF pulse method cycles on and off the RF utilizing various pulse sequences. If an RF pulse is turned on for a duration $\tau$, the magnetization will rotate about $\mathbf{B}_1$ through an angle $\theta = \gamma B_1\tau$. If the $\theta$ is 90° or 180° the pulse is referred to as a 90° or 180° pulse. Such pulses are commonly used in experimental pulsed NMR.

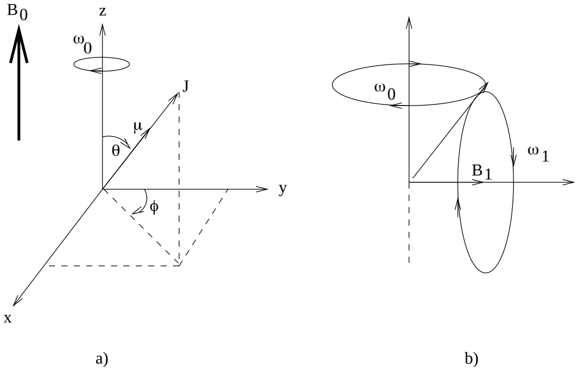

Figure 4-3: Precession of a spin **J** in a magnetic field $\mathrm{B}_0$ at a frequency $\omega_0 = \gamma \mathrm{B}_0$ a). Additionally, when a small rotating magnetic field $\mathrm{B}_1$ is applied about the z–direction, the spin will precesses about $\mathrm{B}_1$ with a frequency $\omega_1 = \gamma \mathrm{B}_1$.

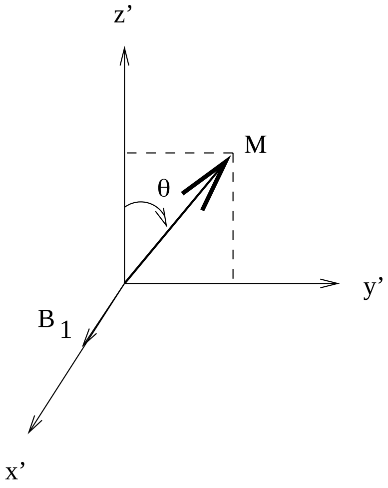

Figure 4-4: Diagram describing the rotation angle $\theta = \gamma\omega_1\tau$which a magnetization vector rotates through when a resonant RF pulse of duration $\tau$ is applied.

### 4.1.3 Spin Relaxation

The application of an RF excitation pulse applied to a system in thermal equilibrium will lift the system to the excited state. Once in the excited state, the system will return to thermal equilibrium with a time constant $T_1$. The energy that was absorbed to excite the nuclei is then transferred to its surroundings, the lattice. This process is referred to as spin-lattice relaxation or longitudinal relaxation. In liquids and gases, the RF fields are moving magnetic nuclei that produce field fluctuations at the resonance condition $\omega_0 = \gamma B_0$. The rate at which nuclei relax is dependent on the motion of the molecule containing the nuclei. For instance, a proton in water may rotate faster than protons in tissue; This is because the protons in tissue may have a stronger rotational component at the resonant condition than do the protons in water. Therefore, the $T_1$ for protons in tissue would be shorter than those in water. One can can easily see that the $T_1$ is dependent upon the magnetic field strength. Typically, the $T_1$ for protons in water is approximately 3 seconds, whereas protons in biologic tissue is typically several hundred milliseconds at typical field strengths (1.5 T). By changing the magnetic field strength, the resonant condition may be closer to the motional frequency of protons in water, causing $T_1$ to shorten and increasing the $T_1$ in tissue.

The change in the magnetization along the direction of the magnetic field as it relaxes to thermal equilibrium is governed by the equation

$$\frac{dM_z}{dt} = \frac{-(M_z - M_0)}{T_1} \tag{4.14}$$

where $M_z$ is the longitudinal component of the magnetization, and $M_0$ is the longitudinal component at thermal equilibrium. Since $T_1$ is the time constant describing the relaxation of the longitudinal component of magnetization, it is referred to as the longitudinal relaxation time.

If a 90° pulse has rotated the magnetization into the x–y plane, the magnetization will precess about $\mathbf{B}_0$. As the magnetization vector rotates about the z–direction its magnitude decreases. This mode of relaxation is referred to as spin–spin, or transverse relaxation, and is given by the time constant $T_2$. Transverse relaxation is different from longitudinal relaxation in that it is not due to energy exchange to the lattice. Rather, unlike longitudinal relaxation, transverse relaxation is due to loss of phase coherence between spins. If the sample of interest were in a uniform field, all the spins would precess at the same frequency and in phase. However, magnetic field inhomogeneities and nuclear dipole fields within the bulk material will cause nuclei at different locations to precess at different frequencies. As the nuclei precess, their relative phases change, causing a loss in transverse magnetization. Since transverse relaxation is affected by dephasing interactions $T_2 \leq T_1$. $T_2$ is primarily due to local field imperfections and, thus, is less susceptible to magnetic field strengths than $T_1$. Since they produce larger static field components, slowly rotating molecules are more efficient at causing efficient $T_2$ relaxation; this is readily observed in solids where $T_2$ is very short. The transverse magnetization is governed by the equation

$$\frac{dM_{x,y}}{dt} = \frac{M_{x,y}}{T_2} \tag{4.15}$$

where $M_{x,y}$ is the component of the magnetization in the x,y direction.

By combining equations (4.14), (4.15), (4.13) and the relationship $\mathbf{M} \propto \Sigma \mathbf{J}_i$ the well known Bloch equations[39] are reproduced in the rotating frame:

$$\frac{dM_x}{dt} = \gamma M_y (B_0 - \omega/\gamma) - \frac{M_x}{T_2} \tag{4.16}$$

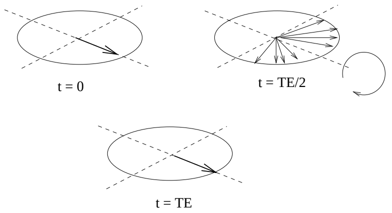

Figure 4-5: Formation of a spin echo. At time $t = 0$ the net magnetization vector is in the x-y plane after having received a 90 degree pulse. As time progresses, the spins begin to dephase due to magnetic field inhomogeneities. At time $t =$ TE/2, a 180 degree pulse is given. At time $t =$ TE the spins have rephased and an echo is observed.

$$\frac{dM_y}{dt} = \gamma M_z B_1 - \gamma M_x (B_0 - \omega/\gamma) - \frac{M_y}{T_2} \tag{4.17}$$

$$\frac{dM_z}{dt} = \gamma M_y B_1 - \frac{M_z - M_0}{T_1}. \tag{4.18}$$

Transverse spin relaxation due to magnetic field imperfections can be can be recovered using spin echos. In applying a 90° pulse, the longitudinal magnetization is rotated into the transverse plane where the spins precess. As time increases, spins in a larger field will precess faster than those in a smaller field causing them to dephase. In figure 4-5 the faster spins are ahead of the slower spins. If a 180° pulse is applied a time TE/2 after the 90° pulse, the slower spins exchange place with the faster spins. After an additional time TE/2, the faster spins will catch up to the slower spins producing a spin echo. An example of a spin echo is shown in figure 4-6. The amplitude of the echo is smaller than that of the FID since the magnetization loss due to local dipolar fields is not recovered with a spin echo as in the case due to losses associated with magnetic field imperfections. When a refocusing 180° pulse is given, both the spins and the dipolar fields are reversed. Thus the effect due to dipolar fields is unchanged using a spin echo. The use of a spin-echo technique allows for the separation of dipolar and magnet inhomogeneity relaxation modes. Therefore, it is useful to define the transverse relaxation time constant due to non-reversible dephasing processes, such as dipolar fields, and diffusion as $T_2$, and the time constant related to the decay of the FID as $T_2^*$

$$\frac{1}{T_2^*} = \frac{1}{T_2} + \frac{1}{T_{2inh}} + \frac{1}{T_{2sus}} + \frac{1}{T_{2other}} \tag{4.19}$$

where $T_{2inh}$, $T_{2sus}$, and $T_{2other}$ are the transverse relaxation time constants due to inhomogeneities in the magnetic field, local differences in susceptibility and magnetization, and other processes. Additional 180° pulses will produce similar echos with decreasing amplitudes that fall off with the time constant $T_2$.

### 4.1.4 Signal Detection

Detection of precessing spins is accomplished by placing a detection coil perpendicular to $B_0$. A net magnetization in the transverse plane perpendicular to $B_0$ induces an emf in the coil. As the magnetization precesses about the magnetic field, the induced emf is proportional to $\mu$NP, where $\mu$ is the magnetic moment of the nuclei under investigation, N is the number of nuclei, and $P$ is the

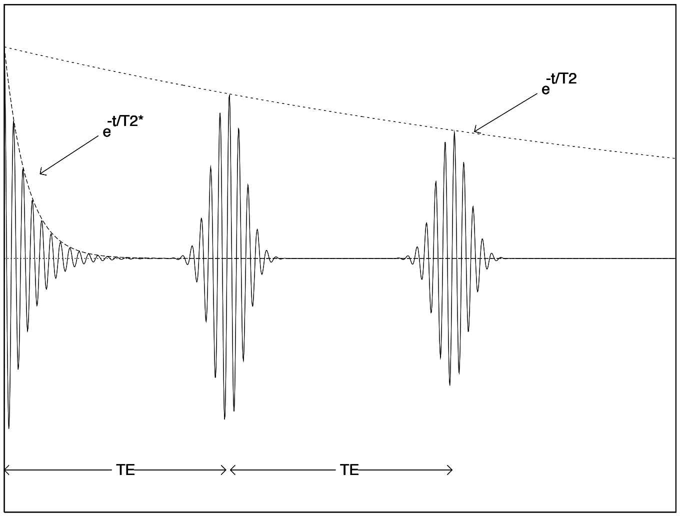

Figure 4-6: Signal observed during a spin echo. At $t = 0$ a free induction decay is observed with a decay time constant of $T_2^*$. At time TE the center of the echo occurs. The echo amplitude decreases exponentially with a time constant $T_2$.

polarization. The induced signal depends to a great extent on the construction of the coil and on the filling factor; the filling factor is a quantity that relates to the degree of which the sample is coupled to the detection coil. A simple definition of the filling factor that is sometimes used is given by

$$F = \frac{V_s}{V_c}$$

where $V_s$ is the volume of the sample, and $V_c$ is the coil detection volume. Once detected, the signal is mixed with an oscillator at frequency $\omega_r$; this method is known as heterodyne detection. The mixed output depends on the relative phase between the detected and reference signal. This allows for quadrature detection by implementing two reference signals that are 90° out of phase. The output from the receiver is then of the form

$$S(t) = S_0 e^{i\phi} e^{i\Delta\omega} e^{-t/T_2}$$

where $\phi$ is the absolute receiver phase, and $\Delta\omega = \omega_0$ - $\omega_r$ is the difference between the reference frequency and the detected frequency.

## 4.2 Magnetic Resonance Imaging

Nuclear magnetic resonance experiments were first reported independently in 1946 by Purcell *et al.*[69] at MIT, and by Bloch *et al.*[70] at Stanford. However, it was not until 1973 that the first two dimensional image of a live animal was reported by Lauterbur.[71] Mansfield and Grannell[72] demonstrated the relationship between the NMR signal and the spin density using Fourier techniques during the same year. In 1977 the first images were observed[73] using a whole-body imager. Shortly afterwards, in the early 1980's, manufacturers obtained FDA approval for their magnetic resonance imaging systems. Today magnetic resonance imaging (MRI) is routinely used in experiments with resolutions of less than 0.1 mm for biological, mineral, and synthetic material research.

### 4.2.1 Basic Principles

Since the frequency of precession for a moment is dependent upon the magnetic field strength, it is easy to impose a spatial dependence to the frequency by using a spatially varying magnetic field. Using linearly varying magnetic fields, the precession frequency will be a linear function of position. By defining the three dimensional gradient **G** as

$$\mathbf{G} = (G_x, G_y, G_z) = \left(\frac{\partial \mathrm{B_z}}{\partial x}, \frac{\partial \mathrm{B_z}}{\partial y}, \frac{\partial \mathrm{B_z}}{\partial z}\right) \tag{4.20}$$

the magnetic field at position **r** can be written as

$$\mathrm{B}(\mathbf{r}) = \mathrm{B}_0 + \mathbf{G} \cdot \mathbf{r} \tag{4.21}$$

where $\mathrm{B}_0$ is the static magnetic field applied in the z direction. The position dependent angular frequency becomes

$$\omega(\mathbf{r}) = \omega_0 + \gamma \mathbf{G} \cdot \mathbf{r}. \tag{4.22}$$

Fourier transforms are essential to NMR and MRI to relate the data to frequency or coordinate space. With NMR spectroscopy, data are acquired in time space ($t$–space) and then transformed into frequency space ($\omega$–space) as spectra using a Fourier transformation. In MRI, data is acquire in spatial frequency space ($k$–space) and then transformed into coordinate space. For a time-dependent signal $S(t)$ its Fourier transform is

$$S(\omega) = \int_{-\infty}^{\infty} S(t) e^{-i\omega t} dt \tag{4.23}$$

where the inverse transform is

$$S(t) = \frac{1}{2\pi} \int_{-\infty}^{\infty} S(\omega) e^{i\omega t} d\omega. \tag{4.24}$$

Similarly, for a spatially dependent function $S(x)$ its Fourier transform is

$$S(k) = \int_{-\infty}^{\infty} S(x) e^{-i2\pi kx} dx \tag{4.25}$$

and the inverse transform is

$$S(x) = \int_{-\infty}^{\infty} S(k) e^{i2\pi kx} dk. \tag{4.26}$$

The form of the transform can easily be extended to multidimensions. The Fourier transform of a 2D function $S(x, y)$ is

$$S(k_x, k_y) = \int_{-\infty}^{\infty} S(x, y) e^{-i2\pi(k_x x + k_y y)} dx dy \tag{4.27}$$

In MRI, images are acquired in $k$–space and then transformed into coordinate space.

If sample of spins exist at position **r** with a small element of volume $dV$, and a total number of spins $\rho(\mathbf{r})dV$, the signal from this element of volume is

$$dS(\mathbf{G}, t) \quad \propto \quad \rho(\mathbf{r}) dV e^{i\omega(\mathbf{r})t} \tag{4.28}$$

$$\propto \;\; \rho(\mathbf{r}) dV e^{i\gamma(B_0+\mathbf{G}\cdot\mathbf{r})t}. \tag{4.29}$$

If signals are mixed with another at frequency $\gamma \mathrm{B}_0$, the observed signal will oscillate with a frequency $\gamma\mathbf{G}\cdot\mathbf{r}$. This process is called heterodyne mixing. The detected signal is

$$S(t) = \int \rho(\mathbf{r}) e^{i\gamma\mathbf{G}\cdot\mathbf{r}} d^3r \tag{4.30}$$

where the constant of proportionality has been ignored. By defining the $k$–vector as

$$\mathbf{k} = \frac{\gamma\mathbf{G}t}{2\pi} \tag{4.31}$$

Equation (4.30) can be rewritten as

$$S(\mathbf{k}) = \int \rho(\mathbf{r}) e^{-i2\pi\mathbf{k}\cdot\mathbf{r}} d^3r \tag{4.32}$$

which is in the form of a Fourier transform. The inverse of equation (4.32) is

$$\rho(\mathbf{r}) = \int S(\mathbf{k}) e^{i2\pi\mathbf{k}\cdot\mathbf{r}} d^3k \tag{4.33}$$

The $k$–space vector has units of inverse space. In order to move through $k$–space, either the time or the magnitude of the gradient must be varied. If the signal amplitude is measured while traversing through $k$–space, equation (4.33) can be used to determine the spin density as a function of $\mathbf{r}$. This is the basic principle of Fourier MRI.

Magnetic resonance data is acquired by sampling the signal at discrete intervals $\Delta t$ in time, or $\Delta k$ in $k$–space. If there are N discrete sampling points, then the total sampling time is $T$ and the maximum $k$–vector is $N\Delta k$. The discrete Fourier transform of a function $f(m\Delta t)$ sampled at intervals $\Delta t$ is

$$F(\frac{n}{N\Delta t}) = \sum_{m=0}^{N-1} f(m\Delta t) e^{-i2\pi nm/N} \tag{4.34}$$

and

$$f(m\Delta t) = \sum_{n=0}^{N-1} G\left(\frac{n}{N\Delta t}\right) e^{i2\pi nm/N}. \tag{4.35}$$

Notice that $F(\frac{n}{N\Delta t})$ is periodic: $F(\frac{N-n}{N\Delta t}) = F(\frac{-n}{N\Delta t})$. The limits of the summation can be changed to $-\frac{1}{2}N$,....,$\frac{1}{2}N-1$. The discretely sampled spin density is

$$\rho\left(\frac{n_x}{N\Delta t}, \frac{n_y}{N\Delta t}\right) = \sum_{l=-\frac{1}{2}N}^{\frac{1}{2}N-1} \sum_{m=-\frac{1}{2}N}^{\frac{1}{2}N-1} S(lT, m\Delta t) e^{\frac{-i2\pi}{N}(ln_x+mn_y)} \tag{4.36}$$

where $n_x$, $n_y = -\frac{1}{2}N$,....,$\frac{1}{2}N-1$.

Earlier it was illustrated that a position dependence can be imposed on frequency using a field gradient. For example, if a gradient is applied along the x-direction, the precession frequency will have an x–dependence $\omega_x = \gamma G_x x$. In addition, spatially dependent phase differences can be induced on the spins. If the field gradient $G_y$ along the y-direction is applied, the spins located at higher fields due to the gradient will precess faster than those at lower fields. If the gradient is turned

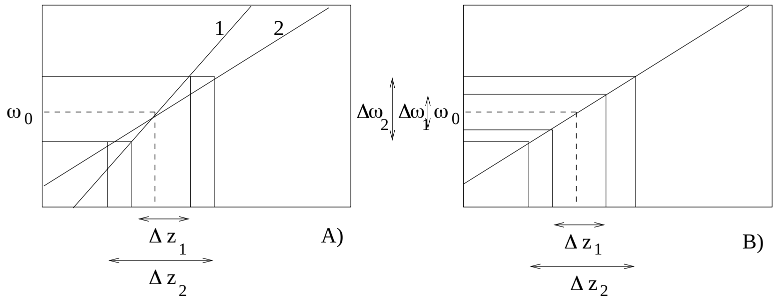

Figure 4-7: Figure A) shows how the slice thickness varies with different gradient strengths. Gradient 1 is greater than gradient 2 and the corresponding slice thickness $\Delta z_1$ is small than $\Delta z_2$. In figure B) the smaller bandwidth $\Delta\omega_1$ produces a thinner slice thickness $\Delta z_1$ than the larger bandwidth $\Delta\omega_2$.

on only for a time $t_y$, the spins are once again precessing at the same frequency. However, in the interim, an induced phase difference $\phi = \gamma G_y y t_y$ appears. This process is known as phase encoding.

In magnetic resonance imaging, it is often necessary to excite a slice within the sample. This is accomplished by utilizing a magnetic field gradient, and an RF pulse with a bandwidth to select only a given slice of thickness $\delta$z. This method is called selective excitation and is shown schematically in figure 4-7. The ability to selectively excite portions of a sample is crucial to MRI. From figure 4-7 the thickness of the selected slice is seen to decrease when the gradient strength increases. Additionally, for a given gradient strength, the slice thickness decreases with the RF frequency bandwidth $\Delta\omega$. The frequency bandwidth is inversely proportional to the time the pulse is turned on. Therefore, short pulses have a wide frequency bandwidth; a 1 ms pulse will have a 1 kHz bandwidth. For a given flip angle $\theta = \gamma \mathrm{B}_1 T$, the product $\mathrm{B}_1 T$ must be held constant. Therefore, to increase the slice thickness, $\Delta z$ $\mathrm{B}_1$ must be increased, while, in order to increase bandwidth, $T$ must be decreased. Large amplitude short pulses are referred to as hard pulses. Hard pulses are used in NMR spectroscopy to excite spins using an appropriate bandwidth to include frequencies shifted by field inhomogeneities and chemical shifts.

Soft pulses are those that selectively excite a layer of thickness $\Delta z$ within the sample. A simple way to make a soft pulse is to both reduce the RF amplitude $\mathrm{B}_1$ and lengthen the pulse duration T. Longer pulses will reduce the frequency bandwidth and as a result $\Delta z$. The Fourier transform of an RF pulse of width $T$ is a sinc function that has its first zero crossings at ±1/T. Since it has side lobes so that excitation occurs outside the bandwidth 1/T, this soft pulse is not optimum. A more efficient soft pulse is created by an RF pulse that has the form

$$B_1(t) = B_1^0 e^{i\omega t} sinc(\frac{t}{T}). \tag{4.37}$$

The Fourier transform to frequency space is a rectangular frequency spectrum with a bandwidth of 1/T. Since the RF pulse is finite in time, $\mathrm{B}_1$ is actually a truncated sinc function which causes the frequency distribution to be in the shape of a deformed rectangle. Ringing at the edges occurs due to Gibbs' phenomenon. Figures 4-8 and 4-9 are hard and soft pulses with their respective Fourier transforms.

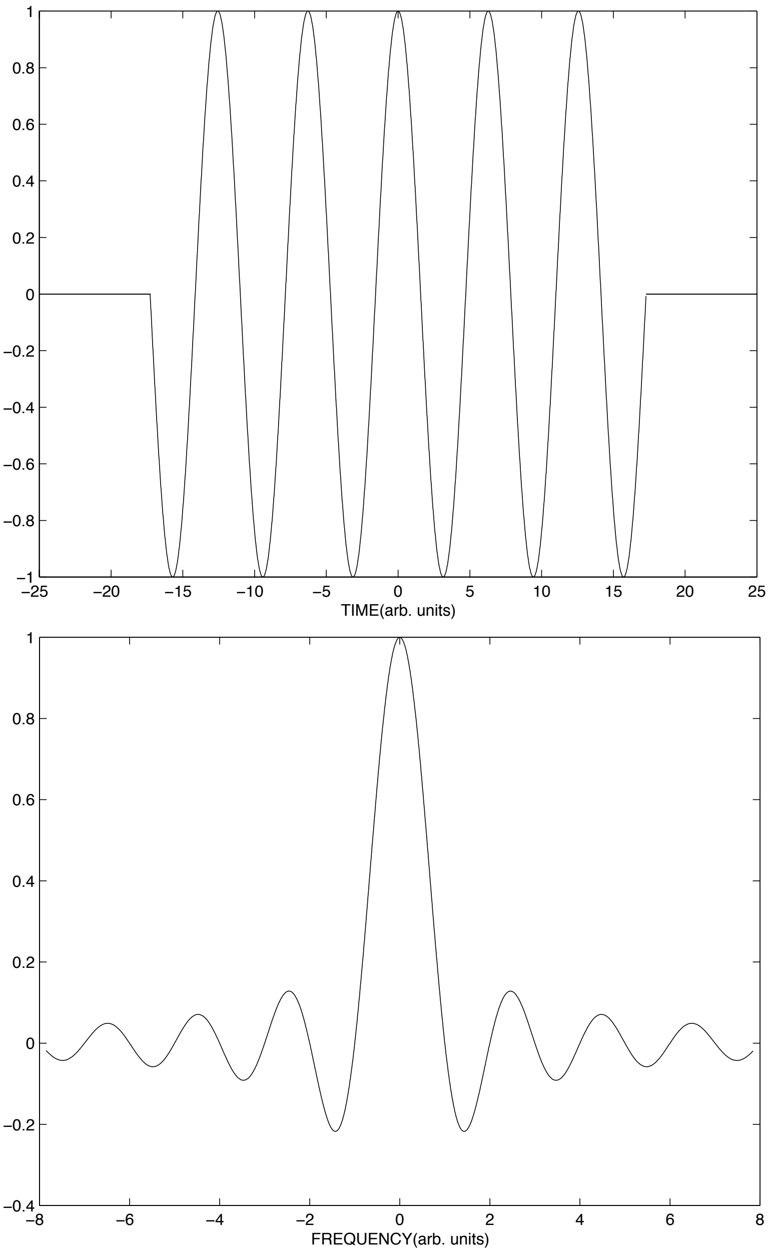

Figure 4-8: A hardpulse and its Fourier transform.

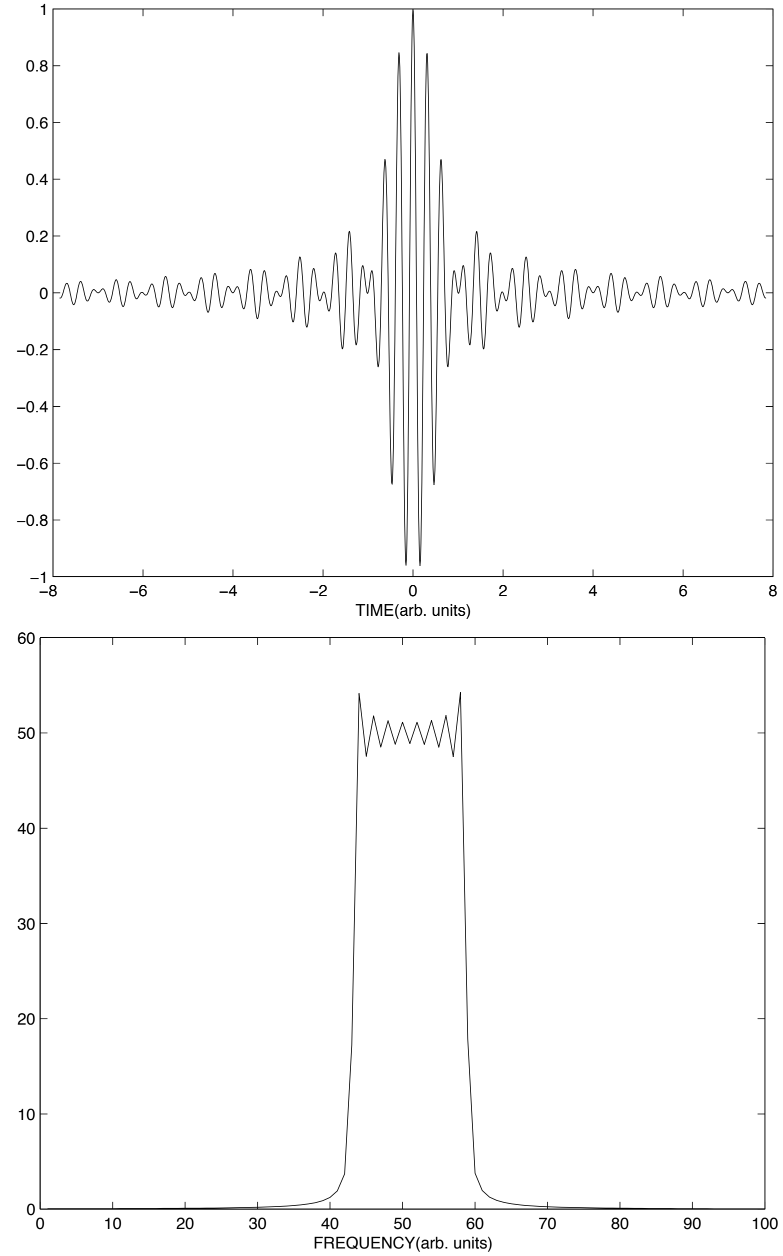

Figure 4-9: A soft pulse and its Fourier transform.

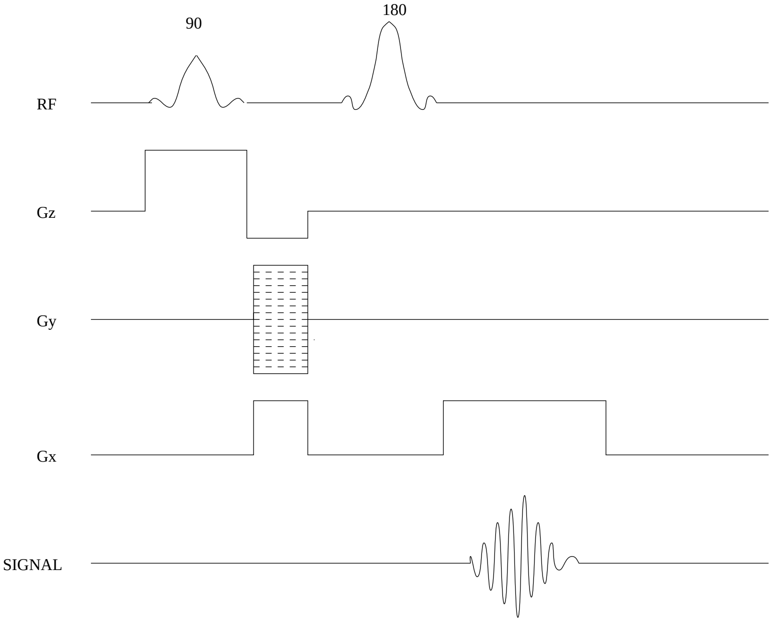

Figure 4-10: Spin echo sequence pulse timing diagram.

### 4.2.2 Pulse Sequences

Many pulse sequences exist that were developed for specific experiments. Several of these sequences are built on the foundations of spin and gradient echo sequences. In the section on relaxation, the formation of a spin echo was discussed and illustrated in figure 4-5, which shows the magnetization as a function of time. Figure 4-10 shows the timing diagram for a spin echo pulse sequence. The first step in the spin echo sequence is the application of a 90° RF pulse, which rotates the magnetization into the transverse plane. The gradient $G_z$ is then used to excite a slice of thickness $2\pi\Delta\nu/\ (\gamma G_z)$, where $\Delta\nu$ is the bandwidth of the RF pulse. After the 90° pulse has been applied, the z–gradient is inverted to rephase the spins. At the same time a variable phase gradient $G_y$ is applied. In addition, the read gradient $G_x$ is used to insure that the spins are dephased, thus ensuring that they can be rephased at a later time to produce the echo. Following this, a 180° pulse is then used to flip the spins by 180°, causing the spins to rephase at time TE. Finally, the read gradient is applied and the echo is formed.

Figure 4-11 shows the timing diagram for a gradient echo pulse sequence. Similar to the spin echo sequence, the gradient echo sequence uses a slice selection gradient $G_z$ and a 90° RF pulse to rotate the spins into the transverse plane. Next, both a phase encode gradient and a dephasing read gradient are applied. The final step entails a negative read gradient to rephase the spins and to frequency encode the spins for acquisition.

### 4.2.3 Signal-to-Noise

The measurement of a signal includes both the true signal and a background of noise which is superimposed on it. This noise may be due to external noise sources, such as motors and switching devices, amplifier noise, and noise due to electronic components. Since other sources of noise can be

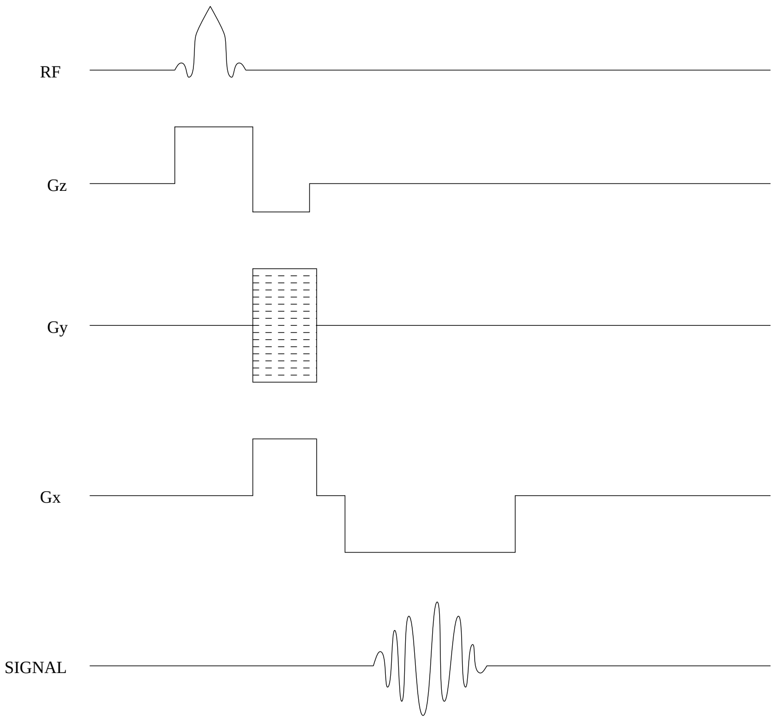

Figure 4-11: Gradient echo sequence pulse timing diagram.

eliminated, it is this latter source of noise that is discussed here. Electrons in a circuit element have a random motion due to their thermal energy. The equipartition theorem of statistical mechanics maintains that, for a system at equilibrium, there is an average energy of $kT/2$ for each degree of freedom. For example, a free electron will have three degrees of freedom and, thus, will have an average energy of $3kT/2$. Since the motion of the electrons are random, there may be more electrons at one end of a resistor than at the other, resulting in a fluctuating potential difference. The root mean square (RMS) potential difference is constant in amplitude as a function of frequency, i.e., 'white' noise. The RMS amplitude of this noise is called "Johnson noise" and is given by

$$\sqrt{< S_{noise}^2 >} = \sqrt{4kTR\Delta\nu} \tag{4.38}$$

where $k$ is Boltzmann's constant, $T$ is the temperature, $R$ is the resistance, and $\Delta\nu$ is the frequency bandwidth. Since noise is a random process, its average is zero, making the RMS amplitude a more useful quantity. When analyzing noise contributions in a circuit, it is the individual powers and not the voltages that add. Therefore, the total noise voltage is given by the square root of the sum of the squares of the individual noise voltages. By repeating a measurement N times, the square of the noise increase N fold and the RMS noise increase as the $\sqrt{N}$. The average RMS noise thus decrease by $1/\sqrt{N}$. Application of this technique is called signal averaging.

The magnitude of the noise does not provide a great deal of information. A more useful quantity is the signal-to-noise ratio ($SNR$). For a non-changing signal between measurements, the signal to noise ratio will increase as the square root of the number of measurements. From the principle of reciprocity,[75] the induced EMF generated by a magnetic moment $\mathbf{m}$ is given as

$$S(t) = -\frac{\partial}{\partial t}\mathbf{m} \cdot \mathbf{B}^{i} \tag{4.39}$$

where $\mathbf{B}_i$ is the magnetic field per unit current induced at the source location by a unit current in the detection coil. For a sample containing magnetic moment density $\mathbf{M}$, the EMF is written as

$$S(t) = -\frac{\partial}{\partial t}\int_{sample} \mathbf{B}^{1} \cdot \mathbf{M}dV \tag{4.40}$$

where the integration is over the sample volume. Assuming that $\mathbf{B}^1$ is homogeneous over the sample volume, the induced signal is given as

$$S(t) \propto \mathrm{B}^{1}\omega\mathrm{M}_{\mathrm{xy}} \tag{4.41}$$

where a 90° pulse has been applied to produce a transverse magnetization $\mathrm{M}_{xy}$. For thermally polarized samples, the signal is

$$S(t) \propto \mathrm{B}^{1}\omega\mathrm{P} \tag{4.42}$$

where $P$ is the polarization (see equation (4.7)) and the signal-to-noise is

$$SNR \propto \frac{\mathrm{B}^{1}\omega\mathrm{P}}{\sqrt{4kTR\Delta\nu}}. \tag{4.43}$$

For thermal polarization, $P$ changes linearly with B (or $\omega$, see equation (4.8)), and for polarized samples $P$ is independent of B. It would appear from equation (4.43) that the signal–to–noise ration would increase as $\omega^2$ for thermal polarization. However, because the resistance $R$ has a frequency dependence, the signal–to–noise does not change linearly with $\omega^2$. The resistance can be broken up into two components, $R = R_c(\omega) + R_s(\omega)$, where the first term is the resistance due to the coil and the second term is the contribution from the sample. For frequencies above 1 MHz, the magnetic field in a conductor is restricted to a region near the surface of thickness $\delta$, known as the skin depth[74]

$$\delta = \sqrt{\frac{2\rho}{\mu\omega}}$$

where $\mu$ is the permeability of the conductor. The resistance of a conducting wire of length l, cross sectional area A, and resistivity $\rho$ is R=$\rho$l/A. Assuming that the magnetic field inside the conductor is restricted to a layer near the surface of thickness $\delta$, the current is also confined to this region. Calculating the effective resistance in the coil

$$\begin{aligned} R_c &= \frac{\rho l}{\pi(r^2 - (r-\delta)^2)} && (4.44)\\ &= \frac{\rho l}{\pi\delta(2r-\delta)} && (4.45)\end{aligned}$$

where r is the radius of the conductor. Hoult and Richards[75] write the resistance as

$$R_c = \frac{l}{2\pi r}\sqrt{\frac{\mu\omega\rho}{2}}$$

where the authors have assumed r $\gg \delta$. This model is modified due to the proximity effect between conductors. Current carrying conductors influence other currents through the magnetic field that it produces. The result of this effect is an increase in the resistance by a factor $\eta$.[75]

When imaging samples with non-zero conductivity, a resistance $R_s$ must be added in series with the coil resistance $R_c$. Noise is generated by random motion of electrons and ions in tissue producing an effective $R_s$ in the coil. Hoult and Lauterbur[76] have calculated an effective resistance due to the sample and shown that it varies as $\omega^2$. They then went on to write the signal-to-noise ratio for a solenoid or saddle coil as

$$SNR = \frac{\nu^2 B_1}{\sqrt{\epsilon n^2 \nu^{1/2} + \beta \nu^2 B_1^2 b^5}} \tag{4.46}$$

where $\alpha$, $\beta$, and $\epsilon$ are constants that depend on both the coil and the sample, and n is the number of turns. This can be rewritten in a more convenient form as a function of the magnetic field and the polarization

$$SNR \propto \frac{\gamma B P}{\sqrt{\alpha' B^{1/2} + \beta' B^2}}. \tag{4.47}$$

Hoult and Lauterbur[76] conclude that noise due to the conductivity of tissue dominates as the proton resonant frequency approaches 10 MHz (2,348 gauss). At these higher frequencies, the signal-to-noise is proportional to B for thermal polarization and is independent of field for polarized samples. For lower frequencies, the coil resistance dominates and the signal-to-noise varies as $B^{7/4}$ for thermal polarization and $B^{3/4}$ for polarized samples. Therefore, the optimum field for use with polarized gases is approximately 2,300 gauss.

In addition to the magnetic field dependence discussed above, the signal-to-noise ratio is dependent on sampling parameters. It is readily seen that the signal and the SNR from a given voxel is proportional to the voxel volume $V_{voxel}$. For 2-dimensional imaging, the voxel volume is defined as

$$V_{voxel} = \frac{FOV_x}{N_x}\frac{FOV_y}{N_y}\delta z$$

where $FOV_x$ ($FOV_y$) is the field-of-view in the x (y) direction, $N_x$ ($N_y$) is the number of samples in x (y) direction, and $\delta$z is the slice thickness. Data is collected using discrete sampling in k-space with intervals

$$\Delta k_x = \frac{\gamma G_x \Delta t}{2\pi} \tag{4.48}$$

$$\Delta k_y = \frac{\gamma \Delta G_y t_p}{2\pi} \tag{4.49}$$

where $\Delta t$ is the sampling interval in the frequency encoding direction, $\Delta G_y$, and $t_p$ are the step size and time duration of the phase encoding gradient. The field-of-views are then related to the k-space intervals: $FOV_x = 1/\Delta k_x = N_x \Delta x$ and $FOV_y = 1/\Delta k_y = N_y \Delta y$. Using equations (4.48) and (4.49), the field-of-views are then given as

$$FOV_x = \frac{2\pi}{\gamma G_x \Delta t} \tag{4.50}$$

$$FOV_y = \frac{2\pi}{\gamma \Delta G_y t_p}. \tag{4.51}$$

The spacing between pixels in the x and y is

$$\Delta x = \frac{2\pi}{N_x \gamma G_x \Delta t} \tag{4.52}$$

$$\Delta y = \frac{2\pi}{N_y \gamma \Delta G_y t_p}. \tag{4.53}$$

The signal-to-noise ratio is also proportional to $\sqrt{N_{acq}}$ where, for 2D imaging, $N_{acq} = NEX \times N_y$, $NEX$ is the number of signal averaging acquisitions, and $N_y$ is the number of phase encoding steps. The signal-to-noise is

$$SNR_{2D} \propto V_{voxel}\sqrt{NEX \times N_y}.$$

Based on equation (4.38), the noise is proportional to $\sqrt{\Delta\nu}$, where $\Delta\nu$ is the bandwidth. For a given voxel, only the frequencies within the range $\Delta\nu_{voxel}$ are encoded.

$$\Delta\nu_{voxel} = \frac{\Delta\nu_{FOV}}{N_x} = \frac{1}{N_x \Delta t} \tag{4.54}$$

The signal-to-noise ratio per voxel as a function of sampling parameters is

$$\begin{aligned} SNR_{2D} &\propto \frac{FOV_x}{N_x}\frac{FOV_y}{N_y}\Delta z\sqrt{\frac{NEX \times N_y}{\Delta\nu_{voxel}}} && (4.55) \\ &\propto \frac{FOV_x FOV_y \Delta z \sqrt{NEX\,\Delta t}}{\sqrt{N_x N_y}}. && (4.56) \end{aligned}$$

From this relationship, an increase in the signal-to-noise is produced by increasing the field-of-views, the slice thickness, the number of signal averages, or the sampling interval. The signal to noise is also increased by decreasing the number of frequency and phase encoding steps $N_x$ and $N_y$.

### 4.2.4 Spatial Resolution

Spatial resolution is the effect that controls our ability to distinguish between small, high-contrast objects and to reconstruct edges. Spatial resolution depends on the imaging technique and the physical properties of the system which are being studied. In the previous section, the spatial interval $\Delta x$ (equation 4.52) was derived in the frequency encode direction. For a given set of sampling parameters, $2\Delta x$ will be defined as the best possible resolution that can be achieved; for this reason $2\Delta x$ will be defined

$$\Delta x_{opt} = \frac{2}{N_x \Delta t}\frac{2\pi}{\gamma G_x}. \tag{4.57}$$

Processes such as diffusion and relaxation will decrease the resolution such that $\Delta x \geq \Delta x_{opt}$.

Relaxation in a sample has the effect of broadening the linewidth in frequency space, which then corresponds to an increase in the spatial resolution. To demonstrate this effect, a sample with a uniform transverse relaxation time $T_2^*$ is placed in a magnetic field. When a 90° pulse is applied, the magnetic moments will precess at frequency $\omega = \gamma$B about the B direction. The signal observed in the detection coil is S′(t). If the transverse magnetization decays with the time constant $T_2^*$, the observed signal is

$$S'(t) = S(t)e^{-\frac{t}{T_2^*}}$$

Using $k = \gamma G_x t/2\pi$ the signal in k–space can be rewritten

$$S'(k) = S(k)e^{-\frac{2\pi k}{\gamma G_x T_2^*}}.$$

Taking the Fourier transform of S$'$(k) provides the spin density $\rho$(x)

$$\rho'(x) = \int_{-\infty}^{\infty} S(k)e^{-\frac{2\pi k}{\gamma G_x T_2^*}} e^{i2\pi kx} dk$$

Using the convolution theorem

$$\frac{1}{2\pi}\int_{-\infty}^{\infty} F(\alpha)G(\alpha)e^{i\alpha x}d\alpha = \int_{-\infty}^{\infty} f(u)g(x-u)du = f(x) * g(x)$$

where F($\alpha$) and G($\alpha$) are the Fourier transforms of f(u) and g(u), finding

$$\rho'(x) = \int_{-\infty}^{\infty} \rho(x)\frac{\frac{2}{\gamma G_x T_2^*}}{(x-x')^2 + \left(\frac{1}{\gamma G_x T_2^*}\right)^2}.$$

This is the convolution of the real spin density $\rho$(x), with a Lorentzian of FWHM $\Delta x_{T_2^*} = \frac{2}{\gamma G_x T_2^*}$ and a corresponding frequency width $\Delta\nu_{T_2^*} = \frac{1}{\pi T_2^*}$. If $\Delta x_{T_2^*}$ is less than the size of the voxel, the resolution is limited by $\Delta x_{opt}$. If $T_2^*$ is sufficiently short so that $\Delta x_{T_2^*} > \Delta x_{opt}$, the resolution is limited by $T_2^*$ broadening. The optimal bandwidth is given by

$$\frac{1}{\Delta t} = \frac{N}{\pi T_2^*}$$

where $1/N\Delta t$ is the pixel separation in the frequency domain.

When dealing with liquids and gases, diffusion has an additional effect on resolution. When spins diffuse in the presence of magnetic field gradients, they dephase and cause a reduction in the transverse relaxation $T_2^*$. As illustrated above, a shorter $T_2^*$ decreases the achievable resolution. For an acquisition time $\tau$, the rms distance that a spin will diffuse in one dimension is $\Delta\eta_{dif} = \sqrt{2D\tau}$, where D is the diffusion coefficient.[80] For $^3$He, the diffusion coefficient was recently measured and reported:[64] D = (1.8±0.2) cm$^2$/s at P=1 bar and 20 °C. In addition, it has been shown[78] that the signal observed during a read gradient is attenuated by

$$e^{-\gamma^2 G_x^2 D t^3/3}.$$

Callaghan and Eccles[78] calculated the spread in the frequency domain by the convolution of this function with the spectrum

$$\Delta\nu_{dif} = 0.6(\gamma^2 G_x^2 \frac{D}{3})^{\frac{1}{3}}. \tag{4.58}$$

Unlike relaxation broadening, diffusion causes a gradient dependent linewidth. The choice of the optimum bandwidth for a constant signal-to-noise $1/\Delta t'$ is dependent on the gradient when diffusive effects dominate. For the diffusion optimum, the pixel spacing $1/N\Delta t'$ is on the order of $\Delta\nu_{dif}$. If the linewidth due to diffusion is greater than that from relaxation, $\Delta\nu_{dif} > 1/\pi T_2^*$, and for constant signal-to-noise, the resolution is given by

$$\begin{aligned} \Delta x &= \frac{2}{N\Delta t'}\frac{2\pi}{\gamma G_x'} && (4.59)\\ &= 1.78\left(\Delta\eta_{dif}^2 \Delta X_{opt}\frac{G_x}{G_x'}\right)^{\frac{1}{3}} && (4.60)\\ &= 1.34\left(\Delta\eta_{dif}\Delta x_{opt}^2\right)^{\frac{1}{3}} && (4.61) \end{aligned}$$

where $1/N\Delta t'$ and $G_x'$ are the pixel pair separation and gradient for diffusive broadening is

$$\Delta x_{opt} = \frac{2}{N\Delta t}\frac{2\pi}{\gamma G_x}$$

the $T_2^*$ optimal resolution and $\Delta x_{dif}$ is the distance the spin diffuses during the acquisition time $\tau$ $= N\Delta t$.

The spatial resolution can now be examined as a function of the gradient strength G for a constant signal-to-noise ratio. From equation (4.56) the signal–to–noise is related to the gradient and bandwidth by

$$\begin{aligned} SNR &\propto (FOV)^2\sqrt{\Delta t} && (4.62)\\ &\propto \left(\frac{1}{G^2\Delta t^{3/2}}\right). && (4.63) \end{aligned}$$

For the pixel limited case, the resolution is given by equation (4.52), which varies as $G^{1/3}$. At fixed signal-to-noise, the gradient must be reduced and for higher resolution, the sampling time $\Delta t$ must be increased for higher resolution. In the case where the pixel separation is smaller than the linewidth due to relaxation the resolution is given by

$$\Delta x = \frac{1}{\pi T_2^*}\frac{2\pi}{\gamma G}, \qquad (4.64)$$

which varies as $G^{-1}$. For the diffusion limited case, the resolution changes with $G^{-1/3}$.

Image resolution can also be effected by non–uniform field gradients that arise from a nonhomogeneous distribution of magnetization. When a diamagnetic material is placed in an external magnetic field the electron cloud surrounding the nucleus is distorted, producing a dipole moment. On the macroscopic level, a net change in magnetic field is observed and given by

$$B = (1 + \chi_m)B_0 \qquad (4.65)$$

where $\chi_m$ is the diamagnetic susceptibility of the material. Imaging of heterogeneous materials with spatially varying magnetic susceptibility produces linewidth broadening, resulting in image distortion and lower resolution. Image processing algorithms rely on a uniformly distributed grid of k-values which does not exist in the presence of non–uniform field gradients. A more thorough discussion of the effects due to magnetic susceptibility are given by Callaghan[100] and Schenck.[79]

### 4.2.5 Image Contrast

Image contrast is the ability to distinguish between two nearby objects. Contrast can be increased by optimizing pulse sequence parameters (flip angle, TR, TE, etc.) for objects or materials that have different $T_1$, $T_2$, densities, etc. As an example, protons in different tissues have different $T_2$'s and, thus, contrast can be accentuated by varying TE. High contrast objects are easily distinguished from one another and therefore, are limited by spatial resolution. Low contrast objects are limited by the contrast-to-noise ratio ($CNR$). For two objects that have slightly different signals,

$$\text{contrast} = \mathrm{S}' - \mathrm{S} = \delta \times \mathrm{S},$$

where $\delta$ is the fractional difference in the signal strengths

$$\delta = \frac{S' - S}{S}.$$

The contrast-to-noise ratio for two voxels is

$$\begin{aligned} CNR_{voxel} &= \left(\frac{\delta \times S}{S_{noise}}\right)_{voxel} && (4.66) \\ &= \delta \times SNR_{voxel} && (4.67) \end{aligned}$$

where $SNR_{voxel}$ is the signal-to-noise ratio per voxel. For low contrast objects it is important to have a large $SNR_{voxel}$.

## 4.3 Magnetic Resonance Imaging with Polarized Noble Gases

As shown in previous sections, for a given nuclear material, the signals in magnetic resonance imaging and nuclear magnetic resonance depend on the total magnetization. This magnetization varies with the density, polarization, and volume of the sample. Traditional MRI experiments are performed in magnetic fields ranging from approximately 10,000 to 100,000 gauss. The thermal polarization of protons in water at room temperature in a standard clinical imager at 15,000 gauss is approximately $5.18 \times 10^{-6}$. However, because of the high number density of water molecules, proton imaging is possible. $^3$He and $^{129}$Xe gases can be polarized to high levels and used for NMR and MRI. As discussed in chapter 3, high polarization of $^3$He and $^{129}$Xe can be achieved by spin-exchange with optically pumped rubidium vapor. Polarizations of $^3$He have been obtained in the tens of percent, while $^{129}$Xe polarizations are typically in the region of 10%. Since the number density of gas is much lower than that of water at room temperature, it is necessary to compare the ratio

$$\frac{n}{n_p}\frac{\mu}{\mu_p}\frac{P}{P_p},$$

where $n$ ($n_p$) is the gas (proton) number density, $\mu$ ($\mu_p$) is the nuclear magnetic moment of the gas atom (proton) and $P$ ($P_p$) is the polarization of the sample. For a 1 atmosphere sample of $^3$He polarized to 1% and a sample of water of equal volume at room temperature in a 15,000 gauss magnetic field, this ratio is approximately 0.6. Therefore, a sample of polarized $^3$He at 1 atmosphere and polarized to ~2% would produce a signal that is approximately equal to that of water at high field. Due to the independence of the noble gas polarization to magnetic field strength, this ratio increases to approximately 450 at 20 gauss. Since large polarizations can be achieved, signal averaging is not needed with polarized noble gas imaging reducing imaging time compared to traditional proton imaging where a delay on the order of $T_1 \approx 3$ seconds is needed to allow for the spins to relax towards thermal equilibrium.

Laser polarized gas MRI was first demonstrated in 1994[81] using polarized $^{129}$Xe and the lungs of a mouse. Polarized noble gases are ideal for imaging organs and other system with air spaces. Since the first demonstration in 1994, other experiments using polarized $^3$He have been conducted using the lungs of guinea pigs[82,83] and human airways.[84–86] One advantage of $^3$He over that of $^{129}$Xe is its greater magnetic moment and, therefore, its signal amplitude. Also, at this time polarized $^3$He is being produced in larger quantities and at a higher polarization than $^{129}$Xe. However, an advantage of $^{129}$Xe is its solubility in blood and other liquids, making it potentially useful for such studies as functional brain imaging[94] and NMR investigations of fluids. In addition to research, polarized gas MRI is being tested as a diagnostic and surgical planning tool for Chronic Obstructive Pulmonary Disease. This is a class of diseases that is the fourth leading cause of death in the United States, afflicting over 20 million people, and resulting in approximately 100,000 deaths per year.[87]

Figure 4-12 is an image of a 3 glass cylinder filled with 3 atmospheres of polarized $^3$He acquired with a GE Omega/CSI imager/spectrometer. The acquisition time was roughly 10 seconds. An interesting effect that is observed in this image is enhancement along the interface between the glass and gas due to restricted diffusion.[88,90] As a spin diffuses around in the presence of a magnetic field gradient, it precesses at a frequency that depends on its location. Once the spin has diffused away from its starting point it has lost phase coherence with its initial state. Similarly, the spin's resonant frequency is different from its starting point. The net result is a dilution in the signal. However, if the spin is near a surface and it returns back to its initial position, it will precess at its original frequency. The image will then show signal enhancement near surfaces. As seen in figure 4-12, the enhancement is only observed in one dimension, the read direction. This is because the spins permanently lose phase coherence after diffusing in a gradient.

## 4.4 Low-Field Imaging with Polarized $^3$He Gas

The use of polarized noble gases and their independence on the magnetic field enables their use with fast MRI at low-fields (≈100 gauss). Typical MRI spectrometers require the use of large magnetic fields (10,000 – 100,000 gauss) that are produced by expensive superconducting magnets. Magnetic fields on the order of 100 gauss are easily produced with small copper coils that require low power. Saam *et al.*[88] were the first to demonstrate the ability of one dimensional, low-field (31 gauss) imaging using polarized $^3$He. In addition, they also observed edge enhancement peaks due to restricted diffusion of the gas. Reported in the following sections are the first 2-D images of polarized $^3$He taken at low-field ( 21 gauss) with a custom low-field imager/spectrometer. Also included in this section are some results from investigations of the advantages of imaging at low-fields: lower distortions due to magnetic susceptibility mismatching and greater RF penetration (skin depth) due to lower frequencies.

### 4.4.1 Images and Imaging

Images were acquired using the custom made low-field imager/spectrometer of polarized $^3$He samples at roughly 21 gauss (66.868 kHz). Standard gradient echo pulse sequences were used to acquire these images. Figure 4-14 contains images of cells in the shape of a triangle and an "H". The triangular cell had a base width of 25.4 mm, a side length of 36.6 mm, and a thickness of 24.9 mm. The "H" shaped cell had a height and width of 23.9 mm and 23.9 mm, respectively, and a thickness of 22.9 mm. A photograph of these cells is shown in figure 4-15. Each cell was prepared with the same method discussed in chapter 3 and contain approximately 2.7 atmospheres of $^3$He and 100 torr of nitrogen. Polarization was obtained by illuminating each cell at approximately 160° for several hours with a 15 W laser diode in the fringe field of a 3 tesla 20 cm horizontal bore magnet. Images were

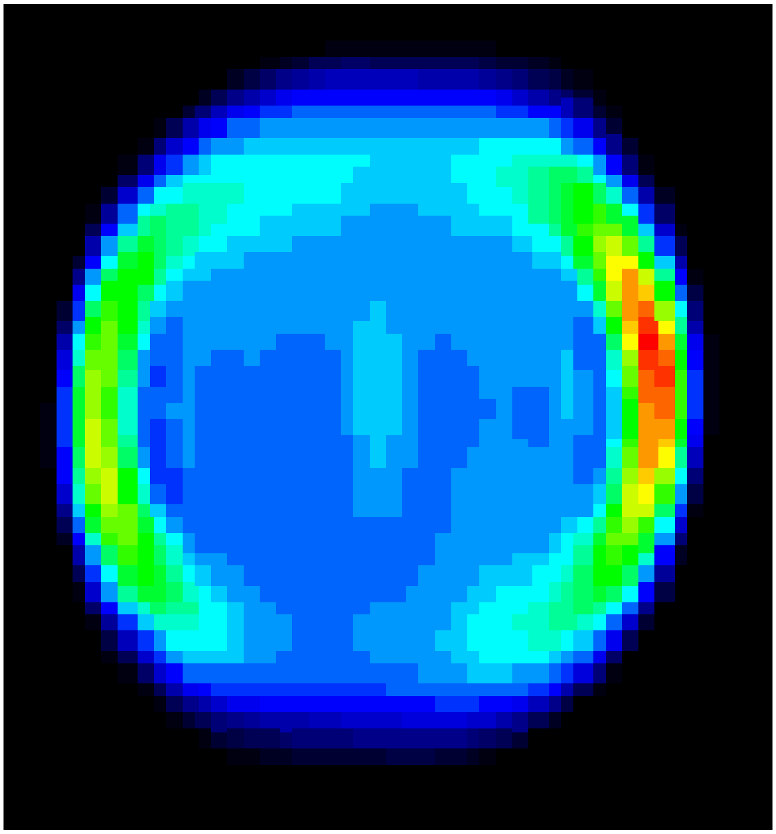

Figure 4-12: Image of a polarized $^3$He sample acquired with a 4.7 tesla commercial GE Omega/CSI imager/spectrometer. The increased intensity near the walls of the cell are due to restricted diffusion.

| | |
|---|---|
| Phase Encodes | 64 |
| Read Steps | 512 |
| Acq. Time | 128 msec |
| Bandwidth | 4 kHz |
| Read Gradient | $\sim$40 mgauss/cm |
| Phase Gradient | $\sim$1.6 gauss/cm/step |
| RF Pulse Width | 4 msec |
| $B_1$ | $\sim$1.1 mgauss |
| Flip Angle | $\sim$5 degrees |
| $FOV_x$ | 30.7 cm |
| $FOV_y$ | 9.7 cm |
| $\Delta x$ | 0.6 mm |
| $\Delta y$ | 1.5 mm |
| d1 | 62.5 msec |
| d5 | 4 msec |
| d8 | 0 msec |
| d10 | 20 msec |
| d15 | 1 msec |
| d20 | 1 msec |
| d30 | 0 msec |
| A1 | 9% max |
| A2 | -18% max |
| A3 | 18.6% |

Table 4.1: Low-field imaging parameters

acquired using a standard gradient echo pulse sequence with 64 phase encodes. No slice selection was used so the images represent a two dimensional projection through the cell. Based on the known cell dimensions and the number of pixels obtained from the unprocessed image, the pixel resolution was approximately $0.6 \times 1.5$ mm$^2$.

When materials with different magnetic susceptibilities are placed in a magnetic field there is a large localized magnetic field gradient near their interface. To demonstrate the benefit of having lower susceptibility induced field gradients at low fields, figure 4-16 contains images from a water sample at 4.7 tesla and a polarized $^3$He sample at 21 gauss with and without the presence of paramagnetic salts[1] in plastic tubes. The water sample is a Plexiglas disk with a grove in the shape of a “W″ filled with water. The “W” vertices are bounded by a square 1.905 cm × 1.905 cm and a line width of 3.175 mm. Note from the figure that the water image is severely distorted when the salts are placed near the sample and the $^3$He image shows little effect.

Traditional MRI does not include experiments that contain highly conductive materials due to the Faraday shielding of the RF field. Oscillating fields incident upon a conductive surface are

---

[1] gadolinium chloride, nickel chloride, magnesium chloride, and Magnevist (gadopentetate dimeglumine).

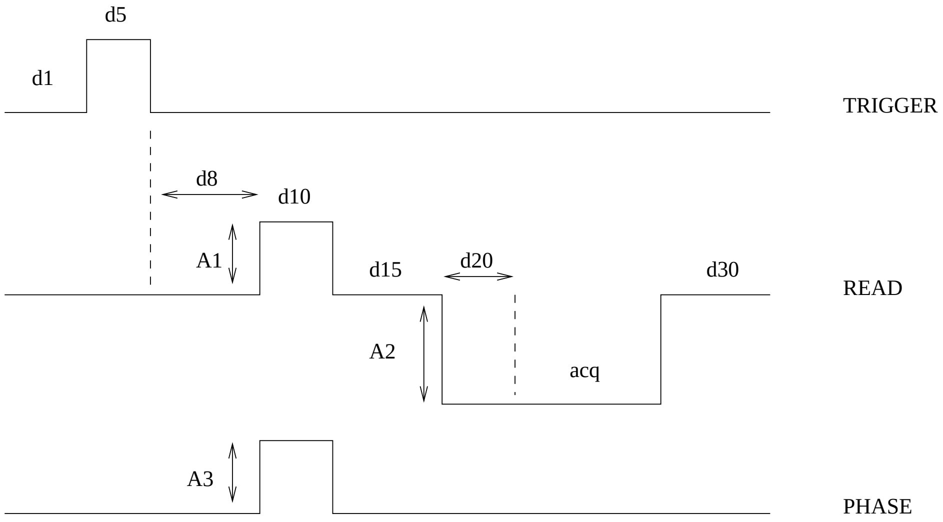

Figure 4-13: Delay diagram for the gradients and RF pulse. The values are given in table 4.1.

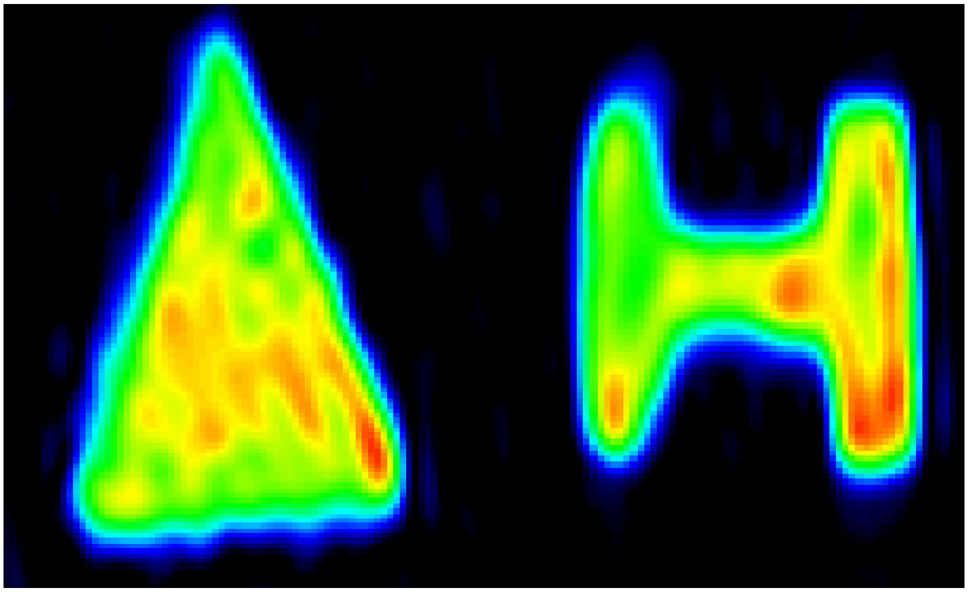

Figure 4-14: The first low-field images of polarized $^3$He gas.

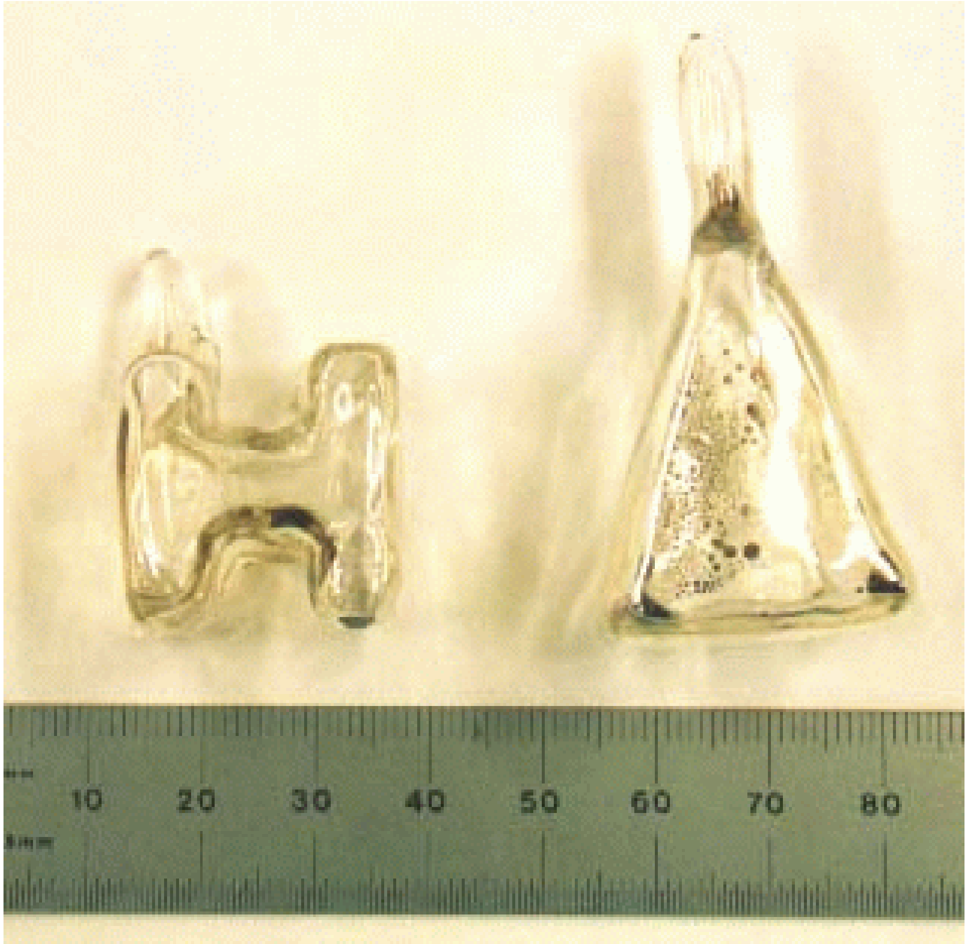

Figure 4-15: Photograph of the “H” and triangular shaped cells used for low-field imaging.

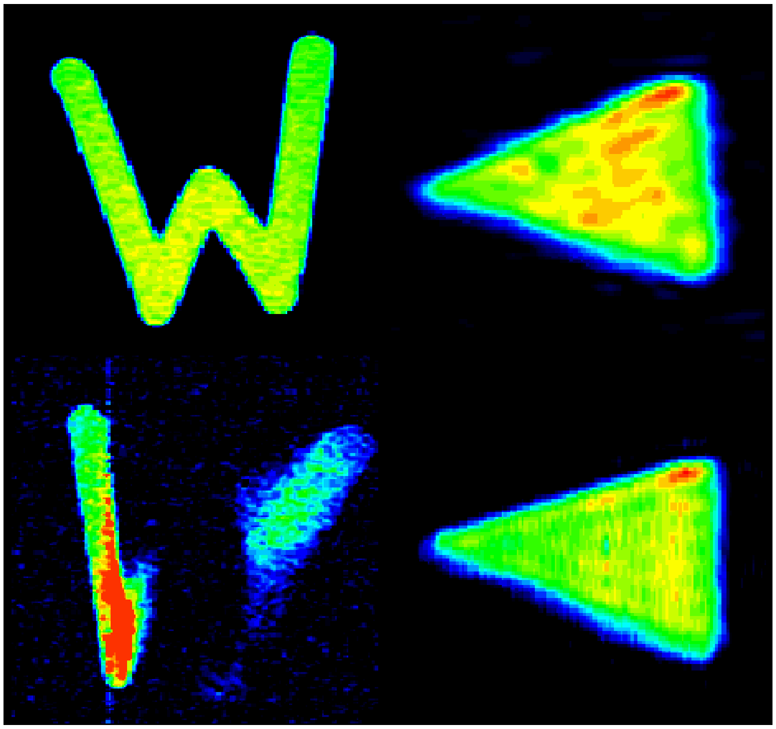

Figure 4-16: These are comparison images taken of a proton sample at 4.7 tesla and a polarized $^3$He sample at 21 gauss (66.868 kHz) both with and without the presence of highly paramagnetic salts. The upper left image is of a water sample without the salts and the lower left image is of the same water sample in the presence of the salts. The right images are of a wedge shaped cell filled with 3 atmospheres of polarized $^3$He; the upper image was without the the paramagnetic salts and the lower image was acquired with the salts.

attenuated within the conductor as

$$e^{-x/\delta}$$

where $\delta$ is the "skin depth" and is given by

$$\sqrt{\frac{2\rho}{\mu\omega}}.$$

$\rho$ and $\mu$ are the resistivity and permeability of the conductor, and $\omega$ is the angular frequency. As the frequency is reduced the penetration of the oscillating field is increased. It is this property that makes low field imaging potentially useful when the system of interest is conductive. When $^3$He is used to image a volume inside a brass cavity, the skin depth is .5 mm at 66.868 kHz (B $\approx$ 21 gauss) and 18.6 $\mu$m at 48.6 MHz (B=15,000 gauss). The flip angle is reduced due to the attenuation of the oscillating RF field $B_1$. And, additionally, the observed signal from the precessing magnetization is likewise reduced. The signal detected from a volume inside a conductive surface is

$$S_c \propto \frac{dM}{dt} \propto \omega M \sin\theta e^{-x/\delta}$$

where $\theta = \gamma\ B_1 e^{-\frac{x}{\delta}}\tau$. For a 1 mil (25.4 $\mu$m) thick brass enclosure, the observed signal would be roughly 90.2% of a signal without shielding. To demonstrate the ability to acquire images of samples in a conductive enclosure at low fields, high and low field images were taken with samples both inside and outside a box made from 1 mil (25.4 $\mu$m) thick brass shim stock. The high field images were acquired using a 4.7 tesla GE Omega/CSI imager/spectrometer, while the low fields were acquired with the custom imager at approximately 21 gauss (66.868 kHz). A standard spin echo pulse sequence was used for the high field proton images and a gradient echo sequence for the $^3$He images; figure 4-17 documents the acquired images.

To determine the gradient strength, one dimensional profile images were acquired. The gradient strength can be determined by

$$G = \frac{\Delta N}{N_r \Delta t}\frac{1}{\gamma l}$$

where $\Delta N$ is the number of channels in the profile, $N_r\Delta t$ is the acquisition time, and $l$ is the width of the cell. The measured read and phase gradient strengths are given in table 4.2 and plotted in figure 4-18 as a function of the percentage of the maximum current available from the Bruker/AMX console. Figure 4-19 is an example of a one dimensional profile of a 2.3 cm diameter spherical cell, which was acquired with the low–field imager.

Flip angle measurements were carried out by measuring the signal amplitude for 64 consecutive FID's. The natural log of the amplitude for each FID was plotted as a function of pulse (flip) number and was then fit to a line with a slope given by ln[cos($\theta$)]. Figure 4-20 is a sample data set plotted with a fit and figure 4-21 is the flip angle plotted as a function of RF amplitude for 1 and 2 ms pulses.

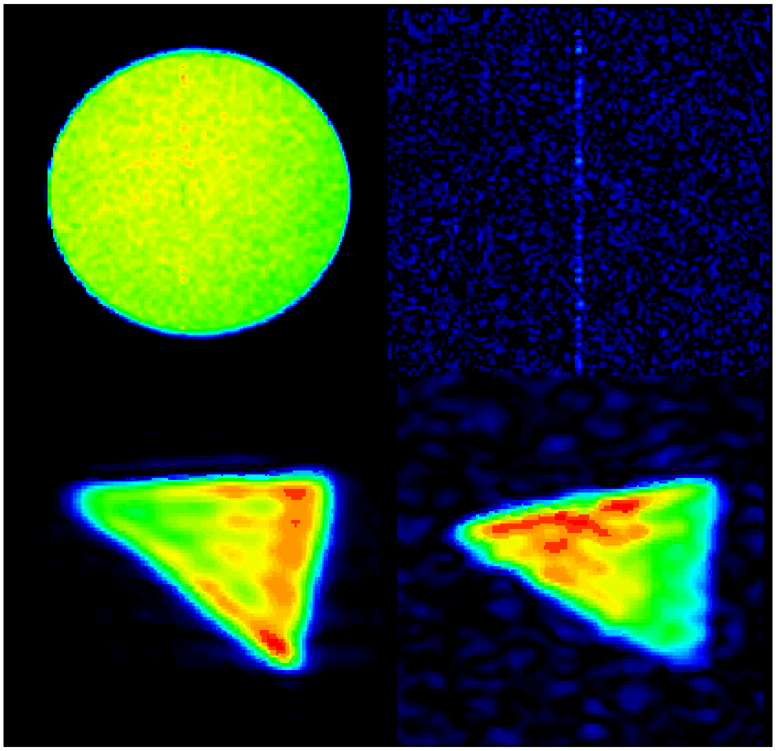

Figure 4-17: These are images taken of a proton sample at 4.7 tesla and a polarized $^3$He sample at 21 gauss (66.868 kHz) both with and without brass shielding. The upper left image is of a water sample without the shielding and the upper right image is of the same water sample inside brass box made from 1 mil (25.4 $\mu$m) thick brass shim stock. The lower images are of a wedge shaped cell filled with 3 atmospheres of polarized $^3$He; the left image was without the brass shielding and the right image was acquired with the cell inside the shielding.

| Gradient | Setting (%) | Strength (mgauss/cm) |
|---|---|---|
| z | 6 | 13 |
| z | 12 | 25 |
| z | 18 | 38 |
| z | 24 | 50 |
| z | 30 | 62 |
| y | 6 | 16.8 |
| y | 12 | 33.7 |
| y | 18 | 50.4 |
| y | 24 | 71.4 |

Table 4.2: Read and phase gradient strengths determined from a spherical cell of known dimensions.

### 4.4.2 Low–Field Rat Lung Imaging

In addition to glass cells, polarized $^3$He has been used in the imaging of excised rat lungs at 21 gauss (see figure 4-22); this is the first image of polarized gases in lungs at such low fields[2]. The low field lung image was acquired using 64 phase encode steps, $\sim$ 9.6° flip angle, a $\sim$ 3.9 mgauss/cm/step phase encode, gradient and $\sim$ 152 mgauss/cm read gradient. The pixel size is approximately 1.2 mm in the phase direction and .16 mm in the read direction. The total acquisition time was $\sim$ 12 seconds. The image was acquired with a concentric encoded gradient echo sequence. Previous low–field images used a sequential encoded gradient echo sequence. While this is acceptable for a sample that has a long $T_1$, lungs with shorter $T_1$ require more signal strength near $k_y = 0$. To accomplish this for the lung image, the pulse sequence was modified so that $k_y$ started at zero and concentrically stepped out to its maximum and minimum values.

In addition to the image, $T_1$ and $T_2^*$ data measurements were performed with a $T_1$ of $\sim$ 39 seconds and $T_2^* > 100$ ms. As documented in figure 4-25, $T_1$ was measured by acquiring 64 FID's and plotting the signal amplitude as a function of time. Folded into the data is the exponential decay due to $T_1$ and the loss of magnetization associated with flipping the magnetization for each of the 64 measurements. To extract, $T_1$ the flip angle had to be accounted for. Figure 4-26 is the data acquired for this $T_2^*$ measurement; $T_2^*$ is plotted as a function of the FID number. The non–constant value of $T_2^*$ is due to radiation damping effects.[39] The transverse polarization induces a current in the detection coil which dissipates power through resistive losses. The energy dissipated comes from a change in energy of the magnetization. The magnetization vector is tilted towards the lower energy state where $\vec{\mu}$ and $\mathbf{B}$ are parallel. In these measurements the spins were initially in their lower energy state before an RF pulse tipped the magnetization vector away from $\mathbf{B}$. The induced current then tilts the magnetization back to its initial state. $T_2^*$ will decrease as the polarization and/or flip angle is increased, caused by an increase in current induced in the coils. As illustrated in figure 4-26, $T_2^*$ increases with the FID number, since the magnetization (polarization) is decreasing with each FID. An additional experiment was performed using a spherical cell filled with $\sim$3 atmospheres of polarized $^3$He, 448 FID's were acquired and the corresponding $T_2^*$'s were determined. Figure 4-27 is

---

[2] Another group[89] has performed NMR with polarized $^3$He in human lungs, measuring a $T_1$ of 35 s and a $T_2$ of a few seconds at 1,000 gauss.

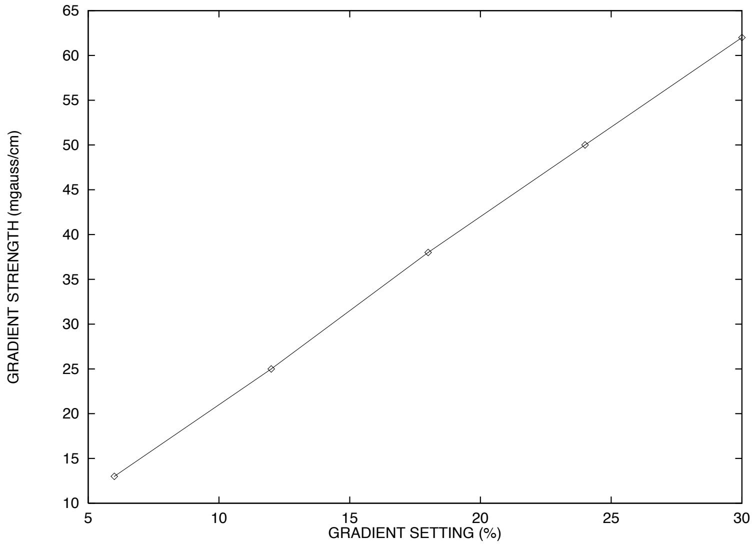

Figure 4-18: The z-gradient strength plotted as a function of the percentage of the maximum available from the AMX console and gradient power supplies.

a plot of $T_2^*$ as a function of the FID number. Again as with the lung data, $T_2^*$ increases with each FID (reduction in polarization). $T_2^*$ is seen to abruptly change at higher FID number due to loss of signal strength. Radiation damping will also change the observed flip angle and $T_1$ measurements.

When $^3$He was polarized in the high energy state, each FID first increased with time before beginning its decay to zero. The initial increase is believed to be due to radiation damping pulling the magnetization vector down towards the lower energy state, therefore, passing through the transverse plane where the detected signal is a maximum. More detail discussions on radiation damping in NMR are given by Xi-An *et al.*[91,93] and Jian-Xin *et al.*[92]

### 4.4.3 Optimal Magnetic Field Strength?

Based on the previous discussion on signal–to–noise, the choice for using high fields for imaging thermally polarized samples is clear. However, due to the nature of noble gas polarization, the optimum field is not as clear. From section 4.2.3 the signal–to–noise ratio was found to increase with frequency in the regime where the coil is the dominant source of noise until the sample noise dominated. Once the sample noise dominated, the signal–to–noise ratio was constant. Ideally, signal–to–noise would be independent of frequency (magnetic field strength) if the technology existed to produce superconducting detection coils with negligible noise. Current advances in superconducting quantum interference devices (SQUID)[95] could lead to higher signal–to–noise ratios and,thus, would be applicable to use in low–field MRI. TonThat *et al.*[96] have reported NMR of laser polarized solid $^{129}$Xe using SQUID detection. As documented in section 4.2.4, the pixel resolution was derived as a function of magnetic field strength with a 1/G dependence in each dimension. The limiting resolution is when the pixel and linewidth related resolutions are equal. Due to the reduction in linewidth broadening caused by magnetic susceptibility induced field gradients, imaging at low fields can potentially achieve higher resolution than at higher fields. The magnetic susceptibility induced fields are proportional to the applied field. Reduced susceptibility induced gradients have the effect of

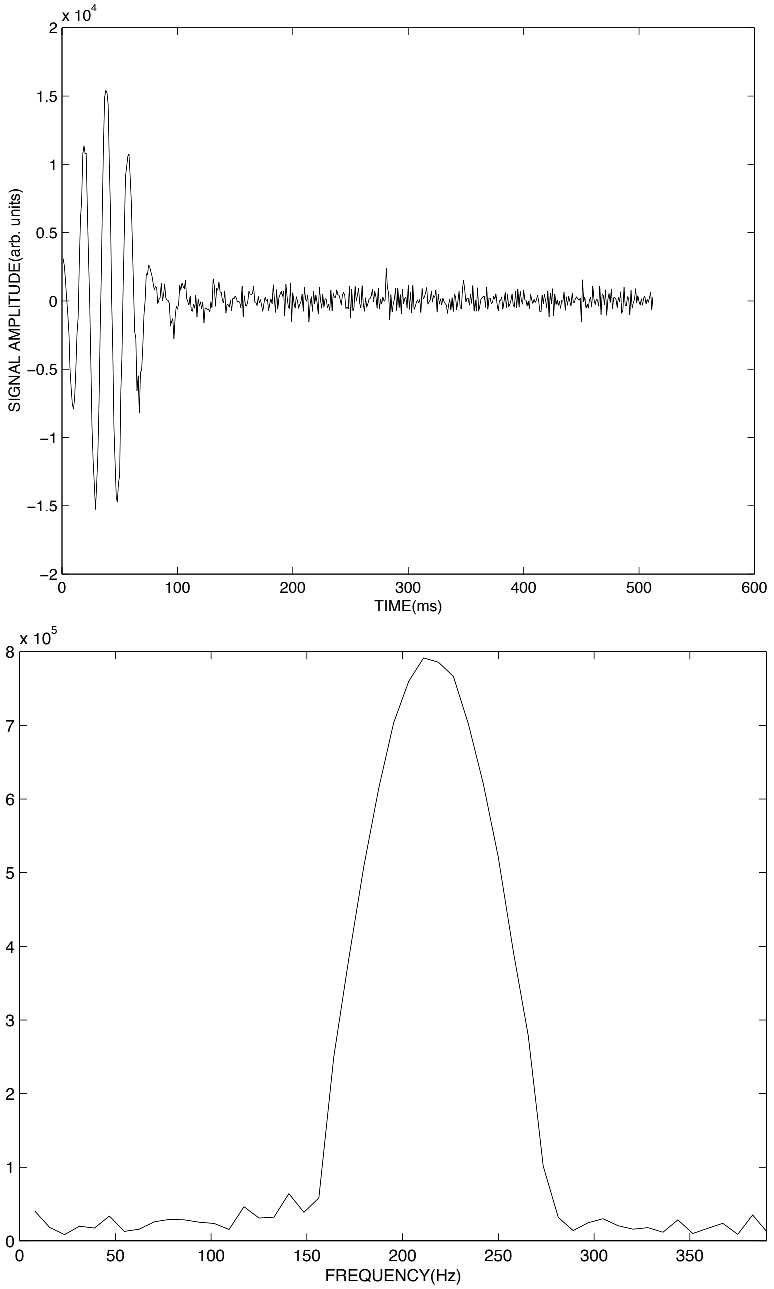

Figure 4-19: An example of an echo (top) and its Fourier transform (bottom) which was used to determine y and z gradient strengths using a 2.3 cm ID spherical cell.

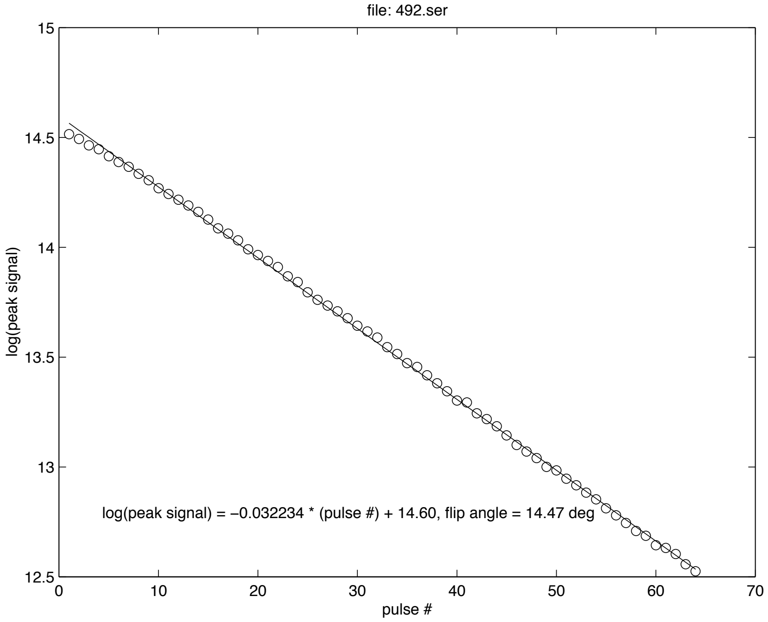

Figure 4-20: An example of a flip angle data set. The open circles are the peak heights of the Fourier Transform of 64 consecutive FID's, and the straight line is a fit to the data. The slope ($= \ln[\cos(\theta)]$) provides the flip angle.

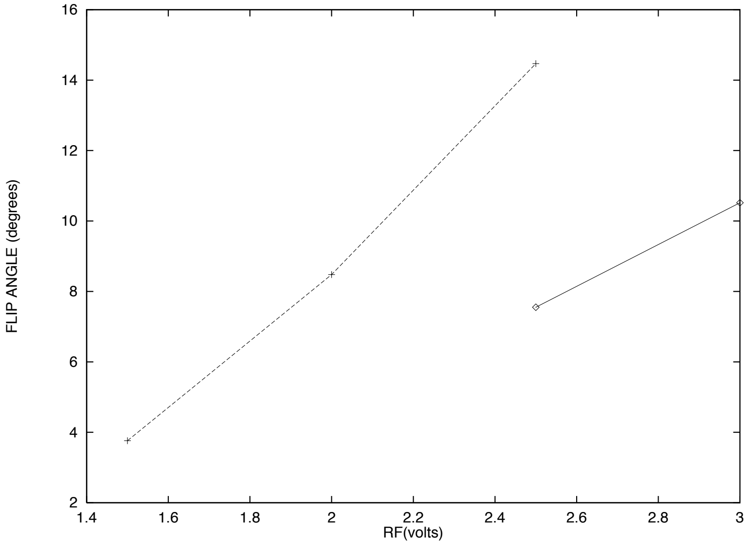

Figure 4-21: Flip angle data plotted against RF voltage. The left data set is for a 2 ms pulse width and the right for 1 ms.

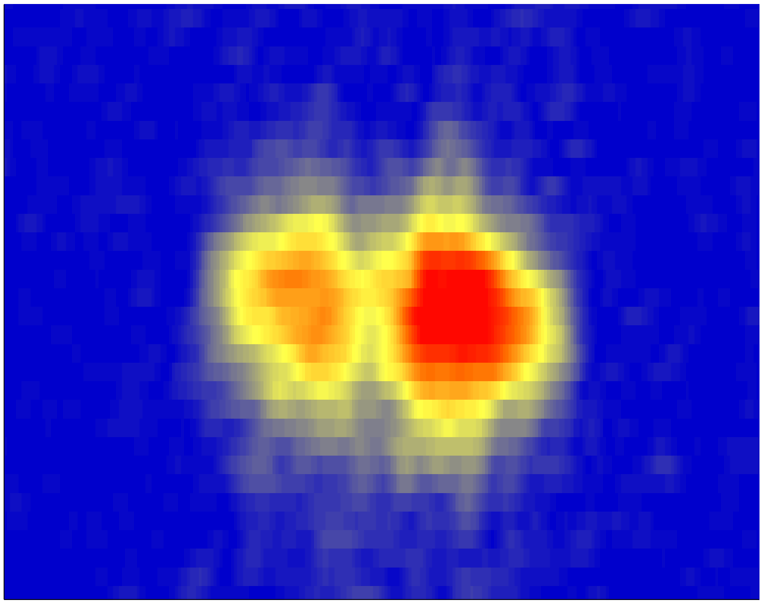

Figure 4-22: Low–field image of polarized $^3$He in an excised rat lung.

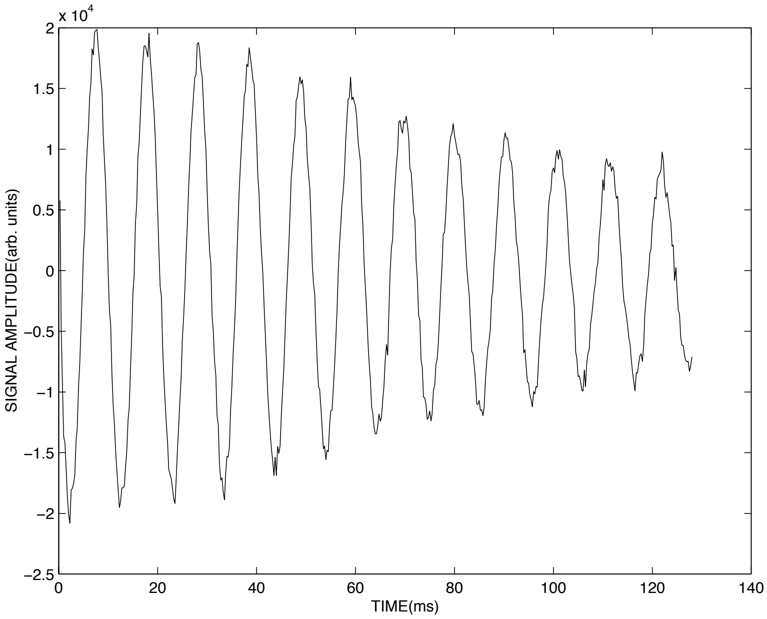

Figure 4-23: Real component of an FID acquired from polarized $^3$He in a rat lung.

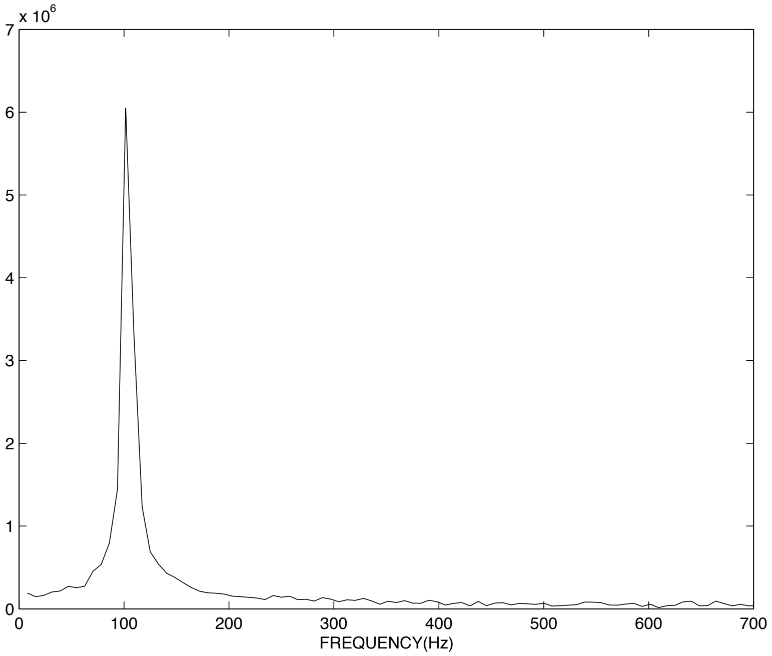

Figure 4-24: Fourier transform of an FID.

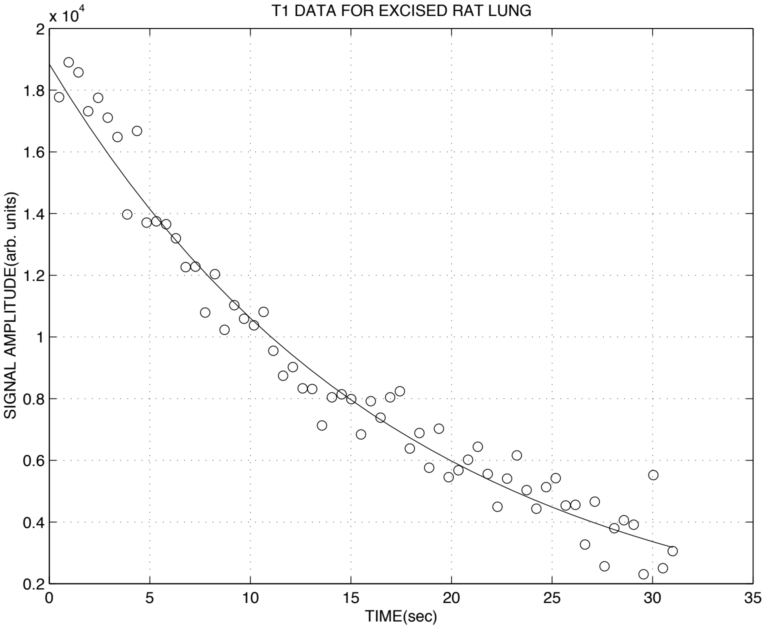

Figure 4-25: $T_1$ data for polarized $^3$He in excised rat lung at 21 gauss using a 10° flip angle. The fit to the data corresponds to a $T_1 \sim 39$ s.

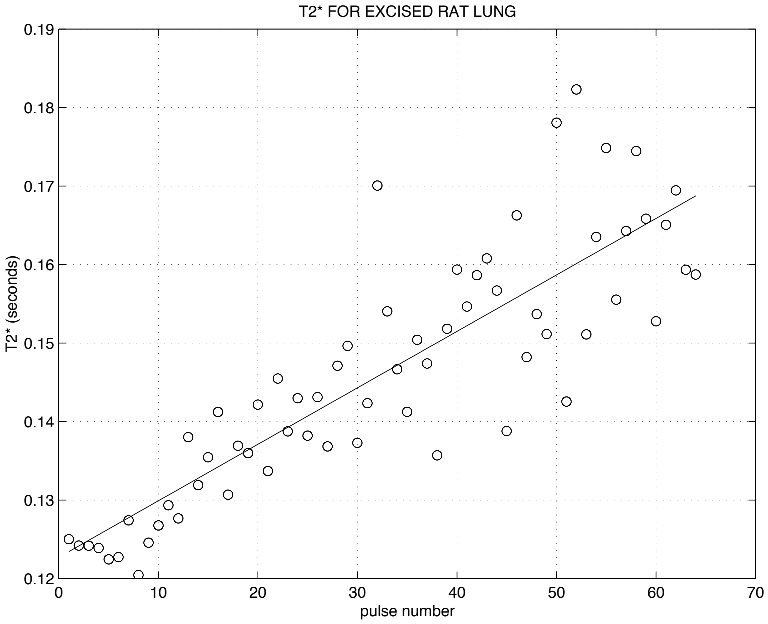

Figure 4-26: $T_2^*$ data for polarized $^3$He in excised rat lung at 21 gauss.

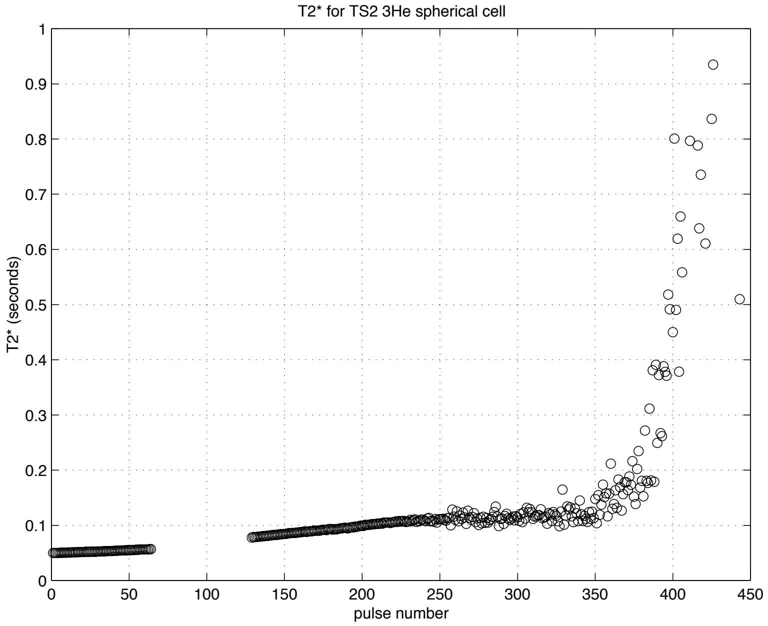

Figure 4-27: $T_2^*$ plotted verses the FID number for polarized $^3$He in a ~3 atmosphere spherical cell.

increasing $T_2^*$, and thus, the achievable resolution (see equation 4.64) if in the regime where resolution is not already limited by other effects (diffusion, pixel size). In the previous section $T_2^*$ was found to be greater than 100 ms for polarized $^3$He in rat lungs (at 21 gauss), compared to ~ 5 ms for polarized $^3$He absorbed into human (at 15,000 gauss) and guinea pig lungs (at 20,000 gauss).[97] The longer $T_2^*$ at 21 gauss is due to lower susceptibility induced gradients.

### 4.4.4 Experimental Setup

The low field images were acquired using a custom made solenoidal magnet, gradient set, RF and detection coils along with the use of a Bruker spectrometer/imager to control the gradients and for signal processing. The solenoid magnet design was taken from Hanson and Pipkin.[98] The solenoid was wound with four layers of 19 gauge copper wire around a 1.37 m long, 30 cm diameter aluminum cylinder. First, second and fourth order shim coils were included for shimming $B_z$. The solenoid was powered by HP6200B current supplies with a stability of roughly 1 part in $10^5$. The current was adjusted to produce a field of 20.62 gauss, which corresponds to a $^3$He resonant frequency of 66.868 kHz.

As shown in figure 4-28 the X and Y gradients ($G_x$,$G_y$) were produced by a saddle coil and the Z gradient ($G_z$) by a Maxwell pair.[100] The gradient coils were wound onto a G–10 cylinder with an outer diameter of 15.5 cm (= 2a). The Maxwell pair were two oppositely wound coils that were separated by $2d = \sqrt{3}a = 13.42$ cm, and contained 6 turns of magnet wire. The $G_x$ and $G_y$ coils were wound onto the same form as the Maxwell pair with a separation of $d_1 = 0.38a = 2.95$ cm and a total length of $d_2 = 2.55a = 19.76$ cm containing 6 turns of magnet wire per coil. The currents for the gradient coils were produced by a pair of power amplifiers which were controlled by the Bruker AMX console. Since a slice select gradient was not used, only the gradients $G_y$ and $G_z$ were used.

The RF field was produced by a pair of square coils with dimensions 7.25 cm by 7.25 cm, and they were separatated by 8.8 cm with 6 turns of number 25 magnet wire. Perpendicular to the RF coils was a pair of pickup coils that were wound onto groves in Nylatron GS plastic discs. Each coil was separated into two coils with a distance of 4 mm. The breaking up of the coils was performed with the intent of increasing the quality factor Q, by decreasing the capacitance between the windings. The distance between the two inner coils is 4.6 cm and 5.4 cm between the outer coils. 100 turns of number 32 magnet wire is wound into each .254 cm wide by 6.86 diameter groove for a total of 400 turns. The coils are center tapped, with the signals being obtained from the beginning of the first coil and from the end of the last coil. In order to tune the resonance frequency to 66.868 kHz with a Q of approximately 35 a external capacitor is placed across the leads from the pickup coil.

Placed between the gradient coils and the RF/pickup coil assembly, was a ground plane made from copper screen to reduce noise from the gradient coils and any capacitive coupling between the pickup coils and the rest of the apparatus.

The electronics diagram for controlling and acquiring the images is shown in figure 4-29. The RF coils are driven by a Wavetek model 29 10 MHz DDS function generator. The RF is turned on by gating the function generator with a signal of length $\tau$ from the Bruker AMX console. The gate also triggers an SRS DS345 function generator, which was programmed to produce a logic pulse (6 ms) to blank the preamplifier during RF excitation. This blanking pulse was longer than the trigger pulse so that ringdown in the coils was not detected. The output of the preamplifier was connected to a SRS SR830 DSP lock–in amplifier. This signal was referenced to the output of the Wavetek frequency function generator. The phase sensitive X and Y outputs from the lock-in were then sent to the Bruker spectrometer/imager for 1 and 2-D processing.

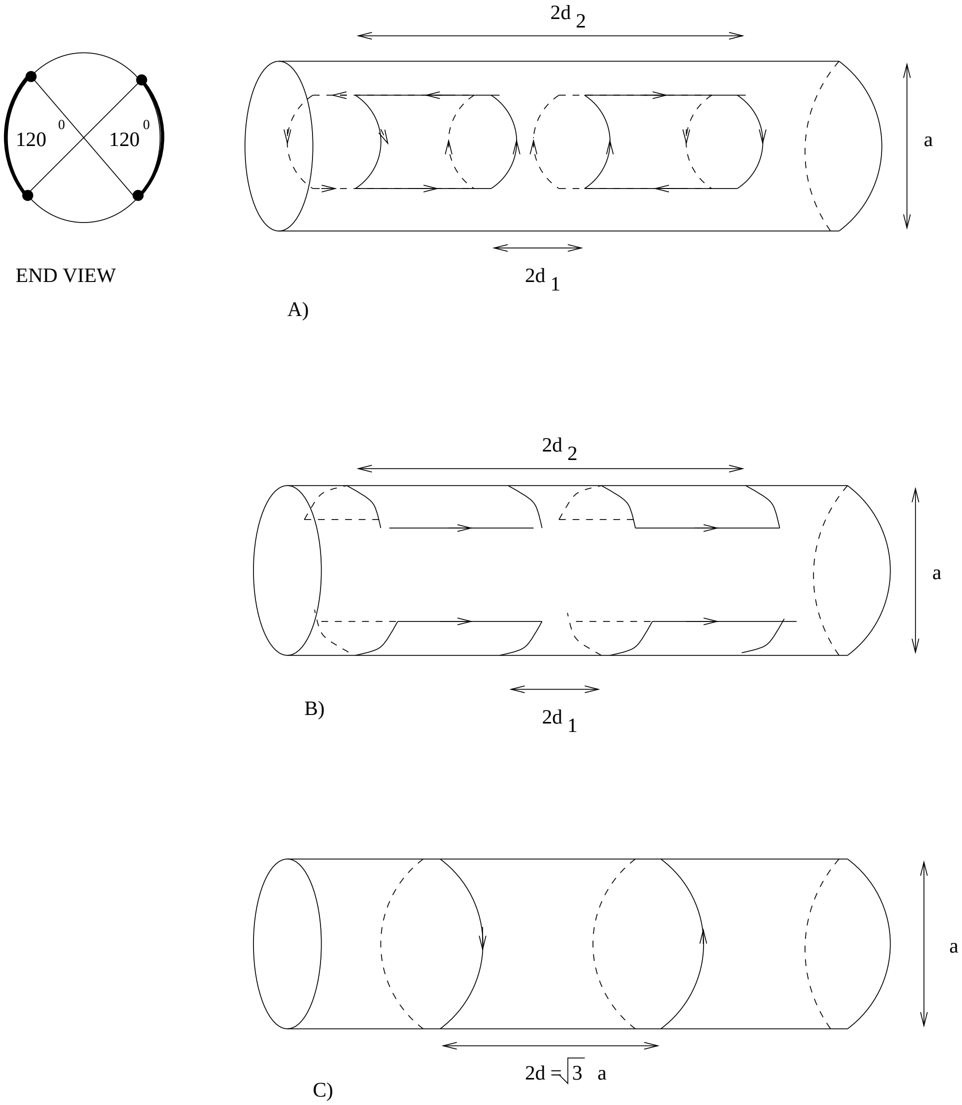

Figure 4-28: Figure A) shows the coils used to produce the x-gradient and figure B) is of the y-gradient coils. The dimensions are $d_1$ = 2.95 cm, $d_2$ = 19.76 cm and a = 7.75 cm. Figure C) is of the Maxwell pair used to produce the z-gradient. The dimensions for these coils are d = 6.71 cm and a = 7.75 cm.

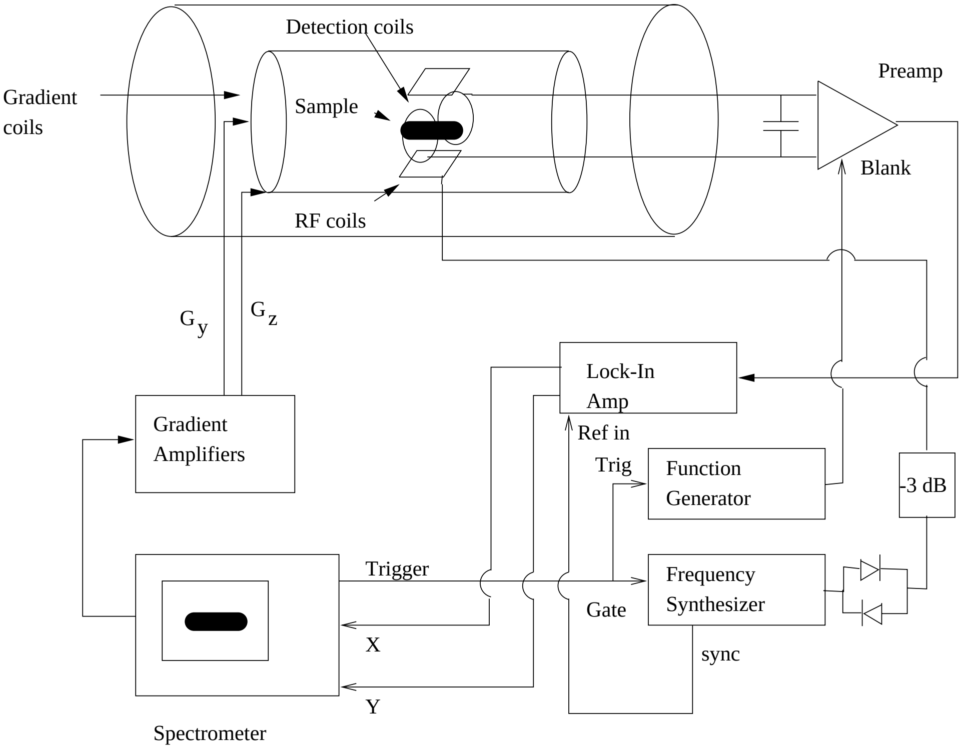

Figure 4-29: Diagram of the low field experimental setup.

### 4.4.5 $^3$He Cells and Polarization

The samples used in the low field experiments were fabricated in the same manner as described in chapter 3. Typically the smaller cells were connected to the vacuum system in a string. Three cells with different geometries were used in this process; the first two were made from Corning 7740 (Pyrex), and the third from Corning 1720 (aluminosilicate glass). The first cell was in the shape of an H with a height of 23.9 mm, a width of 23.9 mm, and a thickness of 22.9 mm. The second cell was in the shape of an isosceles triangle with a base length of 25.4 mm and equal sides lengths of 36.6 mm. The thickness of this cell is 24.9 mm. To produce 100 torr of nitrogen and 2.7 atmospheres of $^3$He at 23 °C, both of these cells were filled while submerged in liquid nitrogen. Photographs of these cells are shown in figure 4-15.

The polarizing occurred in the fringe field of a nearby magnet. For the low field images, this field was produced by a 3T 20 cm horizontal bore magnet while the high field images were polarized in the fringe field of a 4.7T 30 cm horizontal bore magnet. The cells were polarized by heating to approximately 170 °C in a hot air oven made from either glass or glass filled nylon, and then illuminated with 795 nm (FWHM ~3 nm) light from a 15 W fiber coupled diode[65] laser for 3 to 4 hours. Before imaging, the cells were cooled to room temperature and then placed in the RF/pickup coil apparatus at the center of the solenoid magnet.

In the rat lung studies, a polarized gas delivery system shown in figure 4-30 had to be developed. The cell had a $\sim$ 65 cm$^3$ cigar shaped geometry with an o–ring valve connected by a 20 cm long piece of capillary tubing (6 mm OD, 1.5 mm ID). The capillary was used to reduce the conductance between the cell and the valve. The valve o–rings were made from Ethylene Propylene (E.P.).[99] E.P. o–rings were chosen for their resistance to alkali metals. The cell had a measured relaxation time of approximately 28 hours at 12 gauss. The cell was connected to the delivery manifold which consisted of a sorption pump cooled with liquid nitrogen for evacuating the system, a line to a rough pump for removal of unpolarized helium gas between measurements, and a syringe that is used to inject the polarized $^3$He in to the lungs. The system allowed for repeated measurements with a low risk of contaminating the cell.

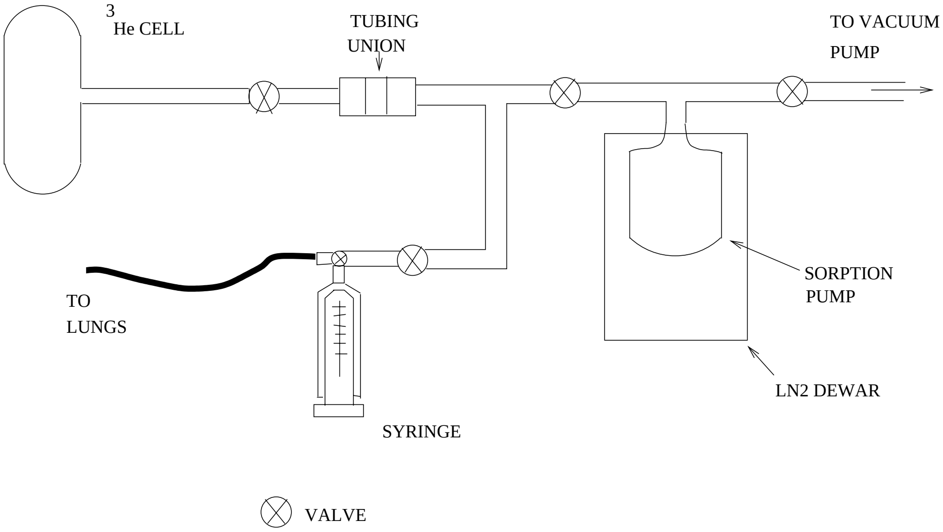

Figure 4-30: Delivery system used for the rat lung experiments.

*"... what immortal hand or eye could frame thy fearful symmetry?"*

*— William Blake*

# Chapter 5

# Polarized $^3$He Neutron Spin–Filters

## 5.1 Introduction

Polarized neutrons are used in a wide variety of studies ranging from fundamental physics experiments to the study of magnetic materials in condensed matter research.[101] Polarized neutrons beams are of great interest for investigations of fundamental symmetries such as parity and time invariance which are crucial to our understanding of the fundamental forces of nature. In addition to elementary particle physics measurements, polarized neutron scattering has proven to be a powerful tool in condensed matter research. Moon *et al.*[103] pioneered the technique of polarized neutron scattering to separate relevant cross sections. Some important examples are the separation of nuclear from magnetic scattering and measurements of the magnetic moments, magnetization density distributions, and magnetic form factors in paramagnets and ferromagnets.[104]

The kinetic energy of the neutron is expressed in units of energy or wavelength. The velocity of a low energy neutron is $v = \sqrt{\frac{2E}{m}}$ and the de Broglie wavelength is $\lambda = h/mv = h/\sqrt{2mE}$, where $h$ is Planck's constant, $m$ is the neutrons mass and $E$ is its kinetic energy. The relationship between energy and wavelength is

$$E = \frac{.81787}{\lambda^2}$$

where $\lambda$ has units of nm and $E$ is in meV. Additionally, the kinetic energy of the neutron can be expressed as a temperature using the relationship

$$T = \frac{E}{k(1000)}$$

where $k = 8.617385 \times 10^{-5}$ eV/K, $E$ is in meV and $T$ is in Kelvin. Table 5.1 compares neutron energy ranges with temperature.

There are several methods for polarizing low energy neutrons.[101,102] Polarizing crystal monochromaters utilize a magnetized ferromagnetic single crystal, such as $\mathrm{Co}_{0.92}\mathrm{Fe}_{0.08}$, to produce a monochromatic (mono–energetic) polarized beam of neutrons by Bragg reflection. Such devices produce intensities far below the requirements for many experiments and are not broad–band sources of neutrons. Supermirrors[105] produce cold neutron beams with high polarization and transmission, but are unable to polarize thermal and hot neutrons effectively and also create divergent neutrons and high gamma ray backgrounds. Polarized cryogenic proton targets[106] have also been used to polarize epithermal neutrons. The demands of producing and maintaining a polarized proton target, and the large fields required that may contribute systematic effects to the experiment, make their use impractical for many applications. These current methods of producing polarized neutron beams have been far below the demands of many experiments.

Due to its large neutron spin dependent absorption cross section, polarized $^3$He can be used to form a broad–band neutron spin–filter. $^3$He based spin–filters produce highly polarized neutron

| Neutron Energy (meV) | Temperature |
|---|---|
| $< 10^{-7}$ | Ultracold |
| 0.1 – 10 | Cold |
| 10 – 100 | Thermal |
| 100 – 500 | Hot |
| $> 500$ | Epithermal |

Table 5.1: Neutron energy ranges and temperature relationships.

beams over a wide range of neutron energies. By changing the thickness of $^3$He gas, the spin–filter may be operated in different neutron energy ranges to obtain the desired neutron polarization and flux. $^3$He based spin–filters also produce uniformly distributed polarized neutron beams with low divergence. Neutron polarizers based on $^3$He also increase the available flux of polarized neutrons when using a spallation source since time–of–flight information can be used rather than chopping the beam or using a monochromator to determine the neutron energy.

## 5.2 Fundamental Physics with Polarized Neutrons

Polarized neutrons are used for the study of parity violating effects, free neutron decay, determination of the electric and magnetic dipole moments of the neutron, time reversal violation and other polarized neutron effects.[107] In this section, an introduction to fundamental symmetries will be given along with two examples of symmetry violation that can be explored with polarized neutrons.

### 5.2.1 Fundamental Symmetries

In nuclear and particle physics, parity (P), charge conjugation (C), and time reversal (T) were thought to be symmetric transformations up into the 1950's. A charge conjugation operation means the particle is replaced by its antiparticle. Charge conjugation reverses the sign of the charge (Q $\rightarrow$ –Q), magnetic moment ($\mu \rightarrow -\mu$), magnetic field strength ($\mathbf{B} \rightarrow -\mathbf{B}$) and electric field strength ($\mathbf{E} \rightarrow -\mathbf{E}$), while preserving the sign of the momentum ($\mathbf{p} \rightarrow \mathbf{p}$) and ($\mathbf{J} \rightarrow \mathbf{J}$) spin. In order for particle–antiparticle symmetry to occur, the physical laws must be invariant under charge conjugation. This means a physical process must occur with the same probability for both the particle and its antiparticle. Charge conjugation symmetry is violated by free neutrinos and their antineutrino; the spin of the free neutrino is antiparallel to its momentum while the spin of the antineutrino is parallel to its momentum.

A parity operation causes an inversion in a spatial coordinate ($\mathbf{r} \rightarrow -\mathbf{r}$), but has no effect on time. The spatial parity operation changes the sign of the momentum ($\mathbf{p} \rightarrow -\mathbf{p}$) and electric field ($\mathbf{E} \rightarrow -\mathbf{E}$), while preserving the sign of the angular momentum ($\mathbf{L} \rightarrow \mathbf{L}$), spin ($\mathbf{J} \rightarrow \mathbf{J}$), and magnetic field ($\mathbf{B} \rightarrow \mathbf{B}$). Parity conservation requires the probability of a certain physical process and a mirror reflected process to be the same. If $|\alpha\rangle$ is a nondegenerate parity conserving state of a system, then a parity operation gives

$$P|\alpha\rangle = \pi|\alpha\rangle$$

where the eigenvalue is $\pi=\pm 1$; the positive and negative signs correspond to even and odd parity states respectively.

In 1956 Lee and Yang[108] theoretically showed that there was no evidence of parity conservation in the weak interaction; this leads to a mixture of parity even and parity odd states

$$|\alpha\rangle = a|even\rangle + b|odd\rangle.$$

Non–conservation of parity requires that the parity operator does not commute with the Hamiltonian: [H,P] $\neq$ 0. For $b \neq 0$, $|\alpha\rangle$ is no longer a eigenstate of the parity operator

$$P|\alpha\rangle = a|even\rangle - b|odd\rangle \neq \pi|\alpha\rangle.$$

This indicates that the Hamiltonian should contain pseudoscalar quantities that reverse sign under a parity transformation, for instance **s**·**p** where **s** is an axial vector (spin) and **p** is a polar vector (momentum). In 1957 Wu *et al.*[109] demonstrated that parity was not conserved in beta decay using the reaction

$$^{60}Co \rightarrow ^{60}Ni + e^- + \bar{\nu}$$

which is governed by the weak interaction. The experiment was carried out using a large magnetic field to polarize $^{60}$Co nuclei and looking for an asymmetry in the ejected electron relative to the magnetic field ($^{60}$Co nuclear spin) direction. An asymmetry was observed leading to the conclusion that parity was not conserved in the weak interaction. However, parity is still thought to be conserved in the strong and electromagnetic interactions.

In addition to charge and parity violations, CP nonconservation was observed in the decay of neutral kaons by measurement of the branching ratio[110]

$$\frac{K_L^0 \rightarrow \pi^+\pi^-}{K_L^0 \rightarrow allmodes} \neq 0,$$

where $K_L^0$ is the long lived neutral kaon. Since CP$|K_L^0\rangle = -|K_L^0\rangle$, CP$|\pi\pi\rangle$=$|\pi\pi\rangle$, and CP$|\pi\pi\pi\rangle$=–$|\pi\pi\pi\rangle$, CP invariance requires $K_L^0$ to decay into three pions Therefore, $K_L^0$ is not an eigenstate of CP.

Under a time transformation t → –t, and the signs of the momentum (**p** → –**p**), angular momentum (**L** → –**L**), spin (**J** → –**J**), and magnetic field strength (**B** → –**B**) are inverted while leaving the spatial coordinate (**r** → **r**), and electric field (**E** → **E**) remain unchanged.

Invariance with respect to all three transformations is assumed to exist. Therefore, for any interaction [CPT,H]=0. This states that a physical process before a combined transformation of C, P, and T, ie from our world to the parity reflected time reversed antiworld, must behave identically after the transformation. CPT conservation would requires that the masses, half–lives, and magnetic moments are identical for particles and their antiparticles. No violation of CPT has been found. The conservation of CPT forces T noninvariance when CP is not conserved. To date, the kaon system is the only known observation of CP violation. Additionally, no direct observation of T violation has been found. Searches for T violation are ongoing in such measurements as the electric dipole moment (EDM) of the neutron[111] and the triple angular correlation $\mathrm{D}\hat{\mathbf{S}}_n \cdot (\mathbf{p}_e \times \mathbf{p}_p)$ in polarized neutron decay.[112]

### 5.2.2 Measurement of the Pion–Nucleon Weak Coupling Constant

In this section, fundamental physics with polarized low energy neutrons is motivated by the proposed experiment to measure the parity–violating gamma asymmetry $A_\gamma$ in the capture of polarized cold neutrons by para–hydrogen, $\vec{n}$ + p → d + $\gamma$, at the Los Alamos Neutron Science Center

(LANSCE).[118] The gamma asymmetry, $A_\gamma$, is primarily sensitive to the pion–nucleon weak coupling constant $H_\pi^1$ which is essential for understanding parity–violating phenomena in nuclei. Measurement of $H_\pi^1$ will also test current theories of the meson–exchange picture of the hadronic weak interaction.

Experiments have been carried out to test the weak interactions in leptonic and semileptonic processes. However, the hadronic weak interaction remains elusive. Hadronic weak interactions can only be studied when the much larger interactions, the strong and electromagnetic, are forbidden by a symmetry principle. The weak amplitudes are typically much smaller than the strong ones, on the order of $10^{-7}$ at low energies. In order to study the nucleon–nucleon weak interaction, parity nonconserving processes must be observed to isolate the weak interaction in the much stronger background of the strong interaction. Theory predicts a suppression of the neutral weak current in $\Delta S=1$ and $\Delta C=1$ where S and C are strangeness and charm respectively. Therefore, the neutral weak current between quarks can only be studied in flavor–conserving processes. The nucleon–nucleon interaction is the only experimentally accessible system to study neutral weak currents between quarks.[119] A measurement of $A_\gamma$, which is primarily sensitive to $H_\pi^1$ will test theories that predict its value and what contribution neutral weak currents have.

The standard model is believed to be an accurate description of the natural world through its constituents (quarks, electrons ,muons, tau, and their neutrinos) and their forces of interaction (hadronic, electromagnetic, and weak). The gauge bosons responsible for carrying the forces are gluons, photons, and the $W^\pm$ and $Z^0$ for the hadronic, electromagnetic and weak forces respectively. The standard model is thought to accurately describe the weak interactions of leptons and their neutrinos. Leptons couple to their neutrinos with a universal weak coupling. However, the standard model cannot calculate the weak interactions between composite hadrons. The weak interaction between quarks is more complicated since linear combinations of quark fields rather than quark fields themselves are involved. The hadronic weak interaction is responsible for parity–violating phenomena in nucleon–nucleon interactions and nucleons in nuclei. A model of the strong interaction is needed to calculate the weak interactions of hadrons. Quantum chromodynamics (QCD) may be a correct theory but to date it is not possible to work out its consequences at low energy.

The weak interaction between quarks is mediated by the exchange of the $W^\pm$ and $Z^0$ bosons. At energies relevant for nucleon–nucleon interactions the range of the $W^\pm$ and $Z^0$ are much shorter than the distance between nucleons. $\pi$, $\rho$, and $\omega$ mesons are responsible for mediating the weak force between nucleons. The mesons are produced by the decay of a weak boson emitted from a quark which traveled a short distance before decaying. The meson then couples strongly to the other nucleon.

A qualitative argument given by Adelberger and Haxton[119] describing the quark–quark weak current implies the charged–current weak component is suppressed for $\Delta I=1$ while the neutral–current weak component is not. The neutral weak current is expected to dominate the $\Delta I=1$ component of the parity non–conserving nucleon–nucleon interaction. In the nucleon–nucleon meson exchange picture the weak pion exchange dominates the interaction due to its light mass compared to the other mesons. Weak pion exchange is a long range component of the nucleon-nucleon weak interaction which makes its effects most likely calculable.

$H_\pi^1$ has been extracted from measurements of $P_\gamma$, the circular polarization from a parity forbidden 1081 keV gamma transition in $^{18}F$.[119] This measurement currently is interpreted as an upper limit: $H_\pi^1 \leq 1.3 \times 10^{-7}$. A theoretical estimate from the quark model and weak SU(6) symmetry by Desplanques[120] is $0 < H_\pi^1 < 6.0 \times 10^{-7}$. Henley *et al.*[121] performed a QCD sum rule calculation of $H_\pi^1$. Their result leads to a prediction of $H_\pi^1 = 5.0 \times 10^{-8}$. Other theoretical predictions[122,123] have been performed with no agreement.

The determination of $H_\pi^1$ can be accomplished to a good degree of accuracy by measuring the

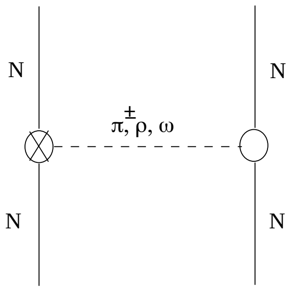

Figure 5-1: One boson exchange diagram in the weak N–N interaction. The cross indicates a weak vertex, the open circle a normal meson–nucleon vertex.

gamma ray asymmetry with respect to the neutron spin direction $A_\gamma$ in the reaction $\vec{n}$ + p → d + $\gamma$. $H^1_\pi$ is related to the asymmetry[119] by

$$A_\gamma = -0.045(H^1_\pi - 0.02H^1_\rho - 0.02H^1_\omega + 0.04H^{1'}_\rho)$$

where the other coupling constants due to the exchange of heavier mesons only contribute to the asymmetry at the few percent level.

The experimental setup for the measurement of $A_\gamma$ using the reaction $\vec{n}$ + p → d + $\gamma$ is shown schematically in figure 5-2. The neutrons will be produced by bombarding a tungsten target with 800 MeV protons at an intensity of 200 $\mu$A (recent upgrade) at the LANSCE facility. The spallation neutrons are then moderated with a liquid hydrogen moderator. Next the neutrons are transported through a biological shield with a super–mirror neutron guide to increase the flux at the target. The neutrons are polarized with a $^3$He spin–filter and their spin reversed with an RF spin flipper to lower systematic errors. The polarized neutrons are then captured in a liquid para–hydrogen target producing 2.2 MeV gamma rays which are detected in an array of CsI detectors surrounding the target. A $^6$Li absorber is placed between the target and detectors to absorb scattered neutrons using the reaction

$$n +^6 Li \rightarrow^7 Li^* \rightarrow \alpha + t$$

where there are no photons produced. A liquid para–hydrogen target is used in order to minimize neutron depolarization in the target. Liquid para–hydrogen has its two hydrogen spin anti–parallel in the ground state whereas ortho–hydrogen spins are parallel with spin 1. The scattering cross section below 15 meV is roughly a factor of 20 smaller for neutrons on para–hydrogen compared to neutrons on ortho–hydrogen. The energy needed to induce a spin flip with para–hydrogen is 15 meV and to excite its first rotational state is 45 meV. Therefore, below 15 meV, neutron spin destruction scattering is zero in para–hydrogen. There is no energy threshold to induce spin destruction scattering with ortho–hydrogen thus the need for para–hydrogen is obvious. A detailed discussion can be found in Bowman *et al.*[118] A proof–of–principle experiment[124] has been carried out examining systematic effects due to electronic noise and detector sensitivity due to magnetic fields. In addition, the CsI detectors were tested while operating in current detection mode due to the high counting statistics.

Parity violation is observed by measuring the gamma flux asymmetry in the CsI detectors

$$\frac{d\omega}{d\Omega} = \frac{1}{4\pi}(1 + A_\gamma \cos\theta_{s,\gamma})$$

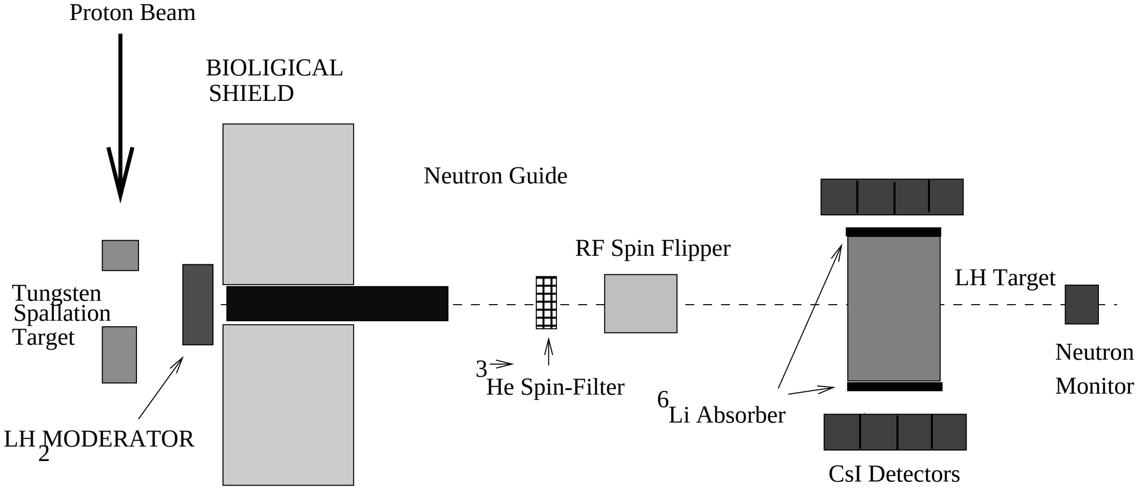

Figure 5-2: Schematic of the gamma asymmetry experiment.

where $\theta_{s,\gamma}$ is the angle between the neutron spin and the emitted photon direction. The uncertainty in the gamma asymmetry $A_\gamma$ is

$$\sigma_{A_\gamma} = \frac{1}{\sqrt{W}}$$

where

$$W = \frac{T_a}{b} \int dE \frac{d\Phi(E)}{dE} Q(E) c(E)$$

and $T_a$ is the required run time, b is the detector efficiency, $d\Phi(E)/dE$ is the differential neutron flux per unit energy, c(E) is the fraction of neutrons captured in the target as a function of energy. The figure–of–merit is $Q(E)=P_n^2 T_n$ where $P_n$ and $T_n$ are the neutron polarization and transmission respectively. The neutron spin–filter contributes to the uncertainty in the asymmetry through Q(E). Figure 5-3 is a plot of the neutron transmission, polarization, and the figure–of–merit for an initially unpolarized 4 meV neutron beam incident on a 60% polarized neutron spin–filter. The figure–of–merit has a broad maximum around 5 meV. Figure 5-4 is a plot of the neutron polarization, transmission, and figure–of–merit as a function of energy for a 5 atm–cm spin–filter polarized to 60%.

One of the challenges of running this experiment is to produce a neutron spin–filter with high $^3$He polarization. The spin–filter must have a large enough diameter to accept neutrons from the 10 cm × 10 cm neutron super–mirror guide. It is technically challenging to fuse such large flat glass windows onto a cylindrical body to hold pressures above or below one atmosphere. Optical pumping with laser diodes is optimized by the use of higher pressures to pressure broaden the absorption cross section. Laser diodes have a wide line-width (~2 nm) that extends beyond the absorption spectrum. Argon ion/Ti:Sapphire laser system are more ideally suited for such an experiment since they have a very narrow line–width which can be utilized at low pressures. The down side of using these lasers is that they are expensive and cumbersome to operate due to high power and cooling requirements.

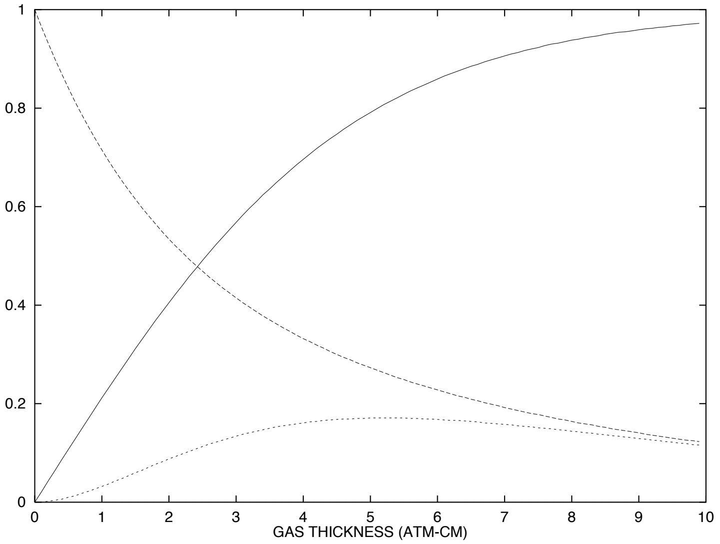

Figure 5-3: This is a plot of the neutron polarization $P_n$ (solid line), transmission $T_n$ (long dashed line) and the figure–of–merit $P_n^2 T_n$ (short dashed line) for an initially unpolarized 4 meV neutron beam incident on a 60% polarized $^3$He sample.

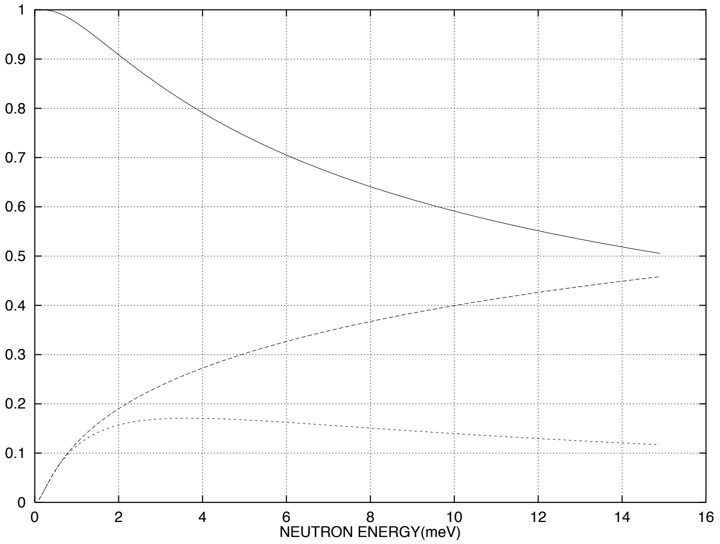

Figure 5-4: Neutron polarization (solid line), $P_n$, transmission (long dashed line) , $T_n$, and the figure–of–merit $P_n^2 T_n$ (short dashed line) for a 5 atm–cm neutron spin–filter polarized to 60%.

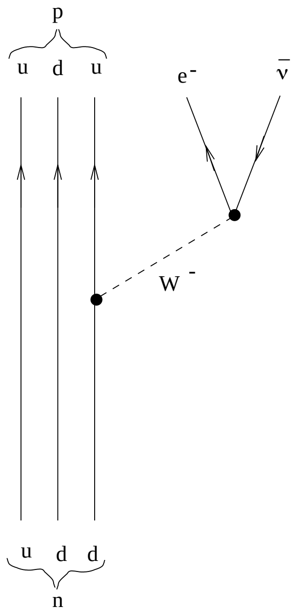

Figure 5-5: $\beta$–decay of a neutron.

### 5.2.3 Neutron $\beta$ Decay

A second fundamental physics application for polarized neutrons is the decay of free neutrons. Neutron decay is governed by, and therefore allows for the study of the weak interaction. Free neutron decay is a clean testing ground of the weak interaction since one does not have to worry about nuclear structure effects. The decay reaction is

$$n \rightarrow p + e^- + \bar{\nu}_e$$

where $\bar{\nu}_e$ is the electron antineutrino. In the quark model neutron decay is explained by a d–quark decay d $\rightarrow$ u + e$^-$ +$\bar{\nu}_e$ (see figure 5-5).

The probability of decay of a free neutron has been calculated[125] and is given by

$$W \sim 1 + a\frac{\mathbf{p}_e \cdot \mathbf{p}_{\bar{\nu}}}{E_e E_{\bar{\nu}}} + \hat{\mathbf{S}}_n \cdot \left( A\frac{\mathbf{p}_e}{E_e} + B\frac{\mathbf{p}_{\bar{\nu}}}{E_{\bar{\nu}}} + D\frac{\mathbf{p}_e \times \mathbf{p}_{\bar{\nu}}}{E_e E_{\bar{\nu}}} \right) \tag{5.1}$$

where $E_e$ and $\mathbf{p}_e$ are the energy and momentum of the emitted electron, $E_{\bar{\nu}}$ and $\mathbf{p}_{\bar{\nu}}$ are the energy and momentum of the emitted anti–neutrino, and $\hat{\mathbf{S}}_n$ is the unit vector pointing in the direction of the neutron spin. The factors a, A, B, D are the electron–antineutrino, neutron spin–electron, neutron spin–antineutrino, and triple correlation coefficients. It is the coefficients A, B, and D that are of interest here since their measurement requires the use of a polarized neutron beam. Since a parity operation on $\mathbf{S}_n \cdot \mathbf{p}_e \rightarrow -\mathbf{S}_n \cdot \mathbf{p}_e$ a measurement of A would indicate parity violation. Similarly, $\mathbf{S}_n \cdot \mathbf{p}_{\bar{\nu}} \rightarrow -\mathbf{S}_n \cdot \mathbf{p}_{\bar{\nu}}$ under parity operation indicating a nonzero value for B if parity is not conserved in $\beta$–decay. Under a time reversal transformation $\mathbf{S}_n \cdot \left(\frac{\mathbf{p}_e \times \mathbf{p}_{\bar{\nu}}}{E_e E_{\bar{\nu}}}\right) \rightarrow -\mathbf{S}_n \cdot \left(\frac{\mathbf{p}_e \times \mathbf{p}_{\bar{\nu}}}{E_e E_{\bar{\nu}}}\right)$. A nonzero value of D would be a direct measurement of time noninvariance. Currently, an experiment at the National Institute of Standards and Technology (NIST)[112] is being performed to measure D, the triple correlation coefficient which, if nonzero, would be a clear indication of time noninvariance. The Standard Model predicts a value of D too small to measure. However, extensions to the standard model predict observable values. Previous measurements[113,114] of D have been consistent with zero with zero with an average value of $0.3 \pm 1.5 \times 10^{-3}$. Interpretation of correlations is complicated by the presence of final state effects causing T–invariant interactions to mimic T–violating observables. Calculations of D for the neutron from this effect is approximately $5 \times 10^{-5}$.[115,116] Polarized neutron $\beta$–decay offers a clean nuclear system to search for time violation whereas a measurement of the triple correlation coefficient in nuclear system can be hard to interpret due to final state effects.

## 5.3 Principles of Polarized $^3$He Neutron Spin–Filters

Polarized $^3$He can be used as a neutron polarizer since there exists a broad ($\Gamma = 400$ keV) unbound resonance ($J^\pi = 0^+$) located 650 keV below the neutron binding energy in the intermediate state $^4$He$^*$,[117] for the reaction

$$n +^3 \mathrm{He} \longrightarrow^4 \mathrm{He}^* \longrightarrow \mathrm{p} + \mathrm{t}.$$

There is a strong spin dependence in the cross section due to the fact the spin of the $^3$He nucleus is carried mostly by the unpaired neutron; only neutrons with spin anti–parallel to that of the $^3$He nucleus will be absorbed. The ratio of the cross section of anti–parallel neutron spin capture to that of the total cross section was measured[126] with a value $1.010 \pm 0.032$, which indicates a small cross section due to non–resonant scattering. For a spin–filter with 100% $^3$He polarization of sufficient density and thickness, neutrons with 100% polarization and 50% transmission would be observed for an initially unpolarized neutron beam. The spin direction of the neutron beam would be aligned along the direction of the $^3$He polarization. Creating a 100% polarized $^3$He spin–filter is not feasible, however spin–filters producing high neutron polarization and transmission are achievable.

For an unpolarized mono–energetic beam of neutrons the transmission through an unpolarized $^3$He sample is given by

$$T = T_0 e^{-\sigma_0(v) n_{He} l} \tag{5.2}$$

where $T_0$ is the transmission through an empty cell, $\sigma_0(v)$ is the absorption cross–section for unpolarized neutrons with velocity $v$, $n_{He}$ is the $^3$He number density and $l$ is the thickness of $^3$He. For unpolarized 25.3 meV neutrons the cross section is

$$\sigma_0(v) \approx 5327b. \tag{5.3}$$

The $^3$He polarization is defined as

$$P_{He} = \frac{n^+_{He} - n^-_{He}}{n^+_{He} + n^-_{He}} \tag{5.4}$$

where $n^\pm_{He}$ are the $^3$He number densities for spin up (+) and down (–) and $n_{He} = n^+_{He} + n^-_{He}$. It is easy to see that $n^\pm_{He}$ can be rewritten in terms of the polarization

$$n^\pm_{He} = n_{He} \frac{(1 \pm P_{He})}{2}.$$

The transmission for neutrons with spin parallel (+) and antiparallel (–) to the $^3$He polarization can be written as

$$T^\pm = e^{(-n_{He} l(\sigma_0 \pm P_{He}\sigma_p))}$$

where $\sigma_0$ and $\sigma_p$ are the unpolarized and polarized cross sections

$$\sigma_0 = \frac{1}{2}(\sigma_+ + \sigma_-)$$

$$\sigma_p = \frac{1}{2}(\sigma_+ - \sigma_-).$$

$\sigma_+$ ($\sigma_-$) is the neutron total cross section for parallel (antiparallel) spins.

For an incident unpolarized neutron beam the number of neutrons with spin up and spin down are equal, $N_i^+$=$N_i^-$=$N_0/2$, where $N_0$ is the total number of incident neutrons. After passing through a spin–filter of length $l$ the number of transmitted neutrons are given by

$$\begin{aligned} N_f^+ &= \frac{N_0 T_0}{2} e^{-n_{He} l(\sigma_0(v) - P_{He}\sigma_p(v))} \\ &= \frac{N_0 T_0}{2} e^{-\sigma_0(v) n_{He} l} e^{-\sigma_p(v) n_{He} l P_{He}} \end{aligned}$$

and

$$\begin{aligned} N_f^- &= \frac{N_0 T_0}{2} e^{-n_{He} l(\sigma_0(v) + P_{He}\sigma_p(v))} \\ &= \frac{N_0 T_0}{2} e^{\sigma_0(v) n_{He} l} e^{\sigma_p(v) n_{He} l P_{He}}. \end{aligned}$$

The neutron polarization and transmission can then be written as

$$P_n = -\tanh\left(\sigma_p(v) n_{He} l P_{He}\right) \tag{5.5}$$

and

$$T_n = T_0 e^{-\sigma_0(v) n_{He} l} \cosh\left(\sigma_p(v) n_{He} l P_{He}\right). \tag{5.6}$$

For $\sigma_- \gg \sigma_+$, which is valid at low neutron energies, $\sigma_0 \approx \sigma_-/2$ and $\sigma_p \approx -\sigma_-/2- \approx \sigma_0$.

For small experimental asymmetries, the statistical accuracy rises in proportion to Q = $P_n\sqrt{(T_n)}$. Figure 5-3 is a plot of the neutron polarization, transmission and Q$^2$ for a 4 meV unpolarized neutron beam incident on a polarized $^3$He spin–filter.

The first use of a polarized $^3$He spin–filter to polarize epithermal neutrons was performed at the Los Alamos Neutron Scattering Center (LANSCE).[127,128] A spin–filter of volume 2.3 cm$^3$, length 3 cm and $^3$He number density $8.7 \times 10^{19}$ cm$^{-2}$ was polarized to $P_{He} = 35 \pm 7\%$, producing a neutron polarization $P_n = 10.3 \pm 1.9\%$ at 0.734 eV. The neutron polarization was also measured using the helicity–dependent transmission at the 0.734 resonance in $^{139}La$: $P_n = 7.7 \pm 2.3\%$.

## 5.4 Accurate Neutron Polarization Measurement at LANSCE

Polarized neutron beams have been shown to be useful for many applications in physics and material science. For some of these applications, an accurate knowledge of the degree of neutron polarization is required. It has been shown by Greene *et al.*[129] that an accurate determination of a monochromatic neutron beam polarization can be accomplished using the relative transmission through a spin–filter. Using equations (5.5) and (5.6) and the identity

$$\tanh^2(\theta) = 1 - \cosh^{-2}(\theta)$$

the neutron polarization can be written as

$$P_n = \sqrt{1 - \left(\frac{T_n^{unpol}}{T_n^{pol}}\right)^2} \tag{5.7}$$

where

$$T_n^{unpol} = T_0 e^{-\sigma_0(v) n_{He} l}$$

is the neutron transmission through the cell when $P_{He} = 0$ and $T_n^{pol}$ is the transmission when $P_{He} \neq 0$. It is interesting to point out that P$_{He}$ can be determined from the neutron transmission without the knowledge of $\sigma_0(v) n_{He} l$.

A measurement of the neutron polarization was carried out at the Los Alamos Neutron Science Center (LANSCE) with collaborators from LANSCE, University of Indiana, Kyoto University, and the University of New Hampshire, where the $^3$He spin–filter was fabricated. The neutron polarizations were measured for energies ranging from 40 meV to 10 eV.[130] The neutron polarization was determined by comparison of the transmission of neutrons through the polarized spin–filter cell to that of an unpolarized reference cell. The value of the number density of $^3$He atoms in each cell is not required since the ratio of number densities can be measured by comparing the transmissions with both cells unpolarized. The transmission ratio is

$$R = \frac{T_0^s e^{-\sigma(v) n_{He}^s l}}{T_0^r e^{-\sigma(v) n_{He}^r l}}$$

where $n_{He}^r$ and $n_{He}^s$ are the number densities for the reference and spin–filter cells and the T$_0$'s are the neutron transmissions through empty cells. The ratio of transmissions for the spin–filter polarized and unpolarized is

$$\frac{T_n^{pol}}{T_n^{unpol}} = \frac{T_n^{pol}}{R T_n^{ref}} = \cosh(n_{He} l \sigma_p). \tag{5.8}$$

Using the measured ratio R and equations (5.7) and (5.8) the neutron polarization can be determined. During the experiment, the polarized spin–filter cell was translated out of the beam of incident neutrons and replaced by the reference cell every 5 minutes. Neutrons are detected and binned in energy using a time–of–flight (TOF) technique. Since the neutrons of interest were not relativistic, the time–of–flight is

$$TOF = \frac{L}{v} = L\sqrt{\frac{m}{2E}}$$

where $L$ is the flight path and $E$ is the kinetic energy of the neutron. During the experiment signals from the detector were recorded in time bins of width $\Delta t$. The acquisition start comes from a signal that was generated by the proton beam. The time–of–flight is

$$TOF = \frac{L}{v} = L\sqrt{\frac{m}{2E}} + T_{offset}$$

where T$_{offset}$ is the timing offset due delays between the start pulse and the location of the neutron beam. Signals observed during a time bin Δt were recorded by a Transient Digitizer. The channel corresponds to a neutron energy given by

$$Channel\# = \frac{L}{\Delta t}\sqrt{\frac{m}{2E}} + \frac{T_{offset}}{\Delta t}.$$

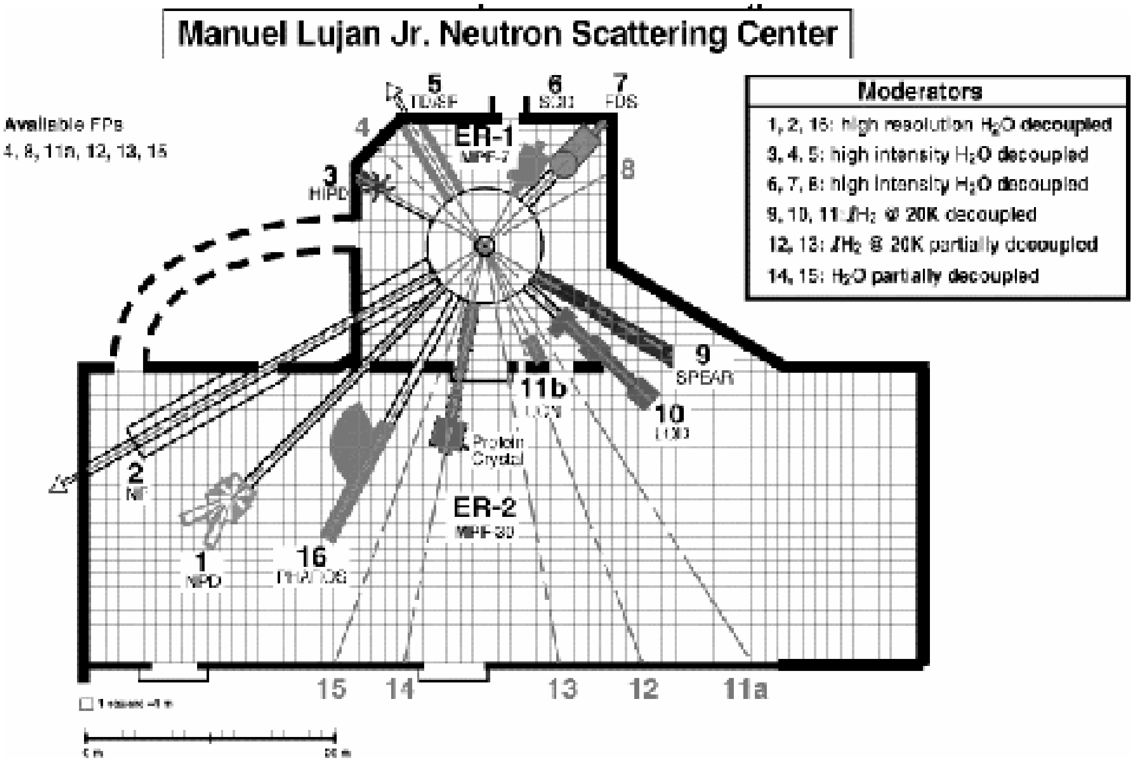

Figure 5-6: Experimental facilities at LANSCE.

Energy calibration was accomplished by inserting material with known neutron absorption resonances and comparing them to the observed spectrum. For energies at 1 eV and below Ir was used and $^{238}$U for higher energies. Wrap–around, the detection of very slow neutrons from previous beam bursts, was not a concern since these slow neutrons were absorbed in the spin–filter.

Neutrons were produced by a $\sim$70 $\mu$A, 800 MeV pulsed proton beam from a storage ring with a pulse width of 250 ns and a repetition rate of 20 Hz incident upon a tungsten spallation target. The spallation neutrons where moderated by a water shield surrounding the spallation target. The neutron source was enclosed in a biological shield with penetrating beam lines leading to various experimental areas. Flight path 2 was used for this measurement (see figure 5-6). Located at the end of the beam line were two ionization chambers. One of the chambers contained $^3$He and the other $^4$He for determination of the neutron flux independent of gamma rays. The $^3$He ion chamber was very sensitive to neutrons whereas the $^4$He chamber was equally sensitive to both neutrons and gammas. The difference between these two detectors produced a signal that was proportional to the neutron flux. Instantaneous neutron rates on the order of 50 kHz at 1 eV were incident to the spin–filter and roughly 15.5 kHz were observed at the detector.

The spin–filter apparatus was located $\sim$10 meters from the source and on a translations system for switching between the polarized and unpolarized cell. Upstream from the spin–filter was a brass collimator with the thin Ir and U foils mounted in front. Another brass collimator was located downstream from the spin–filter followed by a lead collimation wall in front of the entrance window of the vacuum beam–line. At the end of the beam–line, $\sim$60 meters from the spin–filter was a

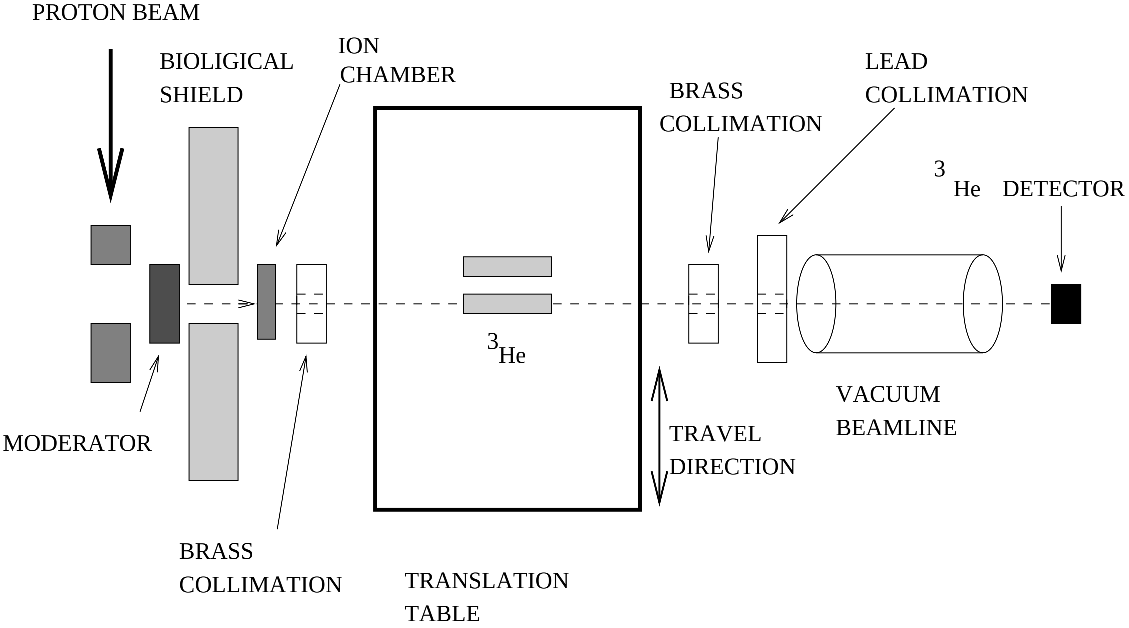

Figure 5-7: Schematic of the neutron polarization experiment.

$^3$He scintillator detector. $^3$He scintillators are ideal for this experiment since they have the ability to detect neutrons with energies in the cold to epithermal range. Additionally, $^3$He scintillator detectors have nearly a 100% efficiency, they can handle high rates, and they have a low sensitivity to gamma ray backgrounds.[131] Signals from the detector were acquired using a transient Digitizer. Figure 5-7 shows the experimental layout.

The spin–filter apparatus is shown in figure 5-8. The holding field was produced by a pair of coils in Helmholtz configuration. The field was approximately 30 gauss at the spin–filter. Perpendicular to the holding field was a 100 kHz oscillating field produced by a pair of RF coils and an amplified signal from a frequency synthesizer. A capacitor was added in series to form a resonant circuit. Perpendicular to the RF and $B_0$ coils, a pair of pick–up coils were placed on either side of the spin–filter cell for detection of the AFP NMR signal (see chapter 3). The NMR signals were used to monitor the relative $^3$He polarization and not the absolute value. The signal from the pick–up coils was amplified using a low–noise pre–amplifier and then sent to a lock–in amplifier. The output from the lock–in was acquired and stored using a Macintosh computer.

The spin–filter cell, the reference cell and the pickup coils were placed inside of an oven made from PEEK and Kapton film. The Kapton was used for transmission of the neutron beam. The oven was heated to 175 °C using hot air from an air heater and maintained with a temperature controller and an RTD located next to the cell. The entire apparatus was mounted onto a translating table that was controlled by the acquisition computer and moved using a stepper motor. The purpose for translating the apparatus was to move the reference cell into the path of the beam and the spin–filter out of the beam. The optical pumping was facilitated by using two fiber coupled diode lasers[65] each delivering $\sim$15 W to the spin–filter. Each laser beam was split into two beams using a linear polarizing cube and then circularly polarized with a $\lambda/4$ plate. The four individual beams illuminated the cell from the side. Each laser was optimized for optical pumping by observing the

| Cell | Dia × Length | P (273K) | $\Gamma^{-1}$ (hours) | windows |
|---|---|---|---|---|
| LA2 | 3.4 cm × 10.0 cm | 3.0 atm | 84.3 | 2 mm 1723 |
| LA5 | 3.6 cm × 10.0 cm | 4.8 atm | 48.5 | 3 mm $^{10}$B and Fe free 1720 |
| LA7 | 3.4 cm × 10.0 cm | 5.5 atm | 38.1 | 3 mm $^{10}$B and Fe free 1720 |
| LA12 | 3.6 cm × 10.1 cm | 5.6 atm | 47.3 | 3.2 mm Fe free 1720 |
| LA13 | 3.6 cm × 10.0 cm | 5.5 atm | 41.1 | 3.2 mm Fe free 1720 |

Table 5.2: LANSCE spin–filter cells.

absorption of the incident beam by rubidium vapor and adjusting the temperature and current of the diode so that the absorption peak was centered around the laser output spectrum. The laser light illuminated the cell through a quartz window in the oven. A $^3$He polarization of approximately 20% was determined from the neutron polarization measurement.[130] A value of 45% $^3$He polarization was achieved during the experiment until a laser malfunctioned causing the polarization to drop to 20%.

The spin–filter and reference cells bodies were made from Corning 1720 aluminosilicate glass with a thickness of approximately 3 mm. Both cells were filled with $\sim$ 3 atmospheres of $^3$He (273 K). The dimensions for the cell used in this experiment (LA2) are given in table 5.2 along with four other cells made for experiments at LANSCE. Some of the windows were made from $^{10}$B free glass to reduce neutron capture. Corning 1720 contains $< 5\%$ by weight natural boron which has an isotopic composition of 19.9% $^{10}$B and 80.1% $^{11}$B. Neutrons are captured by $^{10}$B through the reaction

$$n +^{10}\mathrm{B} \rightarrow^{7} \mathrm{Li} +^{4} \mathrm{He}$$

with a thermal neutron absorption cross section 3840 barns. Additionally, some of the windows were iron free to reduce $^3$He relaxation from the paramagnetic property of iron (see chapter 3. Cell LA2 was used in the neutron polarization measurement. Cells LA12 and LA13 were used at LANSCE to measure the parity violating neutron spin rotation in the n–$^{139}$La p–wave resonance. This experiment required the use of a spin–filter and a spin–analyzer. During the experiment the spin–filter was polarized to ~40% and the analyzer to ~20%.[132]

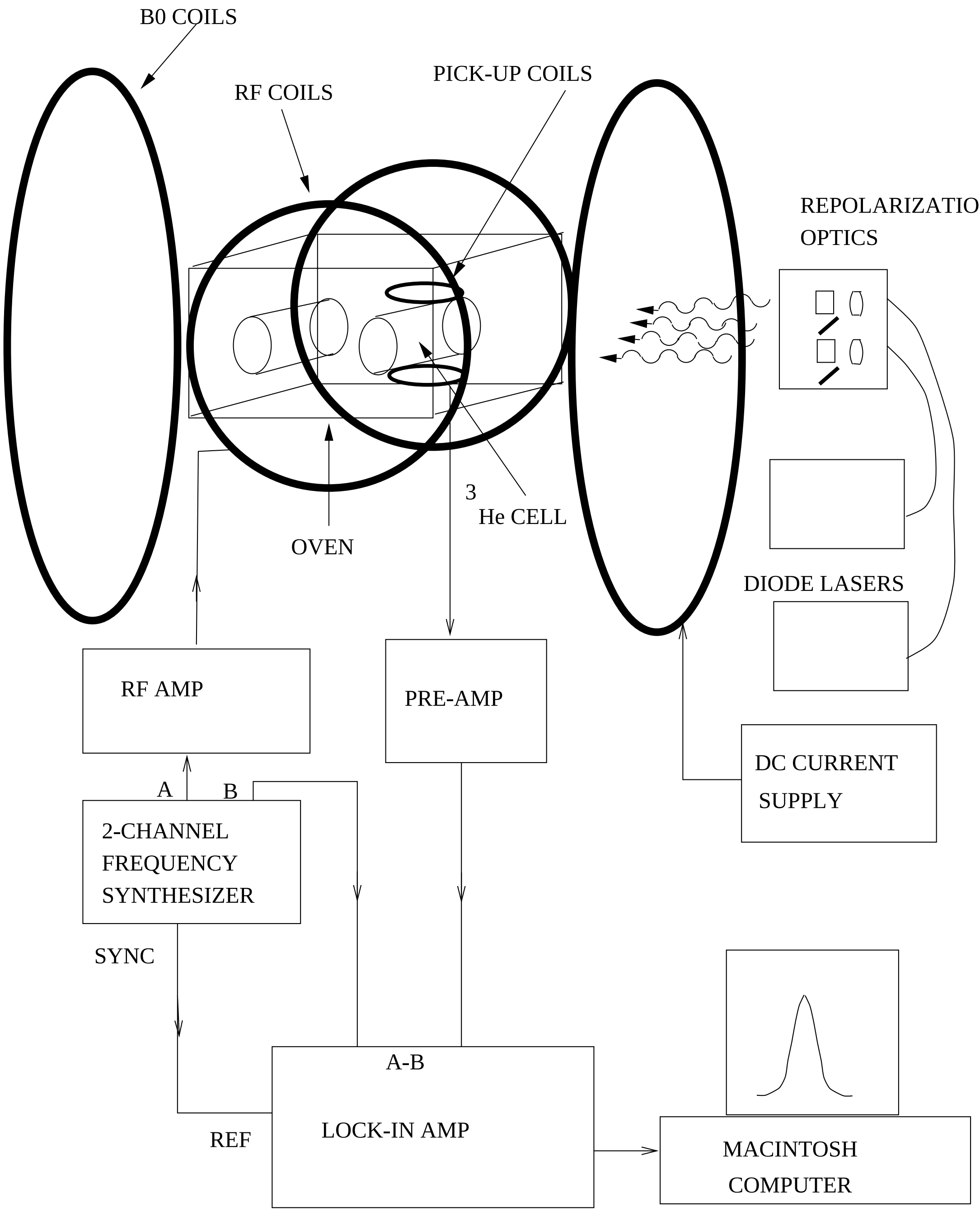

Figure 5-8: The spin–filter apparatus used in the absolute neutron polarization measurement.

Figure 5-9: Photograph of cell LA2.

# List of References

# List of References

[1] T.R. Gentile and R.D. McKeown, *Phys. Rev. A* **47**, 456 (1993)

[2] E. Stoltz, M. Meyerhoff, N. Bigelow, M. Leduc, P.-J. Nacher, G. Tastevin, *Appl. Phys. B* **63**, 629 (1996)

[3] S.F. Pate, *et al.*, MIT/LNS Preprint No. LNS–95–159 (1995)

[4] J. Becker, W. Heil, B. Krug, M. Leduc, M. Meyerhoff, P.J. Nacher, E.W. Otten, Th. Prokscha, L.D. Schearer, R. Surkau, *Nucl. Inst. Meth. A* **346**, 45 (1994)

[5] A. Kastler, *J. Phys. Radium* **11**, 255 (1950)

[6] B. Blankleider and R.M. Woloshyn, *Phys. Rev. C* **29**, 538 (1984)

[7] J.L. Friar, *et al. Phys. Rev. C* **42**, 2310 (1990)

[8] R.W. Schulze and P.U. Sauer, *Phys. Rev. C* **48**, 38 (1993)

[9] F.W. Hersman, *et al.*, MIT/Bates proposed–approved experiment 94–06 "Asymmetry measurement in the quasielastic region using a polarized $^3$He target" (1994)

[10] H.G. Andersen, *et al.*, *Proceedings of the Seventh International Workshop on Polarized Gas Targets and Polarized Beams*, edited by R.J. Holt and M.A. Miller (AIP 421, New York) p. 36 (1998)

[11] W. Korsch, R. McKeown, Z. Mesiani, spokespersons, TJNAF proposal PR94-020, (1994)

[12] P.L. Anthony, *et al.*, *Phys. Rev. Lett.* **71**, 959 (1993)

[13] P.L. Anthony, *et al.*, *Phys. Rev. D* **54**, 6620 (1996)

[14] K. Abe, *et al.*, *Phys. Rev. Lett.* **79**, 26 (1997)

[15] HERMES collaboration, DESY Report No. DESY–PRC–93–06 (1993)

[16] L.J. Lising, *et al.*, *Proceedings of the Intersections Between Particle and Nuclear Physics*: 6th Conference, AIP (1997) pp. 399–402

[17] Y. Masuda, *Nucl. Inst. Meth. A* **402**, 319 (1998)

[18] M.S. Albert, *et al.*, *Nature* **370**, 199 (1994)

[19] L. Zhao, *et al.*, *Jour. Mag. Res. B* **113**, 179 (1996)

[20] A. Kastler, *J. Phys. Radium* **11**, 255, (1950).

[21] A. Kastler, *J. Opt. Soc.* **47**, 460, (1957).

[22] T.R. Carver, *Science* **141**, 599 (1963)

[23] W. Happer, *Rev. Mod. Phys.*, **44**, 169 (1972)

[24] W. Happer, *et al.*, *Phys. Rev.* A **29**, 3092 (1984)

[25] L.C. Balling, In *"Advances in Quantum Electronics,"* vol. 3 (P.W. Goodwin, ed.). Academic Press, New York (1975)

[26] R.J. Knize, Z. Wu, and W. Happer, *"Advances in Atomic and Molecular Physics* vol. 24 Academic Press, (1988)

[27] T.G. Walker, W. Happer, *Rev. Mod. Phys.* **69**, 629 (1997)

[28] M.E. Wagshul, T.E. Chupp, *Phys. Rev. A* **49**, 3854 (1994)

[29] B. Larson, O. Häusser, P.P.J. Delheij, D.M. Whittal, and D. Thiessen, *Phys. Rev. A* **44**, 3108 (1991)

[30] M.V. Romalis, E. Miron, and G.D. Cates, *Phys. Rev. A* **56**, 4569 (1997)

[31] S-Y Ch'en and M. Takeo, *Rev. Mod. Phys.* **29**, 20 (1957)

[32] W. Demtröder, *Laser Spectroscopy* Springer–Verlag, Berlin, Heidelberg, pp 79–1 11 (1981)

[33] A. Gallagher, in *Proceedings of the Fourth International Conference on Atomic Physics, Heidelberg, 1974*, edited by G. zu Putlitz, E.W. Weber, and A. Winnacker, Plenum Press, New York pp 559–574 (1975)

[34] T.G. Waler, J.H. Thywissen, W. Happer, *Phys. Rev. A* **56**, 2090 (1997)

[35] R.J. Knize, *Phys. Rev. A* **40**, 6219 (1989)

[36] M.A. Bouchiat, T.R. Carver and C.M. Varnum, *Phys. Rev. Lett.* **5**, 373 (1960)

[37] R.M. Herman, *Phys. Rev.* **A137**,1062 (1965)

[38] R.L. Gamblin and T.R. Carver, *Phys. Rev.* **A138**, 946 (1965)

[39] A. Abragam, *Principles of Nuclear Magnetism* Oxford University Press, London (Reprint 1996)

[40] K.P. Coulter, A.B. McDonald, W. Happer, T.E. Chupp, M.E. Wagshul, *Nucl. Inst. Meth. A* **270**, 90 (1988)

[41] B. Larson, O. Häusser, P.P.J. Delhij, D.M. Whittal, D. Thiessen, *Phys. Rev. A* **44**, 3108 (1991)

[42] A. Ben–Amar Baranga, S. Appelt, M.V. Romalis, C.J. Erickson, A.R. Young, G.D. Cates, and W. Happer, *Phys. Rev. Lett* **80**, 2801 (1998)

[43] T.J. Killian, *Phys. Rev.* **27**, 578 (1926)

[44] W.H. Press, B.P. Flannery, S.A. Teukolsky, W.T. Vetterling, *Numerical Recipes: The Art of Scientific Computing (FORTRAN Version)* Cambridge University Press, New York (1990)

[45] S. Meiboom, *J. Chem. Phys.* **34**, 375 (1960)

[46] GE Components, 21800 Tungsten Rd., Cleveland, OH 44177 216-266-2451

[47] National Instruments, 6504 Bridge Point Parkway, Austin, TX 78730–5039 512-794-0100

[48] K.D. Bonin, T.G. Walker, and W. Happer, *Phys. Rev. A* **37**, 3270 (1988)

[49] K.P. Coulter, A.B. McDonald, G.D. Cates, W. Happer, T.E. Chupp, *Nucl. Inst. Meth.* **A276**, 29 (1989)

[50] W.A. Fitzsimmons, L.L. Tankersley, and G.K. Walters, *Phys. Rev.* **179**, 156 (1969)

[51] R.S. Timsit, J.M. Daniels, and A.D. May, *Can. J. Phys.* **49**, 560 (1971)

[52] T.B. Smith, T.E. Chupp, K.P. Coulter, R.C. Welsh, *Nucl. Inst. Meth. A* **402**, 247 (1998)

[53] W. Heil, H. Humblot, E. Otten, M. Schafer, R. Sarkau, and M. Leduc, *Phys. Lett. A* **201**, 337 (1995)

[54] Schott Corporation, Technical Glass Division, 3 Odell Plaza, Yonkers, NY 10701 914–968–8900

[55] E. Cheng, M.W. Cole, W.F. Saam, and J. Treiner, *Phys. Rev. Lett.* **67**, 1007 (1991)

[56] G.D. Cates, S.R. Schefer, and W. Happer, *Phys. Rev. A* **37**, 2877 (1988)

[57] G.D. Cates, D.J. White, T.R. Chien, S.R. Schefer, and W. Happer, *Phys. Rev. A* **38**, 5092 (1988)

[58] N.R. Newbury, A.S. Barton, G.D. Cates, W. Happer, and H. Middleton, *Phys. Rev. A* **48**, 4411 (1993)

[59] Anderson Glass Company, Inc., Fitzwilliam, NH 03447 603–585–7771

[60] Princeton University, Chemistry Dept., Princeton, NH 08544 609–258–3915

[61] BNZ Materials, Inc., Littleton, CO 303–978–1199

[62] Omega Engineering, Inc., PO Box 4047, Stamford, CT 800-826-6342

[63] Isotec, Inc. 3858 Benner Rd. Miamisburg, OH 45342 800-448-9760

[64] M. Bock, *et al,*, *Mag. Res. Med.* **38**, 890 (1997)

[65] Opto Power Corp., 3321 E. Global Loop, Tucson, AZ. 85706 520-746-1234

[66] C.P. Slichter, *Principles of Magnetic Resonance*, Third Edition, Springer–Verlag, 1990

[67] B. Cowan, *Nuclear Magnetic Resonance and Relaxation*, Cambridge University Press, 1997

[68] E. Fukushima and S.B.W. Roeder, *Experimental Pulse NMR, A Nuts and Bolts Approach*, Addison–Wesley Publishing Co., Reading MA, 1981

[69] E.M. Purcell, H.C. Torrey, and R.V. Pound, *Phys. Rev.* **69**, 37 (1946)

[70] F. Bloch, W.W. Hansen, and M.E. Packard, *Phys. Rev.* **69**, 127 (1946)

[71] P.C. Lauterbur, *Nature* **242**, 190 (1973)

[72] P. Mansfield and P.K. Grannell, *J. Phys. C* **6**, L422 (1973)

[73] R. Damadian, M. Goldsmith, and L. Minkoff, *Physiol. Chem. Phys.* **9**, 97 (1977)

[74] J.D. Jackson, *Classical Electrodynamics, Second Edition* John Wiley & Sons, New York 1962

[75] D.I. Hoult and R.E. Richards, *Journal of Magnetic Resonance* **24**, 71 (1976)

[76] D.I. Hoult and P.C. Lauterbur, *Journal of Magnetic Resonance* **34**, 425 (1979)

[77] P.T. Callaghan and C.D. Eccles, *Jour. Mag. Res.* **71**, 426 (1987)

[78] P.T. Callaghan and C.D. Eccles, *Jour. Mag. Res.* **78**, 1 (1988)

[79] J.F. Schenck, *Med. Phys.* **23**, 815 (1996)

[80] F. Reif, *Fundamentals of Statistical and Thermal Physics* McGraw-Hill, New York 1965

[81] M.S. Albert, G.D. Cates, B. Driehuys, W. Happer, B. Saam, C.S. Springer Jr, & A. Wishnia, *Nature* **370**, 199 (1994)

[82] H. Middleton, R.D. Black, B. Saam, G.D. Cates, G.P. Cofer, R. Guenther, W. Happer, L.W. Hedlund, G.A. Johnson, K. Juvan, J. Swartz, *Mag. Res. Med.* **33**, 271 (1995)

[83] R.D. Black, H. Middleton, G.D. Cates, G.P. Cofer, B. Driehuys, W. Happer, L.W. Hedlund, G.A. Johnson, M.D. Shattuck, J.C. Swartz, *Radiology* **199**, 867 (1996)

[84] J.R. MacFall, H.C. Charles, R.B. Black, H. Middleton, J.C. Swartz, B. Saam, B. Driehuys, C. Erickson, W. Happer, G.D. Cates, G.A. Johnson, C.E. Ravin, *Radiology* **200**, 553 (1996)

[85] P. Bachert, L.R. Schad, M. Bock, M.V. Knopp, M. Ebert, T. Gro$\beta$mann, W. Heil, D. Hofmann, R. Surkau, E. W. Otten, *Mag. Res. Med.* **36**, 192 (1996)

[86] M.E. Grossmann, *et al.*, *Lancet* **347**, 1297 (1996)

[87] T.L. Petty and G.G. Weinmann, *JAMA* **277**, 248 (1997)

[88] B. Saam, N. Drukker, W. Happer, *Chem. Phys. Lett.* **263**, 481, (1996).

[89] L. Darrasse, G. Guillot, P.J. Nacher, G. Tastevin, *Comptes Rendus de l Academie des Sciences Serie II Fascicule B–Mecanique Physique Chimie Astronomie* **324**, 691 (1997)

[90] B. Pütz, D. Barsky, K. Schulten, *Chem. Phys. Lett.* **183**, 391 (1991)

[91] M. Xi-An, *et al.*, *Chem. Phys. Lett.* **227**, 65 (1994)

[92] G. Jian-Xin, *et al.*, *Phys. Rev. B* **50**, 13461 (1994)

[93] M. Xi-An, *et al.*, *Chem. Phys. Lett.* **222**, 417 (1994)

[94] S.D. Swanson, M.S. Rosen, B.W. Agranoff, K.P. Coulter, R.C. Welsh, T.E. Chupp, *Mag. Res. Med.* **38**, 695 (1997)

[95] Ya. S. Greenberg, *Rev. Mod. Phys.* **70**, 175 (1998)

[96] D.M. TonThat, *et al.*, *Chem. Phys. Lett.* **272**, 245 (1997)

[97] R. Surkau, *et al.*, in *ISMRM, 5th Ann. Meet., Vancouver, BC*, 182 (1997) X.J. Chen *et al.*, in *ISMRM, 5th Ann. Meet., Vancouver, BC*, 21087 (1997)

[98] R.J. Hanson and F.M. Pipkin, *Rev. Sci. Inst.* **36**, 179 (1965)

[99] Chemglass, Inc., 3861 North Mill Rd., Vineland, NJ 08360 800-843-1794

[100] P.T. Callaghan, "*Principles of Nuclear Magnetic Resonance Microscopy*," Oxford University Press, 1991

[101] W.G. Williams, *Polarized Neutrons* Oxford University Press, New York 1988

[102] Yu.A. Alexandrov, *Fundamental Properties of the Neutron* Oxford University Press, Oxford, England 1992

[103] R.M. Moon, T. Riste, and W.C. Koehler, *Phys. Rev. A* **181**, 920 (1969)

[104] R.M. Moon, *Physica* **137B**, 19 (1986)

[105] F. Mezei, *Commun. Phys.* **1**, 8 (1976)

[106] S.I. Penttilä, *et al.*, *Proc. of the 11th Int. Symp. on High Energy Spin Physics*, ed. K.J. Heller and S.L. Smith (AIP Conf. Proc. No 343, 1995) p. 532

[107] *Proceedings of the International Workshop on Fundamental Physics with Slow Neutrons* Grenoble, France *Nulc. Inst. Meth. A* **284** 1989

[108] T.D. Lee, and C.N. Yang, *Phys. Rev.* **104**, 254 (1956)

[109] C.S. Wu, E. Ambler, R.W. Hayward, D.D. Hoppes, and R.P. Hudson, *Phys. Rev.* **105**, 1413 (1957)

[110] J.H. Christianson, J.W. Cronin, V.L. Fitch, R. Turlay, *Phys. Rev. Lett.* **13**, 138 (1964)

[111] S. Lamoreaux, *et al.*, *Proceedings of the Intersections Between Particle and Nuclear Physics*: 6th Conference, AIP (1997) pp. 387

[112] L.J. Lising, *et al.*, *Proceedings of the Intersections Between Particle and Nuclear Physics*: 6th Conference, AIP (1997) pp. 399–402

[113] R.I. Steinberg, *et al.*, *Phys. Rev. Lett.* **33**, 41 (1974)

[114] B.G. Erozolimskii, *et al.*, *Sov. J. Nucl. Phys* **28**, 48 (1978)

[115] J.D. Jackson, *et al.*, *Nucl. Phys.* **4**, 206 (1957)

[116] C.G. Callan, *et al.*, *Phys. Rev.* **162**, 1494 (1962)

[117] A. Csótó and G. Hale, *Phys. Rev. C* **55**, 2366 (1997)

[118] J.D. Bowman, *et al.*, LANSCE Proposal to the Department of Energy

[119] E.G. Adelberger and W.C. Haxton, *Ann. Rev. Nucl. Part. Sci.* **35**, 501 (1985)

[120] B. Desplanques, in *Parity–Non–Conserving Nucleon–Nucleon Interactions*, edited by N. Auerbach and J. Bowman, World Scientific, Singapore, p. 98 (1996)

[121] E. Henley, W.–Y. Hwang, and L. Kisslinger, Phys. Lett. B **367**, 21 (1996)

[122] D. Kaplan and M. Savage, *Nucl. Phys A* **556**, 653 (1993)

[123] N. Kaiser and U.-G. Meissner, *Nucl. Phys A* **499**, 699 (1989)

[124] W.M. Snow, W.S. Wilburn, J.D. Bowman, M.B. Leuschner, S.I. Penttilä, V.R. Pomeroy, D.R. Rich, E.I. Sharapov, and V. Yuan, submitted to *Nucl. Inst. Meth. A*

[125] J.D. Jackson, G.B. Treiman, H.W. Wyld, *Phys. Rev.* **106**, 517 (1957)

[126] L. Passell and R.I. Schermer, *Phys. Rev.* **150**, 146 (1966)

[127] K.P. Coulter, A.B. McDonald, W. Happer, T.E. Chupp, M.E. Wagshul, *Nucl. Inst. Meth. A* **270**, 90 (1988)

[128] K.P. Coulter, T.E. Chupp, A.B. McDonald, C.D. Bowman, J.D. Bowman, J.J. Szymanski, V. Yuan, G.D. Cates, D.R. Benton, E.D. Earle, *Nucl. Inst. Meth. A* **288**, 463 (1990)

[129] G.L. Greene, A.K. Thompson, M.S. Dewey, *Nucl. Inst. Meth. A* **356**, 177 (1995)

[130] D.R. Rich, University of Indiana, Private Communication.

[131] P. Guazzoni, M. Pignanelli, *Nucl. Inst. Meth. A* **72**, 195 (1969)

[132] T. Haseyama, Private Communication, Kyoto University